Spring 5-11-2023

Origin and Structure of the First Sharp Diffraction Peak of Amorphous Solids

Devilal Dahal

ORIGIN AND STRUCTURE OF THE FIRST SHARP DIFFRACTION PEAK OF AMORPHOUS SOLIDS

by

Devilal Dahal

A Dissertation
Submitted to the Graduate School,
the College of Arts and Sciences
and the School of Mathematics and Natural Sciences
of The University of Southern Mississippi
in Partial Fulfillment of the Requirements
for the Degree of Doctor of Philosophy

Approved by:

Dr. Parthapratim Biswas, Committee Chair
Dr. Khin Maung Maung
Dr. Katja Biswas
Dr. Sungwook Lee
Dr. Andrew Sung

May 2023

ABSTRACT

Several explanations have been reported in the literature about the origin of extended-range oscillations (EROs) in the atomic pair-correlation function of amorphous materials. Although the radial ordering beyond the short-range order of about 5 Å has been extensively studied in amorphous materials, the exact nature of the radial ordering beyond a nanometer is still not resolved. This dissertation address this problem and explains the nature of the EROs by using high-quality models of amorphous silicon (*a*-Si) obtained from Monte Carlo and Molecular Dynamics simulations. The extended-range ordering in *a*-Si is examined through radial oscillations on the length scale of 20-40 Å by comparing the distribution of atoms in different coordination shells in *a*-Si with that in partially ordered networks of Si atoms and disordered configurations of crystalline silicon. In addition, the origin and structure of the First Sharp Diffraction Peak (FSDP) of *a*-Si near 2 $Å^{-1}$ and that of amorphous silica (*a*-SiO_2) near 1.5 $Å^{-1}$ wavevector region is studied with particular emphasis on the position, intensity, and width of the FSDP. Likewise, the effects of temperature, structural disorder, and anharmonicity on the vibrational mean-square displacement (MSD) of Si atoms of *a*-Si are studied using harmonic approximation and ab initio molecular-dynamics simulations.

This study shows that weak radial ordering exist in the atomic correlations of *a*-Si extended up to 20-40 Å. The analysis of the radial shell-by-shell contribution to the FSDP of *a*-Si reveals that the second and fourth radial shells significantly contribute to the FSDP of *a*-Si. A similar analysis of the FSDP of *a*-SiO_2 indicates the higher contribution to the FSDP of *a*-SiO_2 is from the third and fourth radial shells. Also, an approximate functional relation has been obtained between the position of the FSDP and the average radial distance of Si atoms in the second radial shell of *a*-Si. On the other hand, the analysis of the effect of anharmonicity on the MSD of Si atoms suggests the vibrational motion in *a*-Si is practically unaffected by anharmonic effects at temperatures below 400 K.

ACKNOWLEDGEMENT

I want to express my profound appreciation to my advisor, Dr. Parthapratim Biswas, for his unwavering encouragement, guidance, support, and inspiration during my Ph.D. journey. His scientific knowledge and exceptional teaching and mentoring skills have nurtured me and enabled me to achieve more than possible. Also, the courage and tideless support I am getting from him are the reasons I make to this stage of my career as a theoretical/computational physicist.

I also sincerely thank the members of my dissertation committee, Dr. Khin Maung Maung, Dr. Sungwook Lee, Dr. Andrew Sung, and Dr. Katja Biswas for their invaluable support, constructive feedback, and wise counsel throughout my graduate study. Additionally, I am grateful to Dr. Ras B. Pandey and Dr. Micheal D. Vera for their insightful suggestions and comments that supported my early days as a graduate student interested in computational physics.

I am also thankful to my collaborators, Dr. Raymond Atta-Fynn and Prof. Stephen R. Elliott, who repeatedly provided instructive feedback and corrected my research work. I also thank my senior group members, Dr. Durga Paudel and Dr. Dil Limbu, and colleague Hiroka Warren for their valuable discussions, comments, and suggestions. Also, the discussions made with fellow group members have fond memories.

I am grateful to the School of Mathematics and Natural Sciences at the University of Southern Mississippi and to all faculty and staff of the Department of Physics and Astronomy for their direct or indirect support during my graduate study. Moreover, I thank the National Science Foundation for my partial financial support during my study.

Most importantly, I am grateful to my wife, Mala Sapkota, for her unconditional love, motivation, dedication, and support, the reason I been able to achieve this very goal of my life. Finally, I want to thank our parents, Kapil Mani Dahal, Dil Maya Dahal, Hari Sapkota, Parbati Sapkota, and other family members for their unwavering support and encouragement throughout these years. And, thanks to Babi and Sidh for being with us during these stressful and equally joyful months.

DEDICATION

To my lovely wife *MALA SAPKOTA*

TABLE OF CONTENTS

ABSTRACT ii

ACKNOWLEDGMENTS iii

LIST OF ILLUSTRATIONS vii

LIST OF TABLES xiv

LIST OF ABBREVIATIONS xv

1 INTRODUCTION **1**
1.1 Amorphous Semiconductors 1
1.2 Amorphous Silicon 2
1.3 Amorphous Silica 5
1.4 First Sharp Diffraction Peak 6
1.5 Outline of the dissertation 7

2 COMPUTER MODELING AND CHARACTERIZING THE STRUCTURE OF AMORPHOUS MATERIALS **9**
2.1 Computer Modeling of amorphous materials 9
2.2 First principles modeling: Density Functional Theory (DFT) method 13
2.3 Structural descriptors of amorphous materials 15
2.4 Electronic properties 19
2.5 Debye-Waller Factor 20
2.6 Atomic dynamics 21

3 EXTENDED-RANGE ORDER IN AMORPHOUS SILICON **22**
3.1 Introduction 22
3.2 Computational method 24
3.3 Results and Discussion 26
3.4 Conclusions 45

4 ORIGIN AND THE STRUCTURE OF THE FIRST SHARP DIFFRACTION PEAK OF AMORPHOUS SILICON **46**
4.1 Introduction 46
4.2 Models and Methods 48
4.3 Results and Discussion 49

4.4 Conclusions 67

5 RADIAL SHELL CORRELATIONS AND FIRST SHARP DIFFRACTION PEAK OF AMORPHOUS SILICA 69
5.1 Introduction 69
5.2 Computational Methods 70
5.3 Results and Discussion 71
5.4 Conclusion 80

6 DEBYE-WALLER FACTOR AND DYNAMICAL PROPERTIES OF AMORPHOUS SILICON 82
6.1 Introduction 82
6.2 Method and Models 84
6.3 Results and Discussion 89
6.4 Conclusions 107

7 SUMMARY 110

BIBLIOGRAPHY 112

LIST OF ILLUSTRATIONS

Figure

1.1 The topology of *a*-Si (left) and *c*-Si in diamond structure (right). 3
1.2 Comparison of the atomic pair correlation function of *a*-Si and *c*-Si up to 8 Å of radial separation. 3
1.3 A snapshot of the topology of *a*-SiO_2 showing bonding of Oxygen (red spheres) and Silicon atoms (green spheres). 5

2.1 A general flowchart of a molecular dynamics simulation method. 10
2.2 A simplified flowchart of the Markov chain Monte Carlo (MCMC) algorithm. . 12
2.3 Simplified flowchart of the self-consistent Khon-Sham DFT calculation. 14
2.4 A toy diagram showing a bond angle (left) between the an atom (red) and its first nearest-neighbor atoms (blue) and the rings in a network of 9 atoms, the rings are of size 4 and 8 (right). 18
2.5 A diagram representing electronic density of states in a single crystal silicon and amorphous silicon, localized states can emerge within the band gap of EDoS of *a*-Si. [91] 19

3.1 The pair-correlation functions of three partially-ordered models (M1 to M3) of Si atoms, showing radial correlations up to a length of 6 Å. The results for *a*-Si (WWW models) are shown for comparison with that for the M3 model. The size of the models corresponds to 21,952 atoms and the PCF data were averaged over three independent configurations for each model. 27
3.2 The reduced pair-correlation function, $G(r)$, of *a*-Si, obtained from a configurational averaging of three large MD models of size 400,000 atoms. The inset shows the presence of radial oscillations up to 40 Å, which are known as the extended-range oscillations in *a*-Si. 28
3.3 The reduced PCFs of the 400,000-atom MD models and 21,952-atom WWW models showing the presence of considerable extended-range oscillations in larger MD models. For clarity, the radial distances are scaled by the corresponding first peak of the PCF, i.e., $R = r/r_0$, where r_0=2.37 Å. 30
3.4 The electronic density of states (EDOS) of 21,952-atom WWW and 400,000-atom MD models obtained from the tight-binding approximation. The presence of an electronic band gap is clearly visible in the plots. 30
3.5 The presence of radial oscillations in MD models of *a*-Si (blue) of size 400,000 atoms and two *dc*-Si structures of size 405,224 atoms from 15 Å to 30 Å. The positions of the radial peaks of *a*-Si approximately correspond to those of *dc*-Si, indicating the possible presence of weak extended-range ordering in *a*-Si beyond 15 Å. 31

3.6 A schematic representation showing the first two coordination shells of a central atom (blue) in a two-dimensional disordered network. The atoms in the first shell (green) and the second shell (yellow) can be reached from the central atom in one step and two steps, respectively. 32
3.7 The shell pair-correlation function, $g_n(r)$, for the nth coordination shell of a 21,952-atom WWW model of a-Si. The total $g(r)$ (dashed black), which is given by the sum of all shell PCFs, is also shown in the plot. 33
3.8 The shell pair-correlation functions, $g_{13}(r)$, obtained from 21,952-atom WWW models of a-Si (red), dc-Si (blue/purple/cyan), and partially-ordered configurations M2 (green) of Si atoms. The disordered crystalline structures were generated from the diamond c-Si structure, using σ = 0.3, 0.8, and 1.0 Å. . . . 34
3.9 The variation of the Fisher-Pearson coefficient of skewness, s, for the distribution $g_{13}(r;\sigma)$ with σ for a number of dc-Si models (blue). The coefficients for the M2 model (green) and a-Si (red), for $\sigma = 0$, are shown in the plot for comparison. 35
3.10 The full width at half maximum (FWHM) for a set of partially-ordered configurations (M1 to M3), a-Si, and four dc-Si structures of size 21,952 atoms. The dc-Si structure (with σ = 0.2 Å) is the most ordered configuration, whereas M1 is the least ordered configuration, by construction. 35
3.11 The effect of the addition of positional disorder on the FWHM of the shell PCFs in M1, M3, and a-Si. The FWHM values of the unperturbed models are also shown for comparison. 37
3.12 The effect of the addition of positional disorder, with σ = 0.5 Å, on the radial oscillations in a 400,000-atom MD model of a-Si between 20 Å and 40 Å. The results for the corresponding pristine a-Si model (green) are also shown for comparison. 38
3.13 The Shannon measure of information (SMI), associated with a discrete probability measure p_n, obtained from the shell pair-correlation functions, $g_n(r)$, for M1 to M3, a-Si, and diamond c-Si. For disordered and amorphous Si networks, the results were averaged over three independent configurations for each shell. 38
3.14 The autocorrelation coefficient, $\gamma(r_k)$, of a set of $G(r)$ values from r = 15 Å to r = 45 Å, constructed from 400,000-atom MD models of a-Si, showing the presence of radial correlations up to 45 Å. The root-mean-square fluctuations are shown as error bars (blue vertical lines). For visual clarity, the results for the radial region from 35 Å to 45 Å are shown in the inset. 39
3.15 The decay of the radial peak heights in $G(r)$ for a-Si (blue) and dc-Si (red and green) with peak distances. The exponential fit of the peak positions (dashed blue line) corresponds to the data for a-Si models of size 400,000 atoms. The decay length for a-Si corresponds to a value of 4.81 Å. The corresponding peak positions for dc-Si structures are shown for comparison. 41

3.16 The static structure factor, $S(Q)$, of a 21,952-atom WWW model of a-Si obtained from the Gaussian approximation (red line) and from direct numerical calculations (blue circles) using Eq. (3.7). 42
3.17 The convergence of the intensity of the FSDP (at Q_0) and the principal peak (at Q_1), obtained from Eq. (3.7), with respect to the number (i) of Gaussian peaks/troughs for a 21,952-atom WWW model. The radial length associated with the Gaussian peaks/troughs is indicated in Å on the secondary x axis (top). 43

4.1 The structure factor of a-Si obtained from simulations and experiments. The simulated data are from 3000-atom WWW models of density 2.28 g.cm^{-3}, whereas the experimental data correspond to those from Ref. [28]. The simulated data are obtained by averaging over 10 models from independent runs. 51
4.2 The normalized bond-angle distribution for a-Si, obtained for 3000-atom WWW models. The full width at half maximum (FWHM) corresponds to a value of 21.4°. The distribution is obtained by averaging over 10 independent models. . 52
4.3 The structure factor of a-Si in the vicinity of the FSDP from simulations and experiments. Experimental data (•) correspond to as-implanted samples from Ref. [101], whereas simulated data refer to 216-atom (♦), 1000-atom (■), 2000-atom (▲), and 3000-atom (■) unrelaxed WWW models. 53
4.4 Effects of approximate first-principles relaxations on the position and the intensity of the FSDP of a-Si for a 3000-atom model before (■) and after (●) relaxation. A small shift of the diffraction peak toward higher values of Q is accompanied by a slight reduction of the peak intensity in the relaxed model. The corresponding reduced pair-correlation functions near the first peak are shown in the inset. 54
4.5 The reduced pair-correlation function, $G(r)$, of a-Si obtained from configurational averaging of ten 3000-atom WWW models. The presence of the first six radial shells, which extend up to a distance of $\approx$ 12 Å, is highlighted in different colors. 55
4.6 The contribution to the FSDP, $F_i(Q)$, near Q_0, originating from the first six radial shells and the total $F(Q)$ (blue). The results correspond to 3000-atom WWW models, and are averaged over ten configurations. The color of the plots corresponds to the color of the radial shells in Fig. 4.5. 56
4.7 The contribution, $F_i(Q)$, to the principal peak at Q_1 = 3.6 Å^{-1} from the first six radial shells of the reduced pair-correlation function. The total $F(Q)$ is shown in blue color for comparison. The results are obtained via configurational averaging of data from ten 3000-atom models. 58
4.8 The dependence of the intensity of the FSDP, $S(Q_0)$, with the radial cutoff distance, R_c, for a number of models of different sizes, as indicated in the plot. The experimental values of $S(Q_0)$ reported in the literature are shown as horizontal dashed lines: 1) $S(Q_0)$=1.52 from Ref. [101]; 2) $S(Q_0)$=1.37 from Ref. [29]; and 3) $S(Q_0)$=1.55 from Ref. [28]. 59

4.9 The full width at half maximum (FWHM) of the FSDP at Q_0 for a number of models before (■) and after (●) DFT relaxations. The horizontal dashed lines indicate the experimental values of 0.54 Å^{-1} (green), 0.57 Å^{-1} (black), and 0.77 Å^{-1} (indigo) for as-implanted samples of *a*-Si from Refs. [101], [28], and [29], respectively. 61
4.10 A scattered plot showing the presence a clear correlation between the FWHM and $S(Q_0)$ of the FSDP for a number of models of varying system sizes. The solid (red) line corresponds to the linear least-square (LS) fit of the data, whereas $r_{XY} = -0.9$ indicates the Pearson correlation coefficient for the data sets. The horizontal and vertical dotted lines indicate the experimental values of FWHM and $S(Q_0)$, respectively, obtained for as-implanted samples of *a*-Si. 62
4.11 The dependence of the position of the FSDP, Q_0, with the size of the models before (■) and after (•) DFT relaxations. The horizontal lines correspond to the experimental value of Q_0 for as-implanted samples of *a*-Si from Refs. [101] (green), [28] (black), and [29] (indigo). 63
4.12 The variation of the peak position (Q_0) for 3000-atom models of *a*-Si with its mass density before (■) and after (•) DFT relaxations. The value of Q_0 has been observed to vary linearly with the density of the model. The experimental values of Q_0 (horizontal dashed lines) correspond to as-implanted samples of density 2.28 g.cm^{-3} from Refs. [28] (black), [101] (green), and [29] (indigo). 64
4.13 The relation between Q_0 and $\langle R_2^3 \rangle$ of the atoms in the second radial shell. A constant value of $Q_0\langle R_2^3 \rangle$ with respect to the density of *a*-Si models indicates that Q_0 is approximately proportional to the inverse of $\langle R_2^3 \rangle$. The horizontal black line indicates the average value of $Q_0\langle R_2^3 \rangle$ within the density range shown in the plot. 65
4.14 The dependence of Q_0 and $\langle R_4^3 \rangle$ for the atoms in the fourth radial shell of *a*-Si in the density range from 2.15 to 2.3 g.cm^{-3}. The large deviation of $Q_0\langle R_4^3 \rangle$ values, indicated by $\Delta \approx 2.5\,\sigma$, from a constant value suggests that no simple relationship between Q_0 and $\langle R_4^3 \rangle$ exists. 66
4.15 The structure factor, $S(Q)$, in the vicinity of the FSDP from 6000-atom *a*-Si models. The change in $S(Q)$ due to varying radial cutoff distances, r_i, is found to be less than one standard deviation ($\Delta S(Q_0) \approx 0.85\,\sigma$ for r_i = 15 Å, and $0.46\,\sigma$ for r_i = 18 Å). The standard deviation, σ, is obtained from using the maximal radial cutoff $L/2$, which is given by 24.85 Å. The results correspond to the average values of $S(Q)$ obtained from 10 configurations. 67
4.16 The fractional error associated with the calculation of the structure factor in the vicinity of the FSDP with a varying radial cutoff distance, r_i, from 15 Å to 18 Å. $\Delta S(Q)$ is the absolute error and R_c (=24.85 Å) is the half-length of the cubic simulation cell for 6000-atom models. The error due to the truncation of the radial distance at r_i can be seen to be around 1–2%, which is well within one standard deviation of $S(Q_0)$ (see Fig. 4.15). 68

5.1 The total neutron structure factor of a-SiO_2 from simulation (blue line). The experimental S(Q) of v-SiO_2 by Susman *et al.* [149] is given for comparison (red dots). 71
5.2 The Si-O-Si (top) and O-Si-O (bottom) bond angle distribution of a-SiO_2. The average bond angle for Si-O-Si and O-Si-O bonds are found to be 141.5° and 109.5°, respectively. 72
5.3 The reduced pair-correlation function, G(r), of a-SiO_2 extended up to 10 Å. The first seven distinct radial shells are highlighted with different colors. 72
5.4 Contribution to the FSDP of a-SiO_2 from different radial shells, colors used for the plots are consistent with the colors of the corresponding radial shells presented in Fig. 5.3. 73
5.5 The reduced scattering intensity, F(Q), of a-SiO_2 at the vicinity of the FSDP (blue), the contribution from Si-Si (green), Si-O (red), and O-O (black) correlations, in terms of the (weighted) partial reduced scattering intensity, $F_{\alpha\beta}(Q)$, are compared for their contribution to the FSDP. 74
5.6 Contribution of the partial atomic pair-correlations on the total atomic pair-correlation, g(r), of a-SiO_2 (blue). The Si-Si (green), Si-O (red), and O-O (black) pair correlations are presented within 3-8 Å radial length scale. 75
5.7 The radial shells in the partial reduced pair-correlation function $G_{\text{O-O}}(r)$(upper plot) and the radial shell contribution to the partial reduced intensity factor, $F_{\text{O-O}}(Q)$, (lower plot) at the vicinity of the FSDP. 76
5.8 (Top) Distinct radial shells separated on the basis of peak positions on the reduced pair-correlation function $G_{\text{Si-O}}(r)$, and (bottom) contribution of the radial correlations on the partial reduced scattering intensity $F_{\text{Si-O}}(Q)$. 77
5.9 Distinct radial shells of $G_{\text{Si-Si}}(r)$ (above) and the contribution to the FSDP of $F_{\text{Si-Si}}(Q)$ arises from the corresponding radial shells (below). 78
5.10 The partial PCF $g_{\alpha\beta}(r)$ obtained from a-SiO_2 system of density 2.10 $g.cm^{-3}$ (blue) and 2.30 $g.cm^{-3}$ (red), respectively 79
5.11 The partial reduced scattering intensity $F_{\alpha\beta}(Q)$ of a-SiO_2 of density 2.10 $g.cm^{-3}$ (blue) and 2.30 $g.cm^{-3}$ (red), respectively 80
5.12 Variation on the position, Q_0, and intensity, $S(Q_0)$, of structure factor, S(Q), of a-SiO_2 with density. 81

6.1 The MSD, $\langle u^2 \rangle$, of Si atoms in a-Si with its density in the harmonic approximation from lattice-dynamical calculations. The MSD values can be seen to be practically independent of the density at 300 K (blue) and 600 K (red). 90
6.2 A comparison of the distributions of u_i^2 of atoms in a low-density model (blue) and a high-density model (red) of a-Si at 300 K obtained from two independent models with no coordination defects. The MSD values for the distributions are indicated as dashed vertical lines. 91

6.3 The variation of the MSD, $\langle u^2 \rangle$, with temperature in the harmonic approximation for a-Si and c-Si. The contribution to the MSD from the zero-point motion (ZPM) of the atoms is explicitly shown as horizontal lines. 92
6.4 The variation of the Debye-Waller factor of a-Si, e^{-2M}, with temperature for Q = 1.99 Å^{-1} (blue circles) and 3.6 Å^{-1} (red triangles). The results are obtained by using λ = 1.54 Å, which corresponds to Cu K$_\alpha$ lines. The Q values chosen correspond to the FSDP (1.99 Å^{-1}) and the principal peak (3.6 Å^{-1}) in the structure factor of a-Si. 93
6.5 The distributions of local squared displacements, u_i^2, for a-Si at 300 K (blue) and 600 K (red). The solid lines (blue and red) indicate a gaussian fit of the data. The corresponding results for c-Si are also shown in the plot (as green and black lines), which are truncated for visual clarity and comparison. The results for a-Si correspond to 100% defect-free networks. 94
6.6 A 500-atom model of a-Si showing several Si atoms with a large value of u_i^2 at 300 K. Silicon atoms with top 10% of u_i^2 values are shown in red color with a slightly larger radius. The rest of the atoms are shown in yellow color. 95
6.7 A comparison of the distributions of u_i^2 for the tetrahedral sites (black and green) of 100% defect-free a-Si networks and the clustered DBs (filled blue and red) at 300 K and 600 K. The distributions are normalized to an integrated value of 10^{-2}. 96
6.8 A color map showing the contribution to u_i^2 at *clustered* DB sites (left panel) and tetrahedral sites (right panel) from the first eighty normal modes (indexed along Y axis) at 300 K, distributed in the frequency range of 0 and 110 cm^{-1}. The abundance of red specks in the left panel indicates a large contribution at the DB sites from the low-frequency modes. The rightmost vertical bar indicates the percentage contribution of $u_i^2(\nu_j)$ to total u_i^2. The results correspond to 65 DB sites and tetrahedral sites selected from the same models. 97
6.9 A color map showing the contribution to u_i^2 at *isolated* DB sites (left panel) and tetrahedral sites (right panel) from individual low-frequency normal modes at 300 K. The left panel is awash with red specks indicating a high contribution from the low-frequency in the range of 0–110 cm^{-1} modes at the DB sites. The results correspond to 65 DB sites and tetrahedral sites from the models. 98
6.10 The distributions of u_i^2 for clustered (red) and isolated (green) DBs in a-Si networks at 300 K. The results correspond to the data obtained from 65 DBs from two sets of five independent models. The results for the tetrahedral sites (black) are from two 100% defect-free a-Si networks. The distributions are normalized to an integrated value of 0.01. 99
6.11 The MSDs of Si atoms obtained from 500-atom models of a-Si in the presence of two voids (red diamonds) at 300 K, 450 K, and 600 K. The corresponding values of the MSD without voids (blue circles) are also shown in the plot for comparison. 100

6.12 The convergence of the mean zero-point energy (ZPE) per vibrational mode for a-Si obtained from the integral representation in Eq. (6.14) with temperature (blue line). The horizontal lines correspond to the results obtained from the sum of vibrational frequencies (red line at 20.5 meV) and that from the Debye model (green line at 17 meV). A value of Θ_d = 541.5 K is used to calculate the ZPE from the Debye approximation. 102
6.13 The temperature dependence of the molar specific heat, C_v, of a-Si from the Debye approximation (green line and red circles) and *ab initio* lattice-dynamical calculations (blue line). The results for the Debye approximation are obtained by using Θ_d = 528 K and 487 K (from Refs. [204] and [203], respectively). . . 103
6.14 Low-temperature behavior of C_v in a-Si from the Debye approximation (red line), *ab initio* lattice-dynamical calculations (blue line), and experiments [204] (black line) in the region of 20–130 K. An approximate linear behavior of C_v can be seen to appear in the vicinity of 45 K in both experimental and theoretical results, which corresponds to a frequency value of about 0.9 THz. 104
6.15 A comparison of the specific heat, C_v, of a-Si at low temperatures from experimental data (black) in Ref. [203] and the present study, using 500-atom (red) and 1000-atom (blue) models, in the lattice-dynamical (LD) calculations. The results from the Debye theory of specific heat are indicated as a horizontal dashed line (green), which corresponds to C_v/T^3 = 0.481 for Θ_d = 541.5 K. . . 105
6.16 A comparison of $\langle u^2 \rangle$ obtained from 216-atom model of a-Si using lattice-dynamical calculations (blue) and direct AIMD simulations (red). The inset shows the results obtained by using the classical expression of energy, $\langle E_n \rangle = k_B T$ in Eq. (6.6). See section 6.3.5 for a discussion. 106
6.17 The dependence of the MSD, $\langle u^2 \rangle$, on the single- and double-zeta basis functions (SZ and DZ) and the exchange-correlation approximations (LDA and GGA) used in the DFT calculations in this study. The data correspond to the average values obtained at each temperature from two independent configurations. . . . 108

LIST OF TABLES

Table

3.1 Structural properties of three WWW models (W1–W3) and three MD models (MD1–MD3). The average bond length ($\langle r \rangle$), average bond angle ($\langle \theta \rangle$), and the root-mean-square width of bond angles ($\Delta\theta$) are expressed in Å and degree, respectively. C_n indicates the number of n-fold-coordinated atoms (in percent). 28

4.1 Structural properties of a-Si models before DFT relaxation. The number of i-fold-coordinated atoms (in percent) in the network is indicated as n_i. Bond lengths and bond angles/widths are expressed in Å and degree, respectively. The results are obtained by averaging over 10 configurations using a nearest-neighbor cutoff value of 2.8 Å. 51

4.2 Structural properties of DFT-relaxed models of a-Si. The total number of i-fold-coordinated atoms (in percent) present in the relaxed networks is indicated as n_i. Average bong lengths and bond angles/widths are expressed in Å and degree, respectively. Asterisks indicate the use of single-zeta basis functions and the non-self-consistent Harris-functional approximation for relaxation of large models. 52

4.3 Estimated values of the peak positions, Q, in $F_i(Q)$, obtained from $Qr = (4m+1)\pi/2$ (dark gray cells in the second row for m=1 to 6) and the maxima of $G(r)$ (first column) in Å. The positions of the FSDP and the principal peak (PP) in F_is are indicated by green and red colors, respectively. The radial shells that contribute to the FSDP and the PP can be directly read off the first column. . . 59

6.1 Debye temperatures (Θ_D) of a-Si obtained from the mean-square displacements and specifc-heat data at low temperature. 101

LIST OF ABBREVIATIONS

***a*-Si**	-	Amorphous Silicon
***a*-Si:H**	-	Hydrogenated Amorphous Silicon
***c*-Si**	-	Crystalline Silicon
MD	-	Molecular Dynamics
MC	-	Monte Carlo
RMC	-	Reverse Monte Carlo
CN	-	Coordination Number
BD	-	Bond-Angle Distribution
RDF	-	Radial Distribution Function
PCF	-	Pair Correlation Function
SRO	-	Short Range Order
MRO	-	Medium Range Order
ERO	-	Extended Range Oscillations
CRN	-	Continuous Random Network
WWW	-	Wooten-Weaire-Winer
SW	-	Stillinger-Weber
DFT	-	Density Functional Theory
LDA	-	Local Density Approximation
GGA	-	Generalized Gradient Approximation
DZ	-	Double Zeta
SZ	-	Single Zeta
XC	-	Exchange-Correlation
EDOS	-	Electronic Density of State
VDOS	-	Vibrational Density of State
DWF	-	Debye Waller Factor
FSDP	-	First Sharp Diffraction Peak
PP	-	Principle Peak
FWHM	-	Full Width at Half Maxima
RMS	-	Root-Mean-Square
LS	-	Least Square
MSD	-	Mean Square Displacement
AIMD	-	*Ab Initio* Molecular Dynamics
DB	-	Dangling Bond
ZPM	-	Zero Point Motion
ZPE	-	Zero Point Energy
TLS	-	Two Level Systems

Chapter 1

INTRODUCTION

1.1 Amorphous Semiconductors

Amorphous solids are condensed phase materials having no long-range translational ordering or periodicity in their atomic arrangements. As a result, they do not exhibit a discrete diffraction pattern like crystalline materials [1, 2] . Although, amorphous materials have no structural long-range ordering, they have some structural order extended up to a few nanometer length scale, which includes short-range ($\approx$ 5 Å) to medium-range orders ($\approx$ 5-20 Å). [2, 3] Amorphous materials have significant presence in technological applications. One of the technologically promising amorphous materials type is covalent semiconductors, which are widely used in modern day electronics and photovoltaic, such as *a*-Se in electro-photography, *a*-Si:H in photovoltaic and thin-film transistors [4, 3], and amorphous chalcogenides in memory devices.

The distinct short-range order of an amorphous semiconductor gives elecronic density of state with a band gap similar to that of its crystalline counterpart, where some indistinct band edges diffuse into the band gap due to varying inter-atomic distances between the nearest neighbor atoms [5]. Except for some elemental amorphous semiconductors, such as *a*-Si and *a*-Ge, resistivity of an amorphous semiconductor depends on temperature [6], given as, $\rho(T) = \rho_0 \exp(\frac{E_g}{2k_\beta T})$ where, ρ_0, E_g, k_β, and T are the resistivity of the semiconductor, the band gap energy, the Boltzmann's constant, and temperature, respectively. In elemental amorphous semiconductors, which lie in column IV-A, V-A, and VI-A of modern periodic table, outer octet of electrons is completed by covalent bonding and sharing of pair of electrons between the neighboring atoms. The elemental semiconductors of type V-A in general show layered-like structures and VI-A and IV-A show rings or chains like three-dimensionally connected structures, respectively. The polyatomic semiconductors somehow have complex structures based on the atomic connectivity of the different atom types.

Amorphous materials can be prepared in laboratories using various methods. Some of the highly practiced methods are thermal evaporation, sputtering, chemical vapor deposition [7], and radiation induced amorphization technique [8]. Likewise, several computational methods have been developed in the past decades to generate model(s) of amorphous material(s), such as Molecular dynamics (MD) simulations [9, 10], Monte Carlo (MC) simulations [11],

genetic algorithm (GA), simulated annealing (SA) methods [12], using empirical, tight-binding, and first-principle total-energy functionals [13], each having their own advantages and limitations.

1.2 Amorphous Silicon

Amorphous silicon, *a*-Si, is a non-crystalline form of silicon, where each atom is bonded to four neighboring atoms through covalent bonds to form a tetrahedral configuration similar to that in crystalline silicon (*c*-Si). It is a prototypical covalently bonded amorphous semiconductor with a wide range of applications as electronic and photovoltaic materials. The structure of *a*-Si consist of short-range structural ordering extended up to a nano-meter, *nm*, length scale. Figure 1.1 represent a snapshot of the topology of *a*-Si and *c*-Si in diamond structure, and Figure 1.2 shows the comparison of the atomic pair correlations of *a*-Si and *c*-Si up to 8 Å radial length. The structure of *a*-Si is mainly characterized by the absence of long-range translational order of *c*-Si or the non-repeating pattern of tetrahedral units.

The lack of long-range order in *a*-Si leads to a number of structural characteristics that differ from its crystalline counterpart in diamond *c*-Si. Additionally, *a*-Si can have a coordination number, the number of bonds per atom, not always four but as low as two to as high as five. Due to high density of defects and interface states in *a*-Si, its performance in electronic devices are often limited compare to that of *c*-Si. The wider band gap of *a*-Si (1.7 eV), as compared to *c*-Si (1.1 eV), makes it more suitable for optoelectronic applications [14], such as thin-film solar cells. In *a*-Si, defects can act as the recombination centers for carriers. The high resistance of *a*-Si which restricts the recombination of carriers makes it more suitable for photoelectric uses. [14]

On the other hand, the low electron mobility in *a*-Si reduces the efficiency of *a*-Si in some electronic applications, such as field-effect transistors [15]. The high defect density of *a*-Si also prevents any substitutional doping of impurities [16] in its atomic network. Some limitations of *a*-Si as electronic materials have been overcome by passivating the dangling bonds with hydrogen, called hydrogenated amorphous silicon (*a*-Si:H). [17, 18] Passivation of dangling bonds can reduce the density of defects and improve the electrical conductivity of *a*-Si, which makes *a*-Si:H an essential electronic material for thin-film transistors [19], photovoltaics solar cells [20], digital displays [21], and optical scanners [22].

Understanding the complete structure of *a*-Si is essential to uncover details of its functional properties. In the past decades, *a*-Si is a widely studied disordered material. Many experimental [23, 24] and theoretical [25, 26] attempts have shown the structural short-range order in the atomic structure of *a*-Si, including the optical, electrical, and vibrational prop-

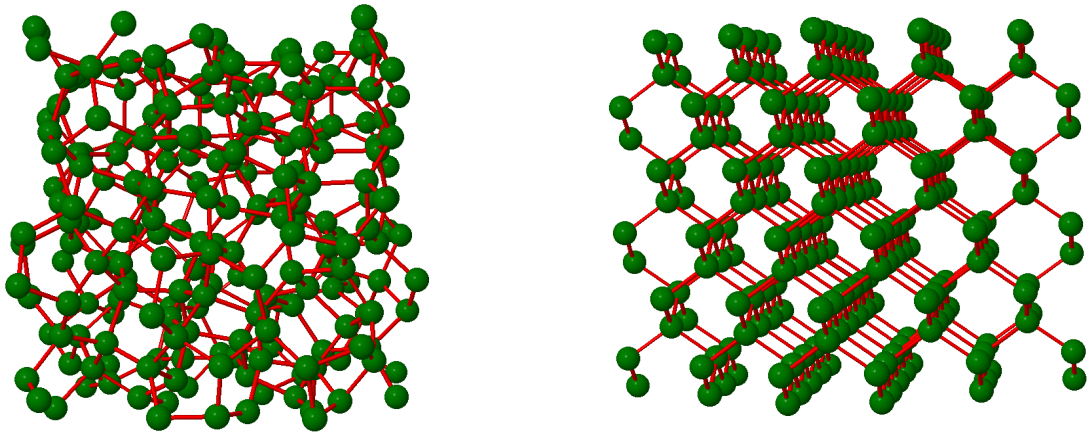

Figure 1.1: The topology of *a*-Si (left) and *c*-Si in diamond structure (right).

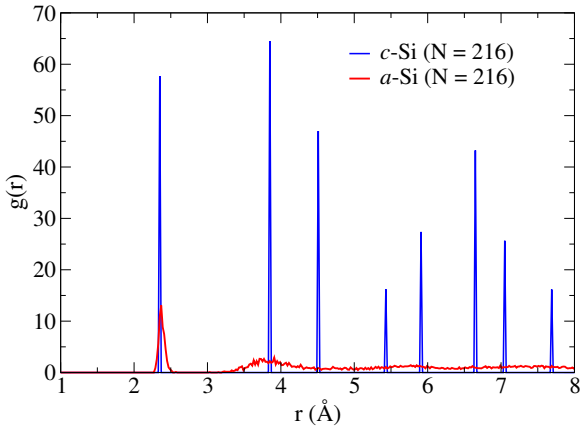

Figure 1.2: Comparison of the atomic pair correlation function of *a*-Si and *c*-Si up to 8 Å of radial separation.

erties. Experimental studies have shown that the structure of *a*-Si can considerably vary from sample to sample depending upon the preparation method and experimental conditions. The self-ion implantation technique is the most reliable method to produce the pure *a*-Si sample with no defects and voids up on relaxation [27, 28]. The comparison of the radial distribution function (RDF) of *a*-Si and *c*-Si have shown that the first and second peak of the RDF of *a*-Si are the broadened version of the peaks of *c*-Si where crystalline third peak missing in *a*-Si and the fourth and fifth peak are merged in to one.

Laaziri *et al.* (1999) [27, 28], using X-ray, and Fortner and Lannin [29], using Neutron diffraction method have measured high resolution RDFs, from the Fourier transform of structure factor S(Q) measured in large Q-range extended up to 55 $Å^{-1}$. The RDFs obtained thereafter reveals both as-implanted and annealed samples are under co-ordinated, having coordination number 3.55-3.79 and 3.88-3.90, respectively. Likewise, the bond length

and bond angle for the as-implanted *a*-Si sample are found to be 2.35 Å and 107-109° with variance of 9-11°, respectively. Since the real-space information extracted from the experimental results are based on the Fourier transform of Q-space data, Q_{max} is an important parameter to be considered in evaluation of atomic structure using experimental data. For converged or reliable value of CN, the Q-space diffraction data should be for at least 40 $Å^{-1}$, with a resolution of at least 0.1 $Å^{-1}$. To understand the actual structure of *a*-Si in atomistic level many hand made and computer generated models of *a*-Si have been purposed and studied in this recent few decades.

The earliest models of *a*-Si were the hand made models developed by Polk (1971) [30] and Connell, and Temkin (1974) [31], the models characterized by a local tetrahedral environment similar to that of *c*-Si. Later, the models were digitized by Polk and Boudreaux [32] and optimized by Steinhardt *et al.* [33] using Keating potential [34]. Henderson and Herman (1972) [35] have generated random network model of 64-atom *a*-Si system with no-dangling bonds, using periodic boundary condition and consideration of thermal and structural disorder. An *a*-Si model, as a tetrahedra packed into a regular structure in curved space, was introduced by Kléman and Sadoc (1979) [36]. As a modern approach, Wooten and Weaire (1987) [37, 26] have put forward three strategies for modeling an amorphous materials implementing the concept of the energy minimization, which are accretion (sequential addition of atoms in a cluster), molecular dynamics, and randomization followed by relaxation. Later, Wooten-Weaire-Winer [26] developed a model with each Si atom having four-fold bonds similar to *c*-Si. Barkema and Mousseau (2000) [38], improved this process further by starting from a completely random configuration instead of *c*-Si system and using Stillinger-Weber (SW) potential for total-energy relaxation. They have successfully generated large systems of *a*-Si of 1,000–4,096 atoms. The energy gap of 1.3 eV is obtained in the electronic density of state of those defect free model of *a*-Si, showing a consistency with experimental results. Using WWW algorithm and employing local relaxation techniques Vink *et al.* (2001) [39], in $O(1)$ calculation, developed 20,000-atom models of *a*-Si.

The classical and *ab-initio* molecular dynamics (MD) [40, 25, 41, 42] are the modeling methods currently popular in the field of computational material science. In molecular dynamics method, starting from a properly equilibrated Si liquid at high temperature (higher then melting temperature) the system is cooled down to a desired temperature at higher cooling rates. The system is further relaxed at that temperature to be considered as a final configuration. Atta-Fynn and Biswas (2018) [40, 41] have implemented a classical MD method to generate, till known, largest *a*-Si modles of 400,000-atom, with nearly 97% fold-fold atoms and average bond-length of 2.36 Å. Tight binding molecular dynamics [43, 9], Reverse Monte Carlo [44, 45], and constraints based data-driven methods, such as empirical

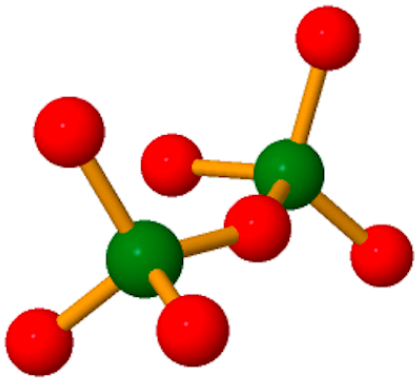

Figure 1.3: A snapshot of the topology of a-SiO_2 showing bonding of Oxygen (red spheres) and Silicon atoms (green spheres).

potential structure refinement [46], force-enhanced atomic refinement (FEAR) [47], and Information-driven inverse approach INDIA [48, 49] are some recently purposed methods each showing certain degree of promises to address the real structure of a-Si using experimental data. In this dissertation, we have presented in-depth analysis of structural, electronic, and vibrational properties of a-Si and a-SiO_2 using the atomistic models, generated via Monte-Carlo and Molecular Dynamics simulation methods.

1.3 Amorphous Silica

Amorphous silica (a-SiO_2) is one of the materials having stoichiometric composition of SiO_2. Amorphous silica is composed of three-dimensional network of silicon-oxygen (Si-O) tetrahedra, SiO_4, with varying degree of disorder. Each SiO_4 tetrahedron consist of four oxygen atoms at the corners of a tetrahedra with a silicon atom at its center. These tetrahedra can link together in different ways resulting a wide range of structure with different degree of connectivity. Among the possible Si-X (X=Si, O) bonds Si-O bond is the most stable bond with average length of $\approx$ 1.62 Å, which is smaller than exact sum of the covalent radii of Si (1.11 Å) and O atoms (0.66 Å) due to the ionic nature of the bond. A snapshot of the topology of a-SiO_2 is given in Fig. 1.3. The structure of a-SiO_2 have been studied via x-ray [50] and neutron diffraction methods [51] where Si-Si correlations and Si-O-Si bond angle are better studied via the x-ray diffraction and O-O correlations and O-Si-O bond angle are better studied via the neutron diffraction methods, based on the atomic sizes and nature of the diffraction pattern.

The lack of well-defined crystal like structure of a-SiO_2 gives some unique properties, such as high surface area, high porosity, and thermal and chemical stability [52]. Amorphous silica is one of the widely used materials in cosmetics, pharmaceutical, food industry, and construction. It can also be used as a catalyst or as a support material for catalysts [53] and has excellent thermal stability with high resistance to thermal shock.

1.4 First Sharp Diffraction Peak

The study of amorphous materials has a long history dating back to the 19th century. The development of x-ray diffraction techniques [54, 55] followed by transmission electron microscopy [56] and neutron scattering techniques [57] have allowed study of the atomic-scale structure of amorphous materials in greater detail, leading to a better understanding of the properties and behavior of such materials. Likewise, many computer generated models have been proposed to study atomic scale properties of the amorphous solids. One of the frequently studied structural feature of amorphous materials is the First Sharp Diffraction Peak, (FSDP), observed near 1-2 $Å^{-1}$ of the wavevector region of the static structure factor. In general, FSDP is a signature feature due to medium-range order in amorphous networks which shows variation with density, pressure, temperature, and composition of the system. In this dissertation, to keep consistency with previous literatures, we defined the first sharp peak in diffraction plot with intensity of about 50% or higher of that of principle peak as the FSDP of a-Si and a-SiO_2.

In tetrahedral materials having corner-sharing or edge-sharing motifs, position of the FSDP is estimated at $k_1 = \frac{2\pi}{d}$, where d is the peak position of the first peak in real-space atomic correlations of the corresponding crystalline structure [58, 59]. This explanation, however, can not explain the FSDP of liquids which barely have any crystal structure [60]. In other cases, FSDP in amorphous materials is explained as the feature due to layered or cage-like motifs and chemical ordering of clusters of voids around the cations [61].

In binary materials of types AX_2, such as $GeSe_2$ and $ZnCl_2$, FSDP arises primarily due to A-A, cation-cation, and A-X, cation-anion correlations in large ring structures extended up to 4-8 Å [60, 62, 63]. In case of a random network of structural units with dimension of the order of $2\pi/Q_0$, where Q_0 is the position of the FSDP, the FSDP arises as a result of competition of the form factor and structure factor for the centers of the units. Similarly, in binary covalent glasses, intensity of FSDP decreases with temperature due to the thermal-vibrations at high temperature which reduce the sharpness of the peaks of RDF,. Decreasing density of binary covalent materials can enhance the medium-range order resulting intensed first peak in wavevector space. On contrary, the FSDP of a-SiO_2 measured via X-ray

diffraction method have shown intensity of the FSDP increases with temperature because of its low thermal expansion [63]. In g-SiO_2, FSDP depends on the MROs which arises as the residue of crystalline MROs [58]. In alkali-silicate glasses, the dominant contribution on the FSDP arises from the radial orders of up to 10 Å [64].

In void-based models, with chemical short-range ordering of interstitial voids, Lee (1994) [65] and Elliott (1991) [61] have shown that the FSDP of binary glasses arising as a pre-peak in the concentration-concentration partial structure factor, which in liquid $ZnCl_2$ depends on the void-void correlations [66]. For monoatomic systems, such as a-Si and a-Ge, only a few explanations have been reported indicating the radial ordering of 10-20 Å is the factor behind the origin of the FSDP. In a-Si and a-SiO_2, different experiments have reveal the position of the FSDP increases linearly with density of the system. [67, 68, 69] Despite many experimental and computational attempts of last few decades a universal explanation of the FSDP is yet a controversial topic. [66, 63, 61]. In general, the FSDP in glasses should be independent of the dimensionality, validity for covalent and ionic bonding, and useful to estimate required parameters. [63].

The FSDP in liquids and glasses is a ubiquitous feature arises due to MRO in network structure [65, 63, 70, 71]. In amorphous materials MRO refers the regime due to large rings structure, layer-like ordering, and the interstitial voids [65, 61]. The main objective of this dissertation is to discuss the origin and structure of the FSDP in the covalent monoatomic and binary solids, a-Si and a-SiO_2 as the prototypes, in atomistic point of view. Also, a functional relation between radial correlations and the FSDP of tetrahedral network models of nearly 100% four-fold disorderd network of a-Si is analyzed via information-theoretical point of view.

1.5 Outline of the dissertation

Chapter 2 presents a brief discussion of the simulation techniques, which are partly or fully implemented in this study for modeling a realistic configurations of a-Si and a-SiO_2. In addition, a brief discussion of the structural descriptors of amorphous materials, the electronic density of state, Debye-Waller factor, and atomic dynamics is given.

A discussion about the origin of the extended-range oscillations in real-space atomic correlation in ultra-large models ($\approx$ 400,000-atom) of a-Si is presented in Chapter 3. Using various network of Si atoms having different degree of (dis)order and distorted c-Si systems obtained from diamond c-Si, extended-range ordering of a-Si in real space atomic correlation is studied in atomistic point of view. In addition, an analysis of the impact of the EROs on the first sharp diffraction peak of a-Si is discussed in details.

Chapter 4 and 5, present the analysis of the origin and structure of the first sharp diffraction peak of the structure factor of covalent networks of *a*-Si and *a*-SiO_2, respectively. A functional relation is observed between the position of the FSDP and average cubic radial distance of the atoms in second radial shell of *a*-Si, which is reported in a literature for the first time. The contribution from the real-space atomic correlations of *a*-Si and *a*-SiO_2 to the FSDP is discussed on the basis of the atomic correlations from diffrent radial shells.

In Chapter 6, atomic mean square displacement of Si atoms of *a*-Si is studied in harmonic approximation using lattice dynamics calculation method. The dynamics of atoms having a perfect four-fold bonding and atoms having dangling-bond (three-folds) are examined for nearly 100% four-fold networks and the networks with clustered or isolated dangling bonds and voids. Finally, the summary of the dissertation is stated in Chapter 7. Chapter 3 and 4 are adapted from the publications published in PRB (2022) [72] and PSS(b) (2021) [69], respectively.

Chapter 2

COMPUTER MODELING AND CHARACTERIZING THE STRUCTURE OF AMORPHOUS MATERIALS

2.1 Computer Modeling of amorphous materials

Computer generated models are essential in understanding the structure and properties of the amorphous materials from an atomistic point of view. Till now, various modeling techniques have been implemented in the study of functional materials, such as semiconductors, energy materials, photoelectric materials, and biomaterials. Different modeling techniques have their unique advantages and limitations based on the approximations used. A brief discussion of the computer simulation methods, which we have partly or wholly implemented for generation of the atomistic models implemented in this disseration work, is given in this section.

2.1.1 Continuous Random Network Model

Modeling a material as a continuous random network (CRN) [73] of constituent atoms is an ideal method for isotropic and homogeneous amorphous semiconductors, such as *a*-Si and *a*-Ge. In this method, materials are considered a random arrangement of atoms bonded with flexible bonds that can rotate or vibrate to allow a high degree of structural disorder. The atomic arrangement is constrained by the material's specific density and chemical composition. The continuous network between the constituent atoms ensures the material is not just a collection of isolated clusters of atoms. For amorphous semiconductors, their network structure is well represented by the continuous random network (CRN) model introduced by Zachariasen [73] in 1932. The quality of a CRN model can be assessed in terms of topological and configurational properties, including coordination number, bond-angle distributions, and deformation energy.

2.1.2 Wooten-Weaire-Winer (WWW) method

Wooten, Weaire, and Winer, in the early 1980s, have developed a model representing an amorphous material as a random packing of spheres with different radii, known as the Wooten-Weaire-Winer (WWW) method.[26]. The basic steps used for the generation of a

computer model of an amorphous material using the WWW method are as follows,
i) Start with a cubic periodic crystalline structure,
ii) Randomize the system using sequence of bond switching while preserving the tetrahedral bonding and introducing five- and sevenfold rings,
iii) At the end of a sequence of bond switching, relax the system using Keating potential within the constraints of the neighbor list,
iv) Accept or reject the model using Monte-Carlo for the minimum energy.

In this dissertation, we have implemented the improvised WWW method modified by G. T. Barkema and N. Mousseau [38] to generate the CRN models of *a*-Si, the details of the modified method is further discussed in Chapter 4.

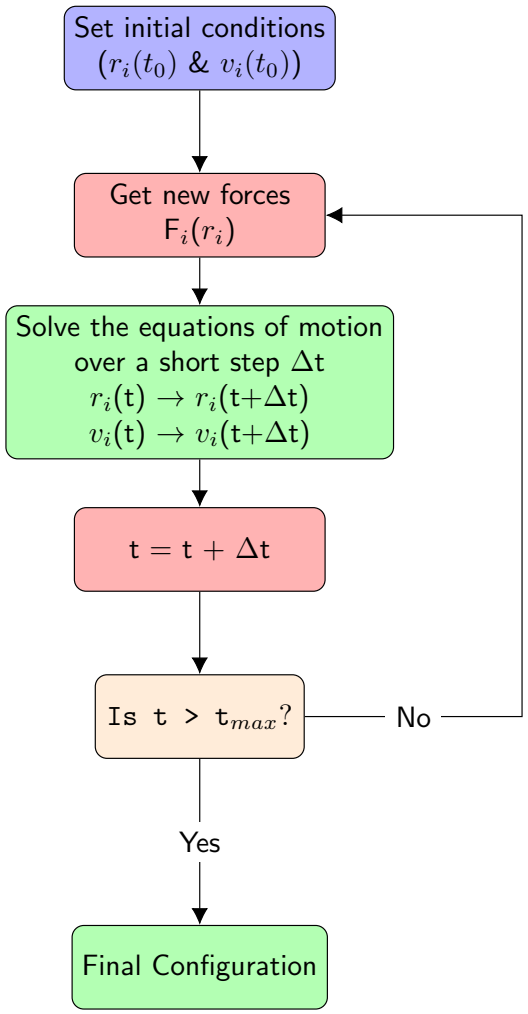

Figure 2.1: A general flowchart of a molecular dynamics simulation method.

2.1.3 Molecular Dynamics (MD) Method

The molecular dynamics (MD) simulation is a simulation method based on the time evolution of a system of interacting particles, such as atoms or molecules, which relies on the empirical force fields that consist of the set of equations used to calculate the potential energy and forces from particle coordinates. The position and velocity of the particles at discrete time steps are calculated by integrating Newton's equations of motion using different algorithms, such as velocity and leap-frog Verlet algorithm [74, 75].

In MD simulation, each atom is considered as a particle of mass m_i. The force, F_i, is then calculated as,

$$F_i = -\frac{\partial V(r_1,...,r_N)}{\partial r_i} = m_i \frac{\partial^2 r_i}{\partial t^2} \tag{2.1}$$

where, r_i is the instantaneous position of the i^{th} particle.

The inter-atomic potentials, such as Keating potentials [34] and Stillinger-Weber (SW) potentials [76], can be implemented in the simulation of covalent amorphous materials such as *a*-Si. In general, MD simulation follows an initialization of atomic position and velocity, equilibrium of the system over a time step using force equations, and model finalization. In actual calculation, periodic boundary conditions are required to avoid any surface related artifacts. A simple flowchart showing the steps of an MD simulation is presented in Fig. 2.1.

The MD simulation method is suitable for investigating the structure and dynamics of amorphous materials to gain insights into how the properties of a material get influenced by factors such as temperature, pressure, and composition. Additionally, the MD simulation technique is beneficial for understanding the mechanisms of crystallization, melting, and deformation of materials [77].

2.1.4 Monte Carlo Method

The Monte Carlo method [78, 79] is a random sampling technique, can be used estimate the properties of interest, such as thermal and mechanical properties, by generating random configurations and averaging over a large number of configurations of a material system.

The Metropolis Monte Carlo technique, based on Markov chain Monte Carlo (MCMC) algorithm [80], is a powerful MC method for simulating systems with many degrees of freedom. A general flowchart showing steps of an MCMC simulation is given in Fig. 2.2. An overview of the steps of the Metropolis Monte-Carlo method is as follows [80];

1. Choose an initial configuration and calculate the energy (E),

2. Generate a new configuration by making a small change to the current configuration, by randomly moving an atom or molecule, or by changing the orientation of an atom or

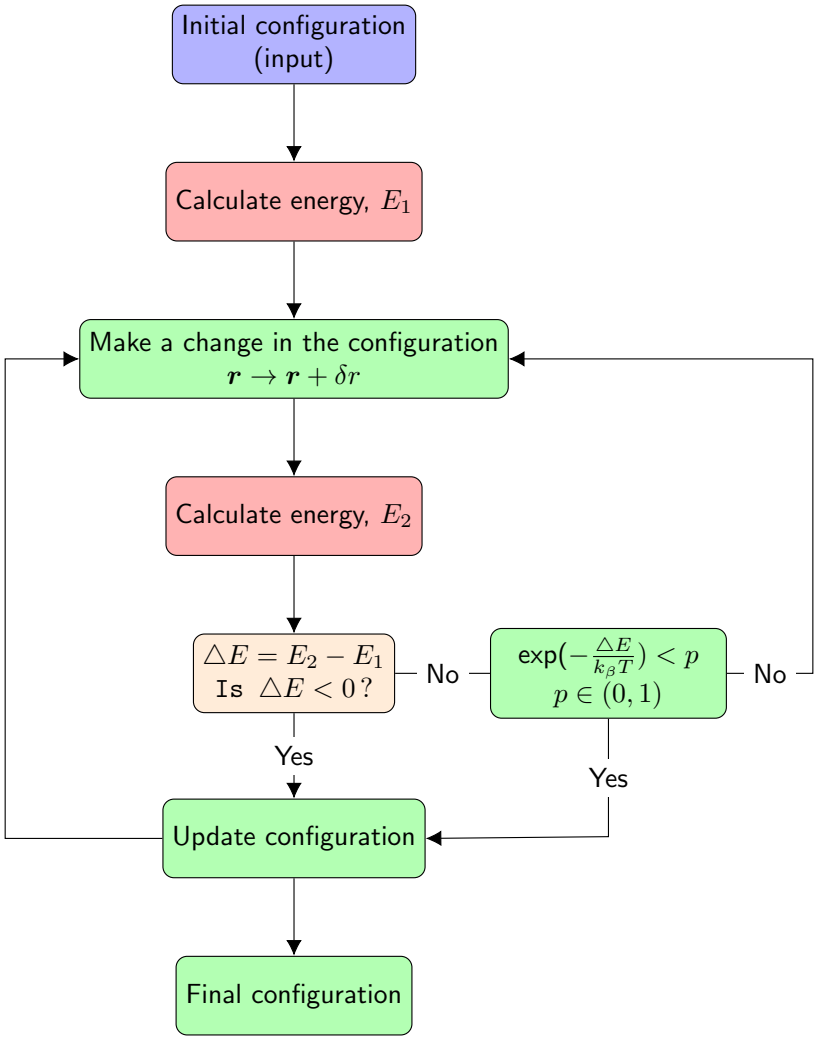

Figure 2.2: A simplified flowchart of the Markov chain Monte Carlo (MCMC) algorithm.

molecule, and calculate the energy (E') of the new configuration.

3. Calculate the change in energy ($\Delta E = E' - E$)

If $\Delta E \leq 0$, accept the new configuration.

If $\Delta E > 0$, accept the new configuration with a probability equal to $\exp(-\Delta E/kT)$, where k is the Boltzmann constant and T is the temperature.

4. Repeat steps 2-3 for a large number of iterations to generate an energy-minimized configuration.

2.2 First principles modeling: Density Functional Theory (DFT) method

Density functional theory (DFT) is a first-principle quantum mechanical method that does not require higher-order parameters for modeling a configuration. Since Hohenberg and Kohn first applied it in 1964 [81], DFT has been widely used in physics, chemistry, and materials science. In a DFT calculation, the ground state properties of many-body systems can be uniquely determined by using electron density rather than solving Schrödinger wavefunctions. It is considered an efficient method to investigate the electronic structure of atoms, molecules, and solid materials.

In general, DFT calculation is based on the two unique theorems known as Kohn-Hohenberg theorems [81], stated as (i) the ground-state energy of a many-body system is a unique functional of the electron density n($\boldsymbol{r}$), i.e., $E = \mathcal{F}n(\boldsymbol{r})$ and (ii) the actual electron density is the electron density that minimizes the energy of the overall functional.

Kohn and Sham (1965) [82] have introduced an approximation method for treating an inhomogeneous system of interacting electrons, considering the exchange and correlation portions of the chemical potential of a uniform electron gas as additional effective potentials in self-consistent equations for the ground state. The Kohn-Sham equation, as a single particle wave equation, is given as,

$$\mathcal{E}_i \psi_i(\boldsymbol{r}) = [\frac{-\hbar^2}{2m_e}\nabla^2 + v_{eff}(\boldsymbol{r})]\psi_i(\boldsymbol{r}) \tag{2.2}$$

where, $\psi_i(r)$, $\mathcal{E}_i$, and v_{eff} are the electron orbitals, corresponding eigen values, and effective potential, respectively. The effective potential, v_{eff}, in terms of the external potential, V_{ext}, and electron density, $n(\boldsymbol{r})$, is given as,

$$v_{eff}(\boldsymbol{r}) = V_{ext}(\boldsymbol{r}) + \int \frac{n(\boldsymbol{r'})}{|\boldsymbol{r}-\boldsymbol{r'}|}dr' + \frac{\delta E_{xc}[n(\boldsymbol{r})]}{\delta n(r)} \tag{2.3}$$

where, E_{xc} is the exchange and correlation energy (XC) functional.

Based on the functions used to obtain the required wave equations, DFT calculations are specified as spatially localized (cluster-type), spatially extended (bulk-type), and plane wave (spatially extended, periodic functions) calculations [83, 84]. To derive the solutions of Kohn-Sham equations one requires the XC-functional. Since the proper form of XC functional has yet to be discovered, various approximations have been implemented in the actual calculations. Some of the widely used approximations are Local Density Approximation (LDA) [85] and Generalized Gradient Approximation (GGA) [86]. A flowchart showing the steps of a DFT calculation using a self-consistent force field is given in Fig. 2.3.

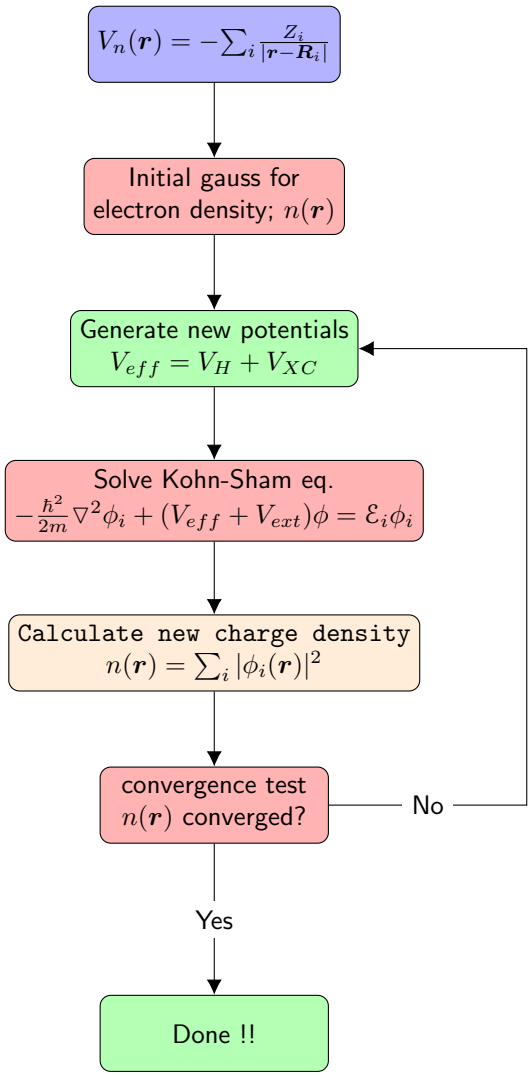

Figure 2.3: Simplified flowchart of the self-consistent Khon-Sham DFT calculation.

2.2.1 Local Density Approximation (LDA)

The LDA method is so called local approximation method as the electron exchange correlation energy at a point is considered a function of energy at that point. The XC-energy functional in LDA method is given as [85],

$$E_{XC}^{LDA}[n(\boldsymbol{r})] = \int n(\boldsymbol{r})\mathcal{E}_{XC}[n(\boldsymbol{r})]dr$$

where, $\mathcal{E}_{XC}$ is the energy density obtained as the sum of individual exchange and correlation contributions, i.e., $\mathcal{E}_{XC} = E_X + E_C$, which is the exchange-correlation energy of an electron in a non-interacting homogeneous electron gas of the electron density $n(\boldsymbol{r})$. This approximation is best for the systems with slowly varying charge density.

2.2.2 Generalized Gradient Approximation (GGA)

In GGA method, XC-energy functional is considered as a function of electron density and its gradient. Here, the XC-energy functional is [86],

$$E_{XC}^{GGA}[n(\boldsymbol{r})] = \int n(\boldsymbol{r})\mathcal{E}_{XC}[n(\boldsymbol{r}), \triangledown n(\boldsymbol{r})]dr$$

Since numerous distinct functionals can be used to gain information from the gradient of the electron density, several functionals have been implemented in the GGA method, among which Perdew-Wang (PW91) [21] and Perdew-Burke-Ernzerhof (PBE) [20, 22] functional are the two frequently used functionals.

2.3 Structural descriptors of amorphous materials

In general, amorphous materials are isotropic materials, having properties identical in all directions. Compared to the periodic structure of crystalline materials, amorphous materials show significant variation in their local atomic environment. In amorphous materials, the number of nearest neighbors and neighboring distances can characterize the real-space local atomic environments. In this dissertation, we have implemented the following descriptors to analyze the atomic distribution of amorphous materials up to various length scales.

2.3.1 Static Structure Factor

For an electron with charge distribution, ρdV, the scattering intensity in terms of the scattering factor, f_e, is given as [87],

$$I = f_e f_e^* \tag{2.4}$$

where,

$$f_e = \int \exp[\frac{2\pi i}{\lambda}(\boldsymbol{s} - \boldsymbol{s}_0).\boldsymbol{r}]\rho(\boldsymbol{r})dV \tag{2.5}$$

The scattering factor for an electron in terms of the scattering vector, $k = \frac{4\pi \sin\theta}{\lambda}$, assuming spherical symmetry, is given as,

$$\begin{aligned} f_e &= \int_{r=0}^{\infty}\int_{\phi=0}^{\pi} \exp[ikr\cos\phi]\rho(r)\,2\pi r^2 \sin\phi\, d\phi\, dr \\ &= \int_0^{\infty} 4\pi r^2 \rho(r)\frac{\sin kr}{kr}dr \end{aligned} \tag{2.6}$$

For the atoms with n electrons, the atomic scattering factor is the sum of the scattering factor of each individual electrons, i.e.,

$$f = \sum_n f_{en} = \sum_n \int_0^\infty 4\pi r^2 \rho_n(r) \frac{\sin(kr)}{kr} dr \tag{2.7}$$

The scattering intensity from an assembly of N particles, using Born approximation is then given as,

$$I = \sum_{i=1}^{N} \sum_{j=1}^{N} f_i f_j \exp[\frac{2\pi i}{\lambda}(\boldsymbol{s} - \boldsymbol{s}_0).\boldsymbol{r}_{ij}] \tag{2.8}$$

For a three dimensional isotropic system,

$$\langle \exp[\frac{2\pi i}{\lambda}(\boldsymbol{s} - \boldsymbol{s}_0).\boldsymbol{r}_{ij}] \rangle = \frac{\sin(kr_{ij})}{kr_{ij}} \tag{2.9}$$

Hence, Eq. 2.8 becomes,

$$I = \sum_{i=1}^{N} \sum_{j=1}^{N} f_i f_j \frac{\sin(kr_{ij})}{kr_{ij}} \tag{2.10}$$

Case I: Monoatomic System:

For a system with N identical atoms Eq. 2.10 can be written as,

$$\begin{aligned} I &= \sum_i f^2 + \sum_i \sum_{j \neq i} f^2 \frac{\sin(kr_{ij})}{kr_{ij}} \\ &= \sum_i f^2 + \sum_i f^2 \int \rho_i(r_{ij}) \frac{\sin(kr_{ij})}{kr_{ij}} dV_j \\ &= \sum_i f^2 + \sum_i f^2 \int 4\pi r^2 [\rho(r) - \rho_0] \frac{\sin(kr)}{kr} dr + \sum_i f^2 \int 4\pi r^2 \rho_0 \frac{\sin(kr)}{kr} dr \end{aligned} \tag{2.11}$$

where, $\rho(r) = \langle \rho_i(r_{ij}) \rangle$, is the average density function. For, amorphous materials with no long-range order, at large r $(\rho(r) - \rho_0) \to 0$. Also, the third term in Eq. 2.11, which depends on the small angle scattering of the order of $k \leq 2\pi/R$, is neglegible. For finite small angle scattering Eq. 2.11 becomes,

$$I = Nf^2 + NF^2 \int_0^\infty 4\pi r^2 [\rho(r) - \rho_0] \frac{\sin(kr)}{kr} dr \tag{2.12}$$

The static structure factor, S(k), in terms of the scattering intensity I, is given as,

$$S(k) = \frac{I}{Nf^2} = 1 + \frac{4\pi\rho_0}{k} \int_0^\infty r[g(r) - 1] sin(kr) dr$$

where, $g(r) = \rho(r)/\rho_0$, is the atomic pair correlation function.

Case II: Polyatomic System:

For a material having n components Eq. 2.12 can be generalized as,

$$\frac{I}{N} = \sum_{i=1}^{n} x_i f_i^2 + \sum_{i=1}^{n}\sum_{j=1}^{n} x_i f_i x_j f_j \int_0^\infty 4\pi r^2 \frac{\rho_{ij}(r)}{x_j}\frac{\sin(kr)}{kr}dr \tag{2.13}$$

$$-[\sum_{i=1}^{n} x_i f_i]^2 \int_0^\infty 4\pi r^2 \rho_0 \frac{\sin(kr)}{kr}dr \tag{2.14}$$

where, x_i, f_i, and $\rho_{ij}(r)$ are the atomic fraction, scattering factor, and average number of $'j'$ atoms per unit volume at distance r from the atom $'i'$. With, the average density function, $\rho(r)$, Eq. 2.14 becomes,

$$\frac{I}{N} = \langle f^2 \rangle + \langle f \rangle^2 \int_0^\infty 4\pi r^2 [\rho(r) - \rho_0]\frac{\sin(kr)}{kr}dr \tag{2.15}$$

The reduced scattering intensity factor is hence,

$$F(k) = k\big[\frac{\frac{I}{N} - \langle f^2 \rangle}{\langle f \rangle^2}\big] = \int_0^\infty 4\pi r[\rho(r) - \rho_0]\sin(kr)dr \tag{2.16}$$

Since the structure factor is a one-dimensional projection of diffraction from a three-dimensional material, information observed via the diffraction structure factor alone is not sufficient to reveals the actual atomic arrangements in an amorphous material. To understand the natural structure of the a material, in addition to the structure factor, the radial distribution function, RDF, is an equally valuable descriptor to be consider.

2.3.2 Radial Distribution Function

The radial distribution function (RDF) [87], $J(r)$, is a statistical measure of atomic two-body correlations. It provides information about the local ordering or the correlations between the position of atoms, molecules, or nanoscale building blocks at molecular length scales. Radial distribution function is useful in finding the strength of intermolecular interactions. In experiments, the pair correlation function, $g(r)$, can be obtained as the Fourier transform of the diffraction structure factor, S(Q), given by,

$$g(r) = 1 + \frac{1}{2\pi^2 \rho_0}\int_0^\infty \frac{Q[S(Q) - 1]\sin(Qr)}{Q}dQ \tag{2.17}$$

and, the RDF is,

$$J(r) = 4\pi\rho_0 r^2 g(r)$$

For a computer generated model consist of N particles distributed within a volume V, atomic pair correlation function (PCF), is given as,

$$g(r) = \frac{\rho(r)}{\rho_0} \tag{2.18}$$

where, $\rho_0 = N/V$ is the number density, and $\rho(r)$ is the density function which will be zero at $r < r_0$ and tends to ρ_0 at $r \gg r_0$. Some important features of radial distribution function are,

i) position of the first peak of the RDF indicates average bond length of the particles,

ii) the first nearest neighbor cut-off distance is the first minima (depth) of the RDF,

iii) sharpness of the peaks of the RDF indicates the degree of atomic ordering,

iv) area under a first peak of the RDF indicates the coordination number,

v) the RDF is useful in calculation of the thermodynamical properties, such as internal energy and pressure of a system.

2.3.3 Bond angle Distribution and Ring Statistics

The bond-angle distribution (BD) is a statistical measure that describes the distribution of bond angles between pair of bonds of an atom with its nearest neighbors as a three-body correlation. The bond-angle distribution provides information about the local ordering of atoms, molecules, or nanoscale building blocks in a material and the strength and type of intermolecular interactions. Bond-angle distribution of a system can be evaluated using X-ray diffraction and neutron scattering techniques.

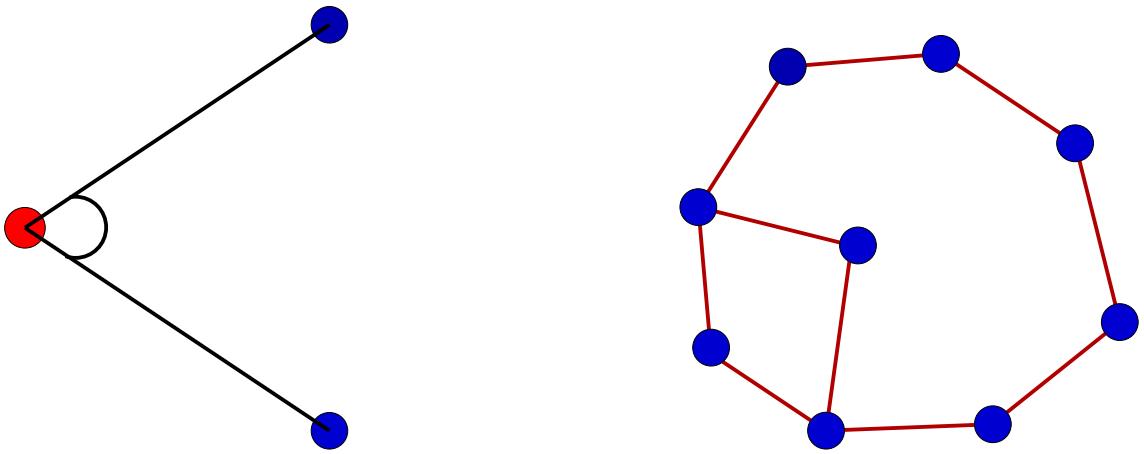

Figure 2.4: A toy diagram showing a bond angle (left) between the an atom (red) and its first nearest-neighbor atoms (blue) and the rings in a network of 9 atoms, the rings are of size 4 and 8 (right).

Likewise, ring statistics is a structural descriptor that can characterize the local structure of amorphous materials. A proper ring should satisfy some specific criteria, such as King's criterion [88], shortest path criterion [89], and primitive ring criterion [90]. Based on these criteria, a ring is the shortest closed path of bonds that starts and ends at the given atomic site and is not decomposable to smaller rings. In general, ring statistics analyzes a series of nodes (atoms) connected in a non-overlap closed connection. Each ring is then characterized by its size, either the total number of atoms of the ring or the number of network-forming nodes. In the first method, the N-membered ring is defined as a ring with N nodes, while in a later definition, it is a ring containing 2N nodes. The ring statistics provide a snapshot of the connectivity of networks, such as short-range order and the local packing of atoms, molecules, or building blocks in an amorphous material. The size and distribution of rings indicate the degree of structural disorder, the presence of structural motifs, and the strength of atomic interactions. A perfect diamond crystal contains 6-fold rings, which can be different for the covalent amorphous materials having topological disorder. Rings of large sizes are due to defects or voids in the structure. A ring of $(n \geq 4)$ indicates the topological order beyond short-range order. Figure 2.4 represents a toy diagram showing a) a bond angle and b) 4 and 8-fold rings in a network of 9 atoms.

2.4 Electronic properties

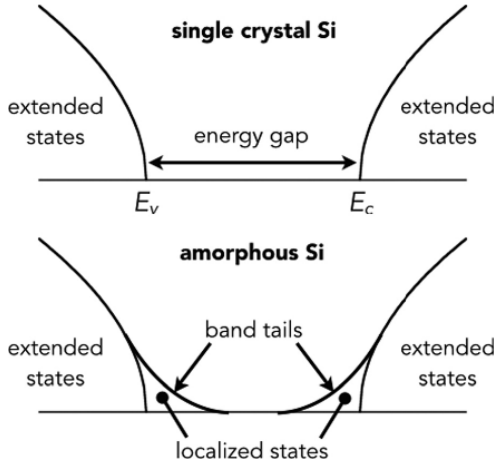

Figure 2.5: A diagram representing electronic density of states in a single crystal silicon and amorphous silicon, localized states can emerge within the band gap of EDoS of *a*-Si. [91]

Amorphous materials exhibit short-range structural ordering similar to their crystalline counterparts. Even though there is SRO, it is hard to predict the most extended separation

between the bonded atoms. Also, due to the absence of long translational order Bloch theorem [92] is non-fully applicable to describe the electronic properties of amorphous semiconductors. In amorphous semiconductors, such as *a*-Si, the valence electrons often are tightly bound or localized because of the stronger binding forces between the covalently bonded atoms. As a consequence of tightly bound valence electrons, the electronic density of state (EDoS) for the localized states extended into the band gap between the energy bands of the valance and conduction bands, resulting the band tails. In some amorphous materials, band tails could overlap depending on the degree of impurities. Figure 2.5 represents a schematic diagram showing the electronic density of state in a single crystal silicon and amorphous silicon [91], indicating the evidence of band tails in EDoS of an amorphous solid.

2.5 Debye-Waller Factor

In x-ray diffraction experiments, to measure the intensity of the scattering amplitudes, crystals or amorphous materials are considered as a perfectly rigid body. In real samples, the atoms in a material don't have perfect stable position but will vibrate from the mean position, for two reasons. The first reason is called zero-point fluctuation, due to the uncertainty principle of quantum mechanics, which occurs even at 0 K and is independent of temperature. The next is by elastic waves or phonons, which are temperature dependent. Regardless the cause, uncertainty of atomic position reduces the magnitude of the interference of the scattering waves from different atoms of a system.

The atomic form factor [87] of a system with single element is given as,

$$\mathbf{f} = \mathbf{f_j} \exp(-\mathbf{i}\boldsymbol{q}.\boldsymbol{r}_j) \tag{2.19}$$

At a finite temperature, $\boldsymbol{r}_j = \boldsymbol{r}_0 + \boldsymbol{u}_j$, where $\boldsymbol{r}_0$ is the mean position and $\boldsymbol{u}_j$ is the vibrational displacement of the atom. The average atomic form factor is then,

$$\begin{aligned} \mathbf{f} &= f_j \exp(-i\boldsymbol{q}.\boldsymbol{r}_{0j}) \langle \exp(-i\boldsymbol{q}.\boldsymbol{u}_j) \rangle \\ &= f_j \exp(-i\boldsymbol{q}.\boldsymbol{r}_{0j}) \exp(-\langle u^2 \rangle q^2) \end{aligned} \tag{2.20}$$

Hence, the total scattered intensity from an atom is,

$$\begin{aligned} I &= \boldsymbol{f}.\boldsymbol{f}^* \\ &= f_j^2 \exp(-i\boldsymbol{q}.\boldsymbol{r}_{0j}) \exp(i\boldsymbol{q}.\boldsymbol{r}_{0j}) \exp(-2\langle u^2 \rangle q^2) \\ &= I_0 \exp(-2M) \end{aligned} \tag{2.21}$$

where, $M = \langle u^2 \rangle . q^2$. For $q = 4\pi \sin\theta / \lambda$,

$$\begin{aligned} M &= \langle u^2 \rangle q^2 \\ &= \frac{8\pi^2 \sin^2\theta \langle u^2 \rangle}{\lambda^2} \end{aligned} \tag{2.22}$$

This intensity reduction factor, e^{-2M}, is known as the Debye-Waller factor.

2.6 Atomic dynamics

The study of the dynamical properties of amorphous materials is not a trivial problem. The adiabatic (Born-Oppenheimer) approximation [93, 94]- with potential energy given in terms of the nuclear coordinates, and harmonic approximation [95]- with potential expanded in the power of the displacement, are the two approximations used in calculation of atomic vibrational excitations. In harmonic approximation, elementary vibrational excitations are considered non-interacting and independent. The inclusion of anharmonic terms includes the interaction between the vibrational excitations.

In general, the hamiltonian for lattice vibrations is given as,

$$H = \sum_{i\alpha} \frac{1}{2} M_i \dot{x}_{i\alpha}^2 + \frac{1}{2} \sum_{\substack{i\alpha \\ i'\alpha'}} \Phi_{i\alpha}^{i'\alpha'} x_{i\alpha} x_{i'\alpha'} \tag{2.23}$$

where, i, is the atom index and $\alpha = (x, y, z)$ is the cartesian coordinates in three dimension. M and $x_{i\alpha}$ are the mass and instantaneous displacement from equilibrium position of an atom, respectively. The $\Phi_{i\alpha}^{i'\alpha'}$ is a $3N \times 3N$ matrix called force-constant matrix, for a system with N atoms, is given as,

$$\Phi_{i\alpha}^{i'\alpha'} = \frac{\partial^2 V(r)}{\partial x_{i\alpha} \partial x_{i'\alpha'}} \tag{2.24}$$

The corresponding equation of motion is,

$$M_i \ddot{x}_{i\alpha} = -\sum_{i'\alpha'} \Phi_{i\alpha}^{i'\alpha'} x_{i'\alpha'} \tag{2.25}$$

considering the simple harmonic motion, solution for Eq. 2.25 is,

$$x_{i\alpha}(t) = \frac{u_{i\alpha}}{\sqrt{m_i}} e^{(i\omega t)} \tag{2.26}$$

since $u_{i\alpha}$ is time independent, using equations 2.25 and 2.26, we have

$$\omega^2 u_{i\alpha} = \sum_{i'\alpha'} D_{i\alpha}^{i'\alpha'} u_{i'\alpha'} \tag{2.27}$$

where, $D_{i\alpha}^{i'\alpha'} = \frac{\Phi_{i\alpha}^{i'\alpha'}}{\sqrt{m_i m_{i'}}}$ is a real-symmetric matrix, called dynamical matrix. Using the diagonalized dynamical matrix, equation 2.27 can have $3N$ real eigenvalues, ω_j^2, called square frequency with $3N$ normal modes, $u_{i\alpha}^j$, for each frequency, ω_j.

Chapter 3

EXTENDED-RANGE ORDER IN AMORPHOUS SILICON

The discussion presented in this chapter has been adopted from a publication by **D. Dahal, S. R. Elliott, P. Biswas; Extended-range order in tetrahedral amorphous semiconductors: The case of amorphous silicon,** *Phys. Rev. B* **105, 115203**

3.1 Introduction

The structure of amorphous silicon (*a*-Si) is well represented by the continuous random network (CRN) model of Zachariasen [96]. The CRN model of *a*-Si suggests that each atom is bonded to four neighboring Si atoms, which form an approximate tetrahedral atomic arrangement in the amorphous environment. The network is topologically distinct from its crystalline counterpart (*c*-Si) owing to the presence of 5-member and 7-member rings. In addition, a considerable number of hexagonal rings and a few higher-member rings are also present in the amorphous network. The pair-correlation function (PCF) of *a*-Si obtained from CRN models indicates that radial correlations typically extend up to a distance of 15 Å. Although the actual structure of laboratory-grown samples of *a*-Si may differ from this simple CRN picture, except for a few properties, the CRN model provides an overall good description of structural, electronic, and vibrational properties of *a*-Si that mostly rely on the short-range order ($\approx$ 5 Å) and, to a lesser extent, the medium-range order ($\approx$ 5–20 Å) of the network.

Although the structure of *a*-Si has been extensively studied by using computer-generated models on the radial length scale of 10–15 Å, there exist only a few studies [61, 97, 98, 41] that discuss the network structure of *a*-Si on the medium-range length scale of 20 Å and beyond. This is partly due to the fact that structural and electronic properties of *a*-Si are generally found to be not particularly dependent on the medium-range structure beyond 15 Å and in part to the computational complexity of conducting quantum-mechanical calculations, using density-functional theory (DFT), for large models. However, this observation does not necessarily imply that no medium-range structure exists in *a*-Si [99]. In this paper, we address this aspect of the problem by studying the network structure of *a*-Si using atomistic models of sizes 21,952 and 400,000 atoms. In particular, we examine two important aspects

of the medium- and extended-range structures of *a*-Si that have been reported in the literature. The first problem involves the presence of weak but noticeable radial oscillations in the PCF at distances of 20–40 Å. This was first reported by Uhlherr and Elliott [100] and it was given the name extended-range oscillations in the PCF of *a*-Si. The second issue is directly related to the first and it concerns the effect of the medium-range order beyond 15 Å, and possibly the extended-range order, on the first sharp diffraction peak (FSDP) of *a*-Si. The latter corresponds to the first peak of the static structure factor [101], $S(Q)$, at $Q = 1.99$ Å^{-1} in *a*-Si. In the following, we use the term medium-range order (MRO) to imply ordering on the length scale of 5–20 Å, whereas the term ERO indicates structural ordering beyond 20 Å, including extended-range oscillations.

The role of the medium-range order (MRO) in amorphous networks has been studied extensively in an effort to understand structure-property relationships in network-forming glasses, for example, oxides [102, 103, 104, 105, 106] and chalcogenides [107, 108, 109, 110, 111]. The MRO in these systems typically manifests itself as the FSDP, and the position, width, and intensity of the FSDP characterize the length scale associated with the MRO. The results from numerous experimental [112, 113, 114, 115, 116, 104, 117] and computational studies [61, 118, 119, 120, 121, 64, 122] indicate that the MRO/ERO in glassy systems can extend up to a distance of 30 Å and that it can play an important role in determining a number of materials properties of network-forming glasses. By contrast, results for tetrahedrally-bonded elemental amorphous semiconductors, such as *a*-Si and *a*-Ge, are few and far between. Uhlherr and Elliott [100] studied the presence of extended-range oscillations in *a*-Si by analyzing experimental neutron-diffraction data of Fortner and Lannin [29] and the pair-correlation data obtained from atomistic models of size 13,824 atoms. [123] The authors concluded, via the Fourier inversion of the structure factor in the vicinity of the FSDP region, that the radial oscillations can extend to at least 35 Å and that it arises from the propagation of second-neighbor radial atomic correlations. Recently, Roorda et al. [124] reported the presence of ERO in amorphous Si/Ge using x-ray diffraction measurements at high resolution. The PCF obtained in their study from the Fourier transform of diffraction data shows the presence of ERO beyond 20 Å in both *a*-Si and *a*-Ge samples. The authors also noted that the (spatial) periodicity and decay length of the MRO/ERO increase upon thermal annealing. In view of these observations, the main task of the present study is to examine the presence of the ERO in large realistic models of *a*-Si by a direct analysis of the pair-correlation function and their partial counterparts associated with distant coordination shells of amorphous silicon.

The rest of the chapter is arranged as follows. In section 3.2, we have provided a description of the computational methods employed here to generate atomistic models of

a-Si and a set of partially-ordered networks of Si atoms. This is followed by results and discussion in section 3.3. The origin of the ERO is addressed from a real-space point of view of the network structure of amorphous silicon. The relation between the ERO and structure of the FSDP is also examined in this section by constructing a semi-empirical expression for the structure factor of *a*-Si in the Gaussian approximation. This is followed by conclusions of our work in section 3.4.

3.2 Computational method

The present study involves the use of three different sets of models. The first set consists of *a*-Si models obtained from using the Wooten-Winer-Weaire (WWW) [26, 38] algorithm. The second set comprises *a*-Si models produced from large-scale molecular-dynamics (MD) simulations. The third set includes three different types of partially-ordered networks of Si atoms, denoted by M1, M2, and M3. These networks are not realistic models of *a*-Si; they have varying degrees of radial ordering in the respective PCF up to a radial length of 6 Å. In order for the ERO to manifest in the PCF of *a*-Si at radial distances of 20–40 Å, it is necessary for the models to be sufficiently large, consisting of a few tens to several tens of thousands of atoms. To this end, the sizes of the models were chosen to be 21,952 atoms and 400,000 atoms, which suffice to establish an unambiguous presence of the ERO in the PCF. In this study, we generated a set of three independent M1/M2/M3 and WWW models and three MD models for the purpose of configurational averaging of data.

The MD models were produced by initially placing 400,000 Si atoms randomly in a cubic simulation cell of length 202.4 Å, so that no two atoms could be at a distance of less than 2 Å. The mass density of the models corresponds to 2.26 g.cm^{-3}, which is close to the experimental value [125, 28] of the *a*-Si density, 2.25–2.28 g.cm^{-3}, depending upon the method of preparation and experimental conditions. The modified Stillinger-Weber potential [126, 76] was used to calculate the total energy and forces and the velocity-Verlet algorithm was employed to integrate the equations of motion in canonical ensembles. The initial temperature was set at 1800 K and the system was equilibrated for 20 ps at 1800 K. The temperature was then gradually decreased, by using a chain of Nosé-Hoover thermostats [127, 128], from 1800 K to 300 K at an average cooling rate of 5×10^{12} K/s. The final structures from the MD simulations were further subjected to geometry optimization using the limited-memory BFGS algorithm, as described by [129]. Atomic configurations were collected during the course of simulations once the configurations satisfied a set of convergence properties, involving a minimum value of the width of the bond-angle distribution and the number of 4-fold-coordinated atoms in the network.

The second set of models were produced by using the WWW method. Here, we employed the modified version of the algorithm, developed by Barkema and Mousseau [38]. The method essentially consists of the following steps: 1) Generate a random configuration and construct a neighbor list of atoms using an appropriate cutoff value, such that the network is tetravalent as far as the list is concerned; 2) Employ the WWW bond-switching algorithm [26, 38] to produce a new configuration and accept or reject the configuration upon local relaxation of the network via the Monte Carlo method. The bond-switching procedure largely maintains the tetravalent character of the atomic network during simulations, and local relaxations were performed by using the nearest-neighbor-based Keating potential [34]; 3) Relax the resulting configuration from step 2 at a regular but infrequent interval to include the structural information from beyond the first shell of neighbors, by using a generalization of Weber's adiabatic bond-charge model [130]. For a description of the method, see [38]. In this study, we have employed three independent 21,952-atom WWW models for obtaining configurationally averaged values of structural properties.

In addition to the WWW and MD models of *a*-Si, we have also generated a set of disordered networks, M1–M3, of Si atoms. As stated earlier, these models are partially ordered and they can be classified by the degree of radial correlations present in the respective PCF. Specifically, M1 models are highly disordered and have very little or no radial correlations in the PCF. By contrast, M2 models are characterized by the presence of a well-defined first peak and radial correlations up to 3 Å. Likewise, M3 models exhibit radial correlations up to 6 Å with a pristine first peak and a part of the second peak, with a well-defined gap between the peaks. The M2 and M3 models were generated by adding one atom at a time in the simulation cell so that the addition of each atom satisfied a set of geometric constraints in order to produce radial correlations up to a length of 4 Å and 6 Å, respectively. The sizes of the WWW and M1/M2/M3 models were chosen to be 21,952 atoms, with a cubic supercell of linear size 77.03 Å.

Apart from the WWW, MD, and M1 to M3 models, we have also employed a number of disordered amorphous silicon (*da*-Si) and disordered crystalline silicon (*dc*-Si) configurations in this study. These configurations were produced by including structural disorder in pristine *a*-Si and diamond *c*-Si structures via random displacements of atoms, using $r_{i,\alpha} \rightarrow r_{i,\alpha} + \sigma\, p_{i,\alpha}$, from their original positions. Here, $r_{i,\alpha}$ is the α-th component ($\alpha = x/y/z$) of the atomic position at site i, σ is the maximum value of the atomic displacement in Å, and $p_{i,\alpha}$ is a random number, which is uniformly distributed between -1 and +1. The values of σ were chosen from 0.2 Å to 1.2 Å, which correspond to a distortion of the Si–Si bond length by 8–51% from its average/ideal value of 2.36 Å in *a*-Si/*c*-Si. It may be noted that a value of σ of the order of 0.3 Å satisfies the Lindemann's criterion of melting,

producing liquid-like structures of a-Si and c-Si. Thus, the dc-Si configurations with $\sigma \gg 0.3$ Å are considerably disordered compared to their counterparts with $\sigma \leq 0.3$ Å.

Given a distribution of atoms in a disordered network, the structure factor can be obtained from the Fourier transform of the reduced PCF, $G(r)$. Assuming that the distribution of atoms in the network is homogeneous and isotropic, the structure factor, $S(Q)$, is given by,

$$\begin{aligned} S(Q) &= 1 + \frac{4\pi n_0}{Q} \int_0^\infty r[g(r)-1]\sin(Qr)\,dr \\ &\approx 1 + \frac{1}{Q} \int_0^{R_c} G(r)\sin(Qr)\,dr, \end{aligned} \tag{3.1}$$

where $g(r)$ is the conventional pair-correlation function (PCF), $G(r) = 4\pi n_0 r\,[g(r)-1]$ is known as the reduced PCF, and n_0 is the average number density of the system. For finite-size models, the upper limit of the integral can be replaced by $R_c = L/2$ by using the periodic boundary conditions, provided $g(r) \to 1$ as $r \to R_c$. We shall see later that this condition is amply satisfied by models for which R_c is of the order of 20 Å.

3.3 Results and Discussion

3.3.1 Extended-range oscillations in the PCF of a-Si

We begin by establishing the unambiguous presence of radial oscillations in the PCF of a-Si at a distance of 20–40 Å. Since the calculation of the PCF beyond 20 Å requires sufficiently large models of a-Si, we first examine the large MD models, consisting of 400,000 atoms. Thereafter, we proceed to determine the origin of these oscillations by analyzing the three-dimensional network structure of these 400,000-atom models and a set of 21,952-atom models obtained from the WWW method. The results from these models will be compared with the same from the partially-ordered networks, M1 to M3, having varying degrees of radial ordering up to a distance of 6 Å. The PCFs of the partially-ordered networks, from M1 to M3, are shown in Fig. 3.1, along with the results from the 21,952-atom WWW models of a-Si. It is evident from the plots that the M2 and M3 models show radial correlations of up to 4 Å and 6 Å, respectively. The M1 models, on the other hand, exhibit small radial correlations up to 3 Å, which mostly originate from the imposed constraint of a minimum separation distance of 2 Å between any two atoms in the network.

Figure 3.2 shows the reduced PCF obtained from the MD models of a-Si, which consist of 400,000 atoms. The data presented here correspond to the configurational-averaged values of $G(r)$ from three independent configurations. The inset in Fig. 3.2 shows the presence of distinct radial oscillations at a distance beyond 20 Å, extending at least up to 40 Å. Similar oscillations have been also observed in the reduced PCF of 21,952-atom

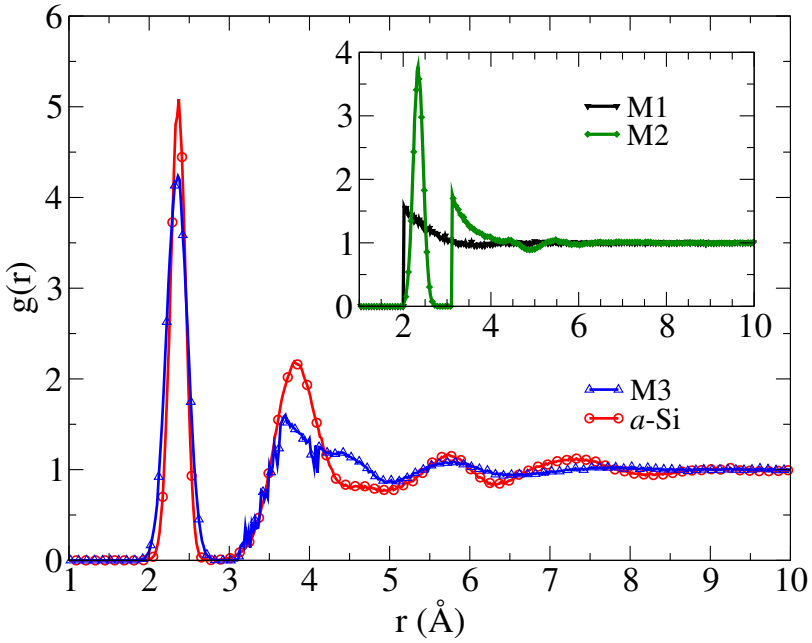

Figure 3.1: The pair-correlation functions of three partially-ordered models (M1 to M3) of Si atoms, showing radial correlations up to a length of 6 Å. The results for *a*-Si (WWW models) are shown for comparison with that for the M3 model. The size of the models corresponds to 21,952 atoms and the PCF data were averaged over three independent configurations for each model.

WWW models, but in a somewhat weaker form. This is apparent in Fig. 3.3, where we have plotted the configurationally averaged reduced PCFs for the 400,000-atom MD models and 21,952-atom WWW models. For comparison, the radial distances (r) in Fig. 3.3 are scaled by the corresponding position of the first peak (r_0) by introducing a scaled variable $R = r/r_0$. The inset in Fig. 3.3 clearly shows the presence of considerable oscillations in larger 400,000-atom MD models compared to their WWW counterpart in the region of R from 6 to 14, which translates into a distance of 14 Å to 33 Å for $r_0 \approx 2.37$ Å. The observed differences can be partly attributed to the size and statistics and in part to the nature of simulations. In general, MD models are considered to be more representative of annealed samples of *a*-Si, which are slighly more ordered than their as-deposited counterpart.

Table 3.1 presents some characteristic structural properties of the MD and WWW models. Since the presence of too many structural defects can affect the local density of the networks, and the radial correlations between atoms, it is necessary for the models to exhibit properties that are compliant with experimental observations. The presence of only a few dangling bonds (up to 1.3%) and floating bonds (up to 1.2%), as well as a small value of the root-mean-square width, $\Delta\theta$, about 9–10°, of the bond-angle distribution, confirms that the structural properties of these models are indeed consistent with actual samples of *a*-Si.

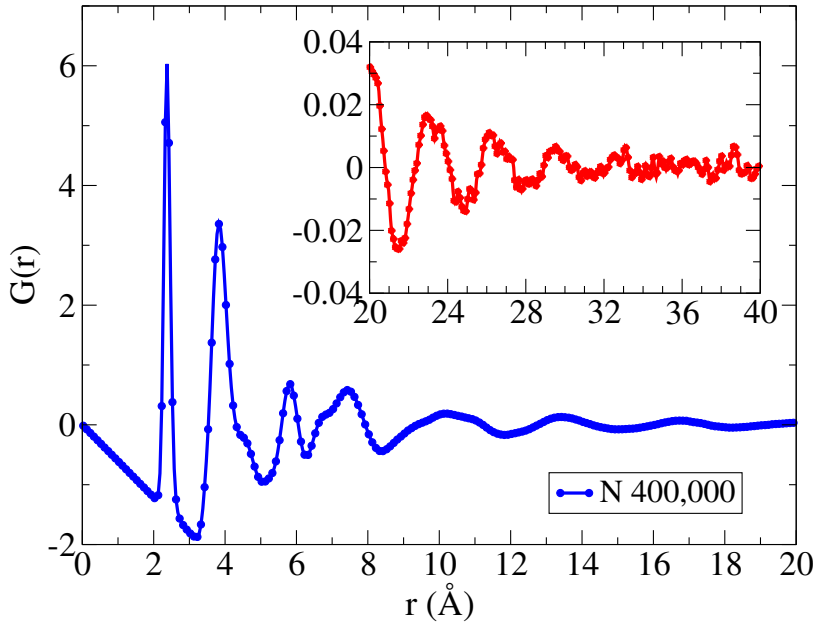

Figure 3.2: The reduced pair-correlation function, $G(r)$, of a-Si, obtained from a configurational averaging of three large MD models of size 400,000 atoms. The inset shows the presence of radial oscillations up to 40 Å, which are known as the extended-range oscillations in a-Si.

Table 3.1: Structural properties of three WWW models (W1–W3) and three MD models (MD1–MD3). The average bond length ($\langle r \rangle$), average bond angle ($\langle \theta \rangle$), and the root-mean-square width of bond angles ($\Delta\theta$) are expressed in Å and degree, respectively. C_n indicates the number of n-fold-coordinated atoms (in percent).

Model		Bond angle		Atomic coordination				Bond length
Type	Size (N)	$\langle \theta \rangle$	$\Delta\theta$	C_2	C_3	C_4	C_5	$\langle r \rangle$
W1	21,952	109.21	10.04	0.00	0.00	99.86	0.14	2.36
W2	21,952	109.23	9.83	0.00	0.00	99.9	0.1	2.36
W3	21,952	109.22	9.87	0.00	0.00	99.88	0.12	2.36
MD1	400,000	109.23	9.26	0.02	1.28	97.59	1.11	2.38
MD2	400,000	109.23	9.31	0.03	1.29	97.52	1.16	2.38
MD3	400,000	109.23	9.34	0.02	1.26	97.57	1.15	2.38

To further characterize the models, one often computes the electronic density of states (EDOS). The EDOS in a-Si is found to be very sensitive to the presence of coordination defects, especially three-fold-coordinated Si atoms or dangling bonds. The presence of an electronic gap largely depends on these defects, and the size of the gap is known to be related to the density of such defects and the degree of disorder in bond-length and bond-angle distributions. We have therefore calculated the EDOS of 21,952-atom WWW models and

400,000-atom MD models. Since the diagonalization of the Hamiltonian matrix (H) of such large a-Si models is highly nontrivial, we had to resort to: a) the tight-binding approximation of the Hamiltonian; and b) employ the recursion method of Haydock, Heine, and Kelly (HHK) [131, 132] to obtain the EDOS. In the recursion approach of HHK, one calculates the projected density of states $n_\alpha(E)$, associated with a basis function $|\alpha\rangle$ (involving a site and an orbital), by writing

$$n_\alpha(E) = \sum_k |\langle\alpha|\psi_k\rangle|^2 \delta(E - E_k). \tag{3.2}$$

Here, E_k and ψ_k are the energy eigenvalues and eigenvectors of H, respectively. Using a representation of the δ-function and writing $z = E + \imath\varepsilon$, where $\varepsilon \to 0^+$, it can be shown that the projected EDOS can be expressed in terms of the singular part of the diagonal element of the resolvent of H or the Green's operator $\hat{G}(z) = (z\hat{I} - \hat{H})^{-1}$. This yields [133]

$$n_\alpha(E) = -\frac{1}{\pi} \lim_{\varepsilon \to 0^+} \Im\, G_{\alpha\alpha}(E + \imath\varepsilon). \tag{3.3}$$

The local EDOS obtained from using Eq. (3.3) is averaged over multiple sites to calculate the total EDOS. For 400,000-atom MD models, the problem is particularly difficult due to the handling and storage of large matrices and the computational cost associated with the calculation for all sites. In practice, a few clusters of several hundred atoms are found to suffice for configurational averaging. Using a fast matrix-vector multiplication scheme and a compressed representation of the sparse H matrix, one can implement an order-N algorithm for the calculation of the local EDOS in the tight-binding approximation. The results obtained from these calculations are shown in Fig. 3.4. The presence of a clean gap, rather than a pseudo gap, in the EDOS further establishes the quality of the models. The approach can be adapted to calculate the vibrational density of states in the harmonic approximation, provided that an efficient scheme to obtain electronic forces for the construction of the dynamical matrix (DM) of a-Si is available. A simple order-N approach to construct the DM can be found in Ref. [134].

3.3.2 Origin of extended-range oscillations in a-Si

The first step toward understanding the ERO in a-Si follows from an analysis of the reduced PCF of disordered crystalline silicon (dc-Si) structures. The inclusion of positional disorder washes out the sharp δ-functions in the PCF of diamond c-Si and leads to a series of broadened peaks for the resulting dc-Si structures. A comparison of the reduced PCF of a-Si with those from dc-Si, for σ = 1.0 Å and 1.2 Å, in Fig. 3.5 reveals that a-Si exhibits small but noticeable oscillations at large distances of up to at least 30 Å. Despite the fine

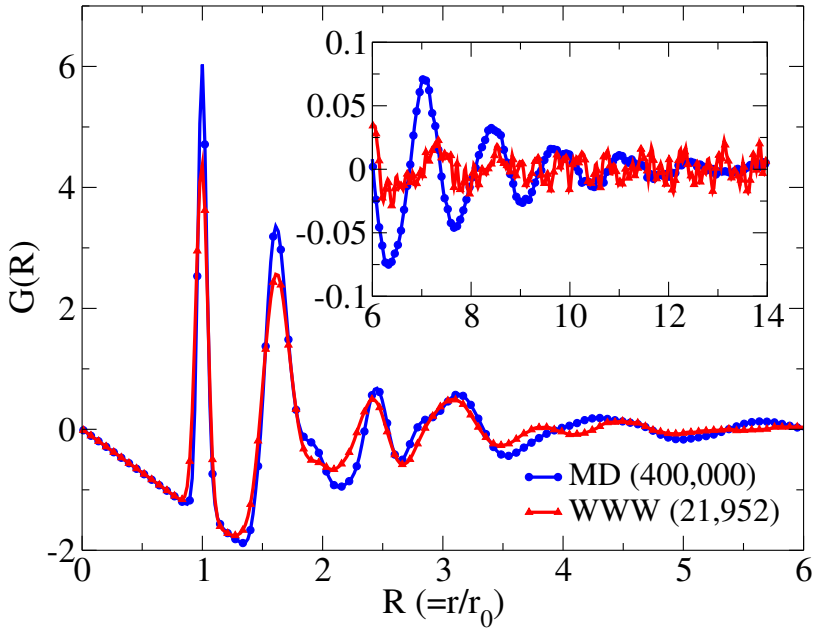

Figure 3.3: The reduced PCFs of the 400,000-atom MD models and 21,952-atom WWW models showing the presence of considerable extended-range oscillations in larger MD models. For clarity, the radial distances are scaled by the corresponding first peak of the PCF, i.e., $R = r/r_0$, where r_0=2.37 Å.

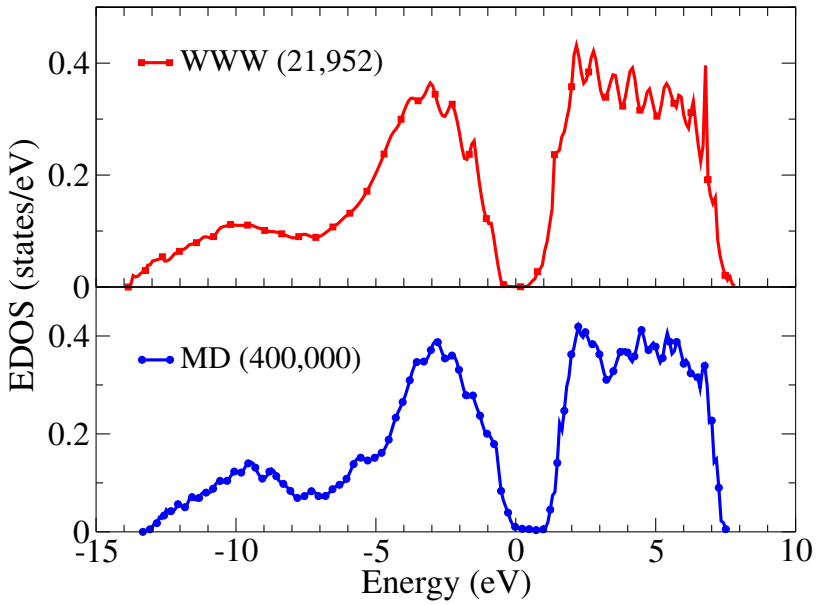

Figure 3.4: The electronic density of states (EDOS) of 21,952-atom WWW and 400,000-atom MD models obtained from the tight-binding approximation. The presence of an electronic band gap is clearly visible in the plots.

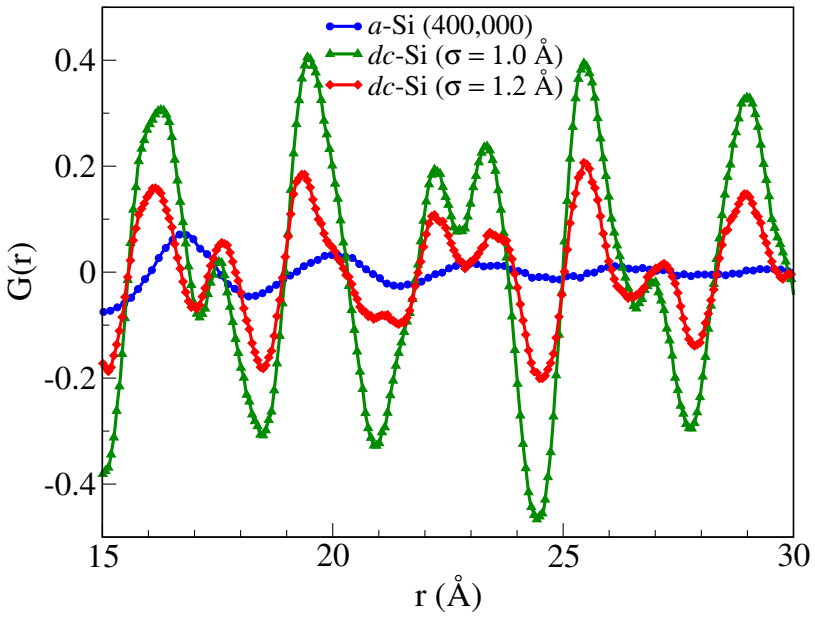

Figure 3.5: The presence of radial oscillations in MD models of *a*-Si (blue) of size 400,000 atoms and two *dc*-Si structures of size 405,224 atoms from 15 Å to 30 Å. The positions of the radial peaks of *a*-Si approximately correspond to those of *dc*-Si, indicating the possible presence of weak extended-range ordering in *a*-Si beyond 15 Å.

structure of $G(r)$ in *dc*-Si, it is apparent that the positions of the peaks in *a*-Si approximately coincide with those in *dc*-Si. This observation leads to the possibility that the ERO in *a*-Si could originate from the presence of weak radial-shell structures on the nanometer length scale, as in the case of *dc*-Si. This point is examined at length in the following paragraphs.

Assuming that radial-shell structures exist in the partially-ordered environment of *a*-Si at large distances, one may express the total PCF, $g(r)$, as a linear combination of the same for each coordination shell, $g_n(r)$. Thus, $g(r) = \sum_n g_n(r)$, where $g_n(r) = \langle g(r = |\mathbf{r_n} - \mathbf{R_i}|)\rangle_i$. Here, r is the distance between a central atom at $\mathbf{R}_i$ and its neighbors in the nth coordination shell at $\mathbf{r}_n$, and the symbol $\langle\,\rangle_i$ stands for the average over all atoms and independent configurations. Since, for an arbitrary (highly) disordered network, distant radial shells may not exist or be well defined – depending on the degree of radial disorder – it is more appropriate to define the nth coordination or topological shell as one that consists of nth near neighbors of the central atom at $\mathbf{R_i}$. This is schematically illustrated in Fig. 3.6 by showing the first-shell neighbors (green) and the second-shell neighbors (yellow) of the central atom (blue). The key point here is that the nth neighbors of a central atom are those that can be reached (from the center) by a minimum of n distinct and irreversible steps, irrespective of the presence of well-defined radial shells or not. Thus, the coordination shells defined above depend on the topology or connectivity of the atomic network, and

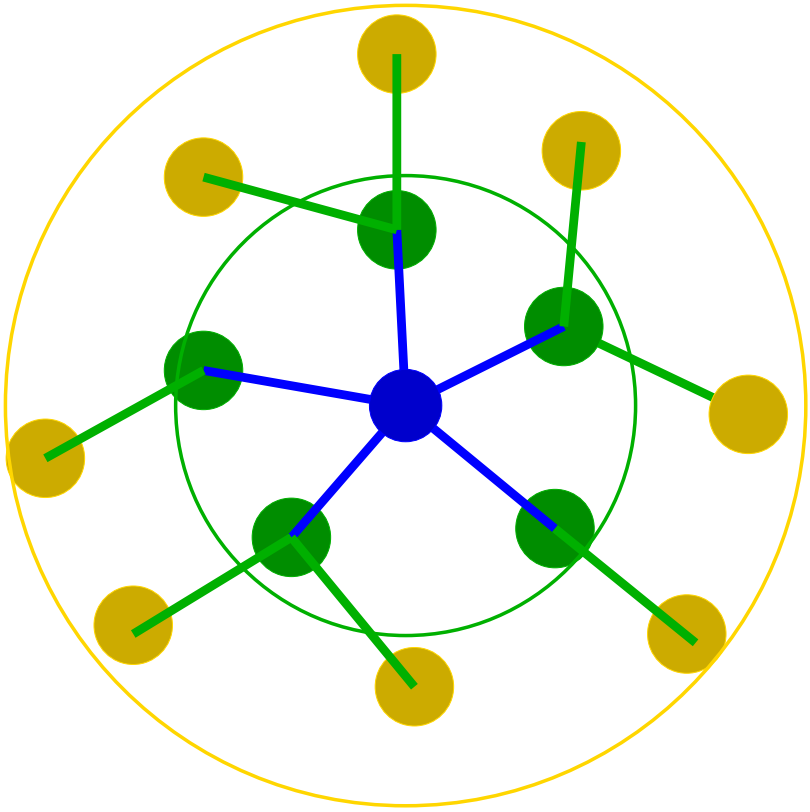

Figure 3.6: A schematic representation showing the first two coordination shells of a central atom (blue) in a two-dimensional disordered network. The atoms in the first shell (green) and the second shell (yellow) can be reached from the central atom in one step and two steps, respectively.

the three-dimensional shape of the shells may not be necessarily spherical. We shall see later that this can lead to a highly asymmetrical radial distribution of atoms within the coordination shells of partially-disordered networks. Figure 3.7 shows the shell PCFs, $g_n(r)$, obtained for the first six coordination shells, along with $g(r)$ for a 21,952-atom WWW model of *a*-Si. It is apparent that the shell PCFs, for $n = 1$ to $n = 6$, can be represented by a bell-shaped curve in *a*-Si, with the exception of $g_3(r)$ for which a bi-modal distribution is observed. The latter is consistent with the earlier study by Uhlherr and Elliott [100], who attributed the bi-modal shape of $g_3(r)$ to the end-to-end radial distances of a set of four neighboring atoms or quartets associated with dihedral angles in *a*-Si.

Having expressed the total PCF in terms of $g_n(r)$, we now examine the oscillations in the PCF by studying individual $g_n(r)$s, which reflect the characteristic properties of the radial distributions of atoms in *n*th shells. In particular, the width of $g_n(r)$ is indicative of the strength of the radial (dis)order in the *n*th shell. A small value of the width corresponds to a highly ordered state of atoms within the shell as far as radial ordering is concerned, and vice

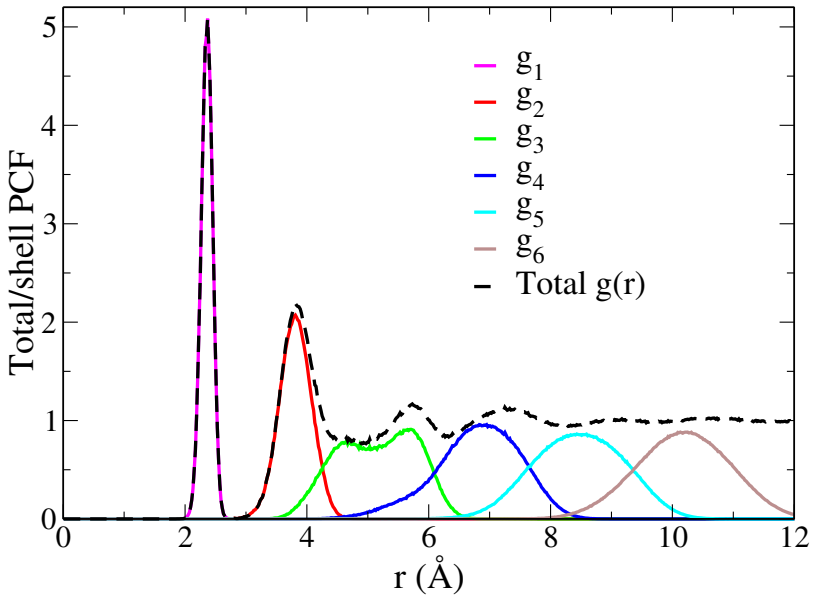

Figure 3.7: The shell pair-correlation function, $g_n(r)$, for the nth coordination shell of a 21,952-atom WWW model of a-Si. The total $g(r)$ (dashed black), which is given by the sum of all shell PCFs, is also shown in the plot.

versa. This assertion can be verified by computing $g_n(r)$ for a number of partially-ordered networks of silicon. Figure 3.8 shows the results for the 13th coordination shell, $g_{13}(r)$ as a representative example, obtained from 21,952-atom models, of a-Si, dc-Si, and M2. As stated earlier in Sect. 3.2, the latter model (M2) is characterized by the presence of a well-defined first-coordination shell, whereas the dc-Si structures are produced by using a value of σ in the range from 0.3 Å to 1.0 Å. It is apparent that a small value of σ (for example, σ = 0.3 Å) produces well-defined multiple peaks in $g_{13}(r)$ for dc-Si models. However, as the value of σ increases and goes beyond 0.6 Å, the peaks in $g_{13}(r)$ coalesce to form a unimodal distribution. This is unsurprising due to the presence of strong residual crystalline order in the dc-Si networks for $\sigma \leq 0.6$ Å. By contrast, the width of $g_{13}(r)$ for a-Si is found to be considerably smaller than its M2 counterpart, which shows a more radially disordered distribution of atoms within the same shell in M2. This observation is found to be true not only for $g_{13}(r)$ but also for all $g_n(r)$s. The high asymmetry of $g_{13}(r)$ for the M2 and dc-Si models can be readily attributed to the connectivity of the atoms in these models. Since the position of an atom in a given coordination shell is determined by the number of steps/hops from the central atom, there exist a few atoms in the shell that are radially close to the central atom but are not reachable (from the central atom) via a small number of steps/hops, due to the low connectivity of the atoms in the networks for increasing values of σ. This is reflected in the left tail of the distribution (see Fig. 3.8), which leads

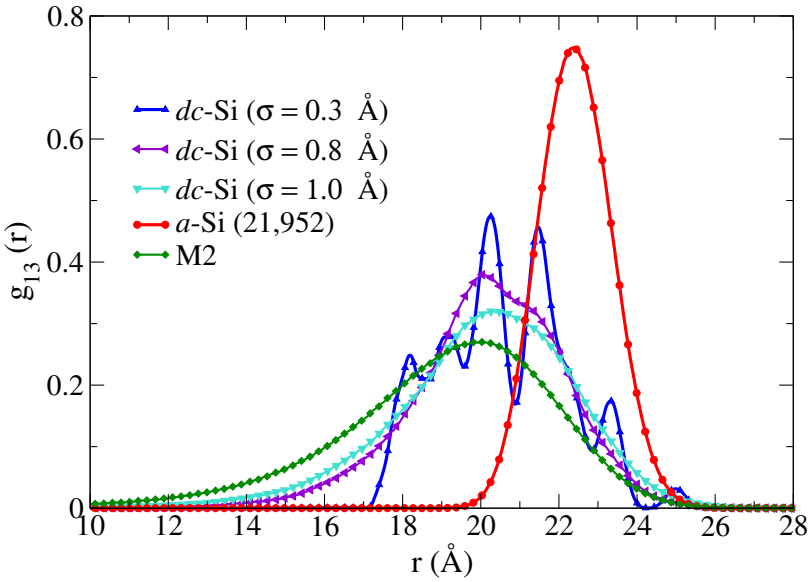

Figure 3.8: The shell pair-correlation functions, $g_{13}(r)$, obtained from 21,952-atom WWW models of *a*-Si (red), *dc*-Si (blue/purple/cyan), and partially-ordered configurations M2 (green) of Si atoms. The disordered crystalline structures were generated from the diamond *c*-Si structure, using σ = 0.3, 0.8, and 1.0 Å.

to a negative value of the skewness for the radial distribution of atoms in the shell. This can be verified by computing the Fisher-Pearson (FP) coefficient of skewness [135], s, for $g_{13}(r)$, for different σ values. In general, the FP coefficient of skewness is given by the standardized third central moment of a distribution, and a negative value of the coefficient signifies a skewed distribution toward the left, and vice versa. The variation of s with σ for a number of *dc*-Si models is shown in Fig. 3.9, along with the corresponding value of the coefficient for the M2 model for comparison.

Figure 3.10 shows the full width at half maximum (FWHM) of the shell PCFs, $g_n(r)$, for different shells, from n=1 to n=20, for a class of partially-ordered models (M1 to M3), *a*-Si, and *dc*-Si models of size 21,952 atoms. Since *dc*-Si models tend to exhibit the presence of multiple peaks in $g_n(r)$ for $\sigma \leq 0.6$ Å, the FWHM for the *dc*-Si models (with multiple peaks) in Fig. 3.10 is calculated by fitting each individual peak with a Gaussian distribution and averaging over the resulting FWHM values for all major peaks in the distribution. The FWHM values (in Fig. 3.10) suggest that the M1 models are highly disordered, whereas the *dc*-Si structures with σ = 0.2 Å are the least disordered configurations. This observation is indeed true by construction. For σ = 0.2–0.5 Å, a significant radial ordering exists in the *dc*-Si structures that leads to a small value of the width in Fig. 3.10. The rest of the models, from M2 and M3 to *a*-Si, exhibit an increasingly more ordered state of radially distributed

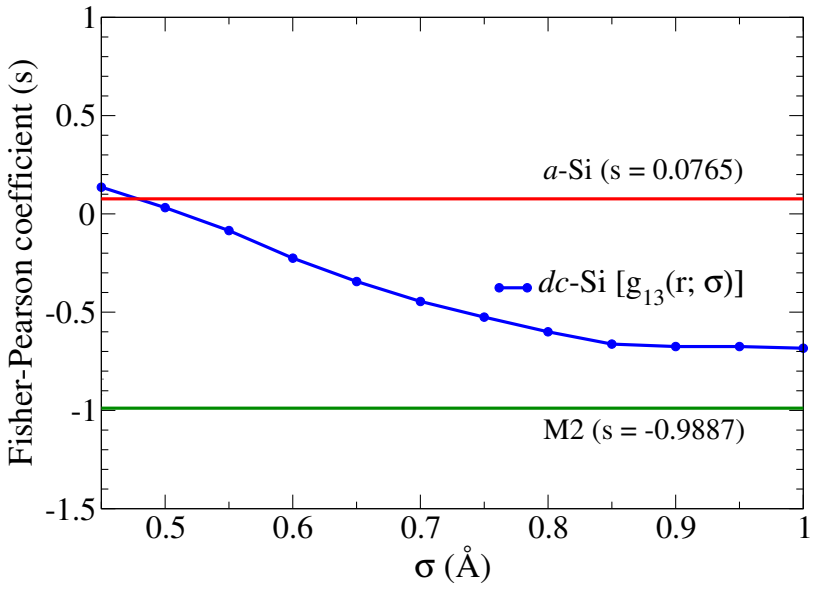

Figure 3.9: The variation of the Fisher-Pearson coefficient of skewness, s, for the distribution $g_{13}(r;\sigma)$ with σ for a number of *dc*-Si models (blue). The coefficients for the M2 model (green) and *a*-Si (red), for $\sigma = 0$, are shown in the plot for comparison.

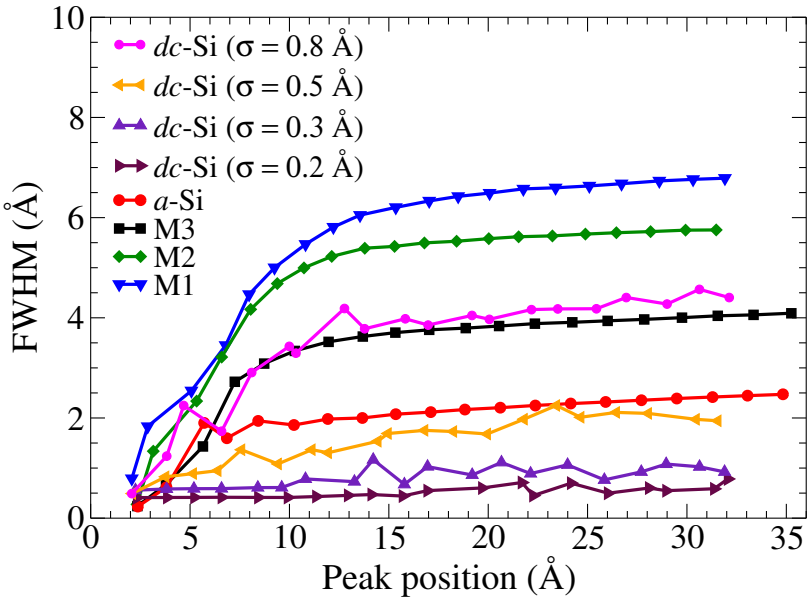

Figure 3.10: The full width at half maximum (FWHM) for a set of partially-ordered configurations (M1 to M3), *a*-Si, and four *dc*-Si structures of size 21,952 atoms. The *dc*-Si structure (with $\sigma = 0.2$ Å) is the most ordered configuration, whereas M1 is the least ordered configuration, by construction.

atoms in the shells. It is apparent that as more radial ordering is incorporated in a model (for example, M2 and M3), the corresponding FWHM value of $g_n(r)$ begins to decrease

for a given shell. Conversely, the inclusion of (additional) structural disorder increases the corresponding FWHM value of $g_n(r)$ in a model. This can be seen from Fig. 3.11, where the addition of positional disorder, via random displacements of atoms in M1, M3, and *a*-Si, resulted in an increase of the FWHM values of $g_n(r)$. This observation also applies to the total PCF of *a*-Si. Figure 3.12 shows that the amplitude of the radial oscillations reduces in the region of 20–40 Å with the addition of positional disorder in *a*-Si. It may be noted that the FWHM values for the M1 models, which are highly disordered by construction, are practically unaffected in Fig. 3.11 in the presence of additional disorder with σ values of the order of 0.3 Å. Thus, the width (or the average width for a multimodal case) of $g_n(r)$ can be taken as a measure of the radial order/disorder in partially-ordered networks, including *a*-Si and *dc*-Si structures.

3.3.3 Shannon information as a measure of extended-range ordering

The assertion that the width of the shell pair-correlation function, $g_n(r)$, can provide a measure of the disorder in the radial distribution of atoms in the n-th coordination shell of a disordered network is not particularly surprising and it directly follows from the Shannon measure of information (SMI) [136]. By normalizing the shell PCF, $g_n(r)$, one can readily construct a discrete probability measure, p_n^i, to define the SMI as follows:

$$S[p_n^i] = -k \sum_i p_n^i \ln p_n^i. \tag{3.4}$$

In Eq.(3.4), the value of $0\ln(0)$ is defined to be 0, k is a constant, and p_n^i is given by

$$p_n^i = \frac{g_n(r_i)}{\sum_i g_n(r_i)}.$$

The SMI can be understood as providing a measure of the degree of uncertainty or the lack of radial ordering in the distribution of atoms in the coordination shells. The multiplicative constant k in Eq. (3.4) can be taken as unity without any loss of generality. The results for the SMI obtained from M1/M2/M3/*a*-Si models are shown in Fig. 3.13 for the first twenty coordination shells. The corresponding results for diamond *c*-Si are also shown in the plot for comparison. As one may expect, the SMI values for different shells behave in a similar manner as that of the FWHM (of the shell PCFs) with respect to the peak position in Fig. 3.10. Once again, the largest values of the SMI correspond to the highly disordered M1 models, whereas *a*-Si exhibits the smallest values of the SMI for each shell among M1, M2, M3 and *a*-Si. It is noteworthy that, unlike the case of disordered and amorphous Si networks, the SMI values associated with the coordination shells in the diamond *c*-Si structure, which is perfectly ordered, increase considerably with the increasing shell number in a global sense.

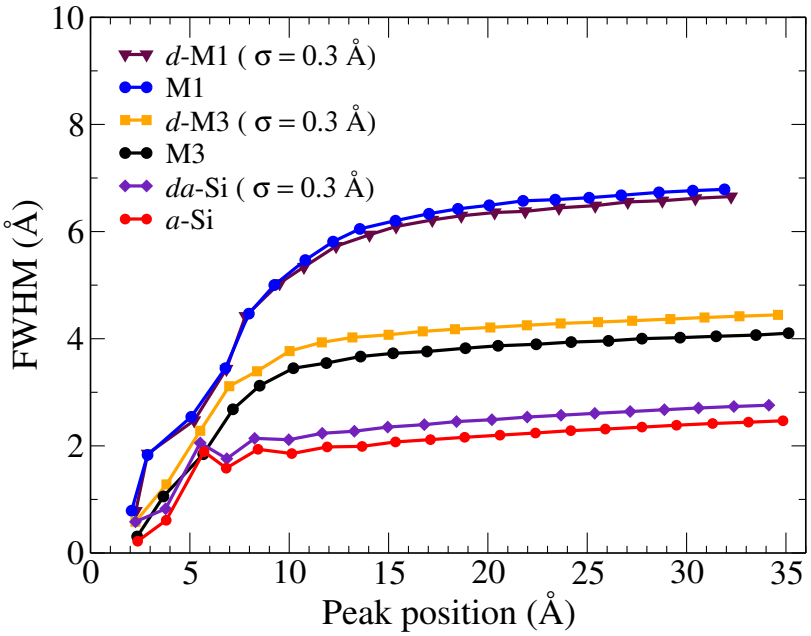

Figure 3.11: The effect of the addition of positional disorder on the FWHM of the shell PCFs in M1, M3, and *a*-Si. The FWHM values of the unperturbed models are also shown for comparison.

This observation can be attributed to the presence of multiple peaks in the higher-order coordination shells. Since the (shell) PCFs for a crystalline structure consist of a series of δ-functions, the presence of an increasing number of peaks in the distant shells leads to more uncertainty in the radial distribution of the atoms in these shells. This is reflected in the larger value of the SMI for the distant shells. Thus, the SMI can be loosely interpreted as a global measure of ordering/disordering in the distribution, which is most appropriate for describing the degree of order/disorder associated with unimodal distributions. However, for multimodal distributions, such as the *dc*-Si structures with $\sigma \leq 0.5$ Å, one requires a suitable local measure of information, for example, the Fisher information [137], in order to quantify the degree of disorder or uncertainty associated with the radial distribution of the atoms in the coordination shells. These issues will be addressed elsewhere from an information-theoretic point of view in a future communication.

The origin of the extended-range oscillations in *a*-Si can now be interpreted in light of the results from Figs. 3.7–3.13. Since the full PCF can be expressed in terms of its partial components, any structural aspects of $g(r)$, such as the extended-range oscillations, can also be represented by a suitable set of $g_n(r)$, associated with the length scale of the oscillations. Figures 3.10 and 3.13 essentially suggest that, as the degree of radial ordering in the full PCF increases from M1 to M3, the corresponding width and the Shannon information associated

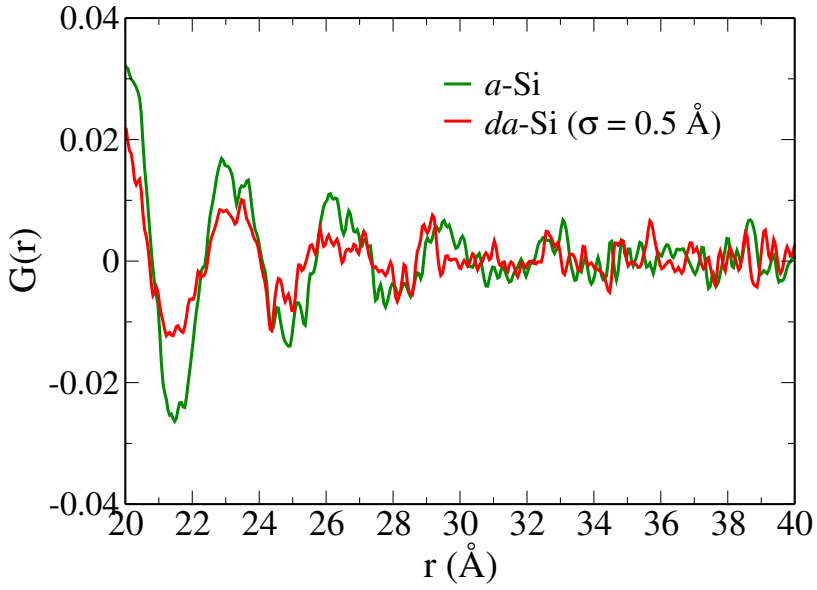

Figure 3.12: The effect of the addition of positional disorder, with $\sigma = 0.5$ Å, on the radial oscillations in a 400,000-atom MD model of *a*-Si between 20 Å and 40 Å. The results for the corresponding pristine *a*-Si model (green) are also shown for comparison.

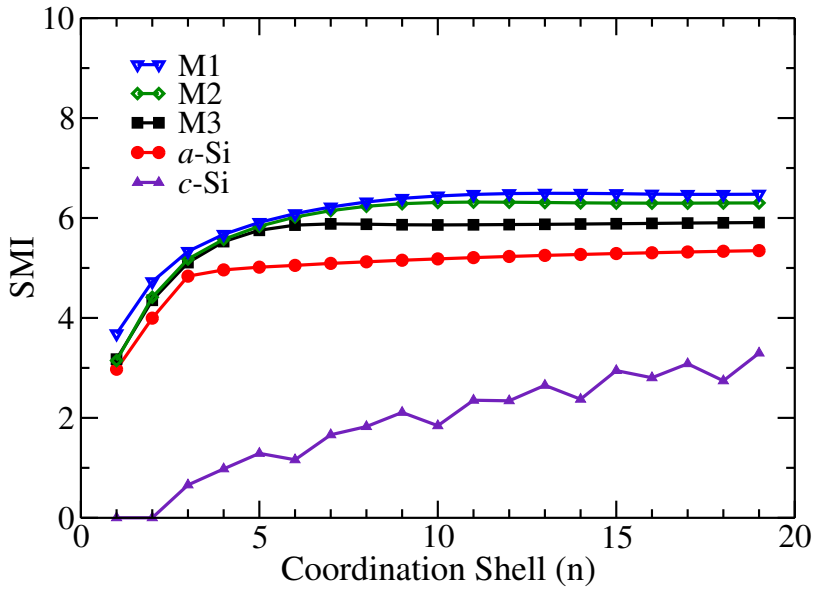

Figure 3.13: The Shannon measure of information (SMI), associated with a discrete probability measure p_n, obtained from the shell pair-correlation functions, $g_n(r)$, for M1 to M3, *a*-Si, and diamond *c*-Si. For disordered and amorphous Si networks, the results were averaged over three independent configurations for each shell.

with $g_n(r)$ steadily decrease. Thus, the inclusion of radial information of up to a distance of 4 Å in M2 and about 6 Å in M3 suffices to result in a reduction of the width of $g_n(r)$

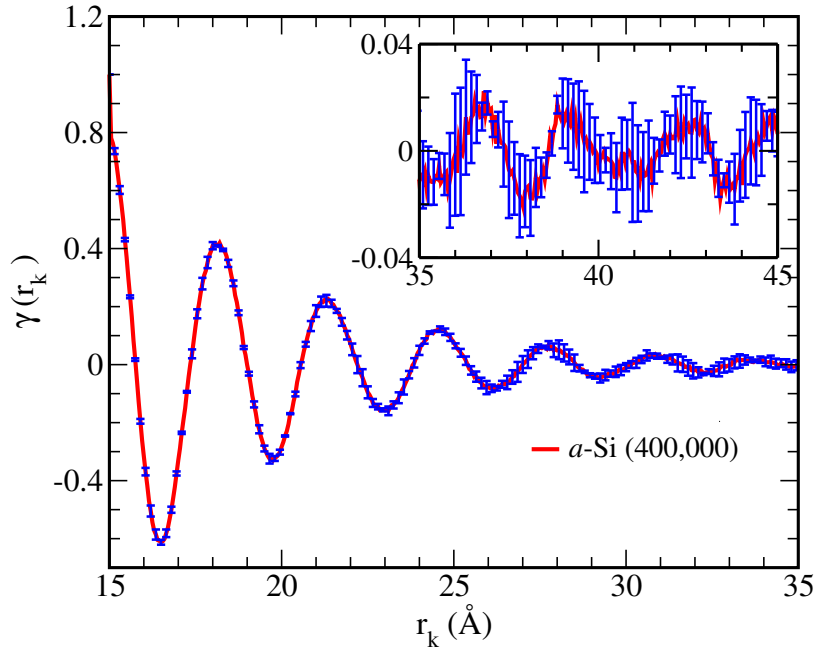

Figure 3.14: The autocorrelation coefficient, $\gamma(r_k)$, of a set of $G(r)$ values from r = 15 Å to r = 45 Å, constructed from 400,000-atom MD models of *a*-Si, showing the presence of radial correlations up to 45 Å. The root-mean-square fluctuations are shown as error bars (blue vertical lines). For visual clarity, the results for the radial region from 35 Å to 45 Å are shown in the inset.

associated with the distant coordination shells. Since *a*-Si is characterized by the presence of strong radial ordering at least up to a length of 20 Å in the full PCF, it is unsurprising that a small value of the width of $g_n(r)$ of *a*-Si is reflective of the radial ordering in the distant shells on the length scale of 20–40 Å. By contrast, the *dc*-Si models with σ = 0.2–0.5 Å show significant radial ordering as far as the widths of various $g_n(r)$s are concerned. Thus, the ERO in *a*-Si can be understood as the resultant density fluctuations, originating from highly ordered radial distributions of atoms in the first few coordination/radial shells, which propagate and decay radially as the (density) fluctuations travel through the distant shells. A comparison of the results from the M2, M3, and *a*-Si models in Fig. 3.10 appears to suggest that the characteristic local radial ordering of up to 6 Å forces the atoms in distant shells to organize in such a way that small radial oscillations are built up on the length scale of up to 40 Å, when the model is sufficiently large. The presence of these small but distinct radial oscillations in the full PCF is indicative of the existence of weak extended-range radial ordering in *a*-Si up to a length of 40 Å, as far as the size of the *a*-Si models studied in this work are concerned.

3.3.4 Decay of radial correlations, autocorrelation coefficient, and comparison with experimental diffraction data

The presence of radial atomic correlations beyond 20 Å can be further evidenced by computing the autocorrelation coefficient(s) of $G(r)$. Assuming that M observations, $y_1, y_2, \ldots, y_M$, form a time series, where $y_i = G(r_i)$, the autocovariance coefficient [138], c_k, between the observations that are k-steps apart, is given by:

$$c_k = \frac{1}{M} \sum_{i=1}^{M-k} (y_i - \bar{y})(y_{i+k} - \bar{y}),\ k = 1, ..., n, n < M. \tag{3.5}$$

The autocorrelation coefficient at lag k is then expressed as $\gamma_k = c_k/c_0$, where c_0 is the variance and $\bar{y}$ is the mean value of the set $\{y_i\}$. Figure 3.14 shows a plot of γ_k versus r_k. Here, the set $\{y_i\}$ is constructed by choosing a segment of $G(r)$ from r_1 = 15 Å to r_n = 45 Å and expressing k in terms of $r_k = r_1 + k\Delta r$, where Δr is the distance between two consecutive observations of $G(r)$. It is apparent from the plot that, given the set of $G(r)$ values from 15 Å to 45 Å, Δr = 0.05 Å, n = 600, and M = 900, the radial correlations decay in an oscillatory manner and become almost negligible after 35 Å. The root-mean-square (RMS) fluctuations of γ_k, obtained from the configurational averaging of the results from three independent MD models of size 400,000 atoms, are also shown in Fig. 3.14. Since the RMS values of the fluctuations are almost of the order of γ_k for $r \geq 40$ Å, the radial correlations in this region may not be significant, even though the presence of small residual correlations can be seen in this region.

We now provide a direct comparison of our results with those from diffraction measurements by computing the decay length and the (spatial) period of the ERO at radial distances beyond 10 Å. High-energy x-ray diffraction measurements on *a*-Si samples, by Roorda et al. [124], suggest that the period of oscillations ranges from 2.77 Å to 3.03 Å and that the decay length in annealed samples of *a*-Si is about 4.23 Å. Figure 3.15 shows the decay of the amplitudes of radial oscillations in $G(r)$ for 400,000-atom MD models of *a*-Si, which can be roughly considered as the simulated counterpart of annealed samples of *a*-Si in experiments. Here, the amplitudes and positions of the peaks are obtained from Fig. 3.2. The corresponding decay for *dc*-Si networks for σ = 0.7 Å and 0.8 Å are also included in the plot for comparison. For visual clarity, the first three peaks of *a*-Si are omitted from the plot, by choosing an appropriate range for the y axis. The values of the period and the decay length obtained from our calculations compare very well with the results from experiments. The average period of oscillations from 400,000-atom MD models, in Fig. 3.15 (and Fig. 3.2), is found to be 3.2$\pm$0.065 Å, which is very close to the experimental value of 3.03 Å, and the corresponding decay length turns out to be about 4.81$\pm$0.012 Å. The

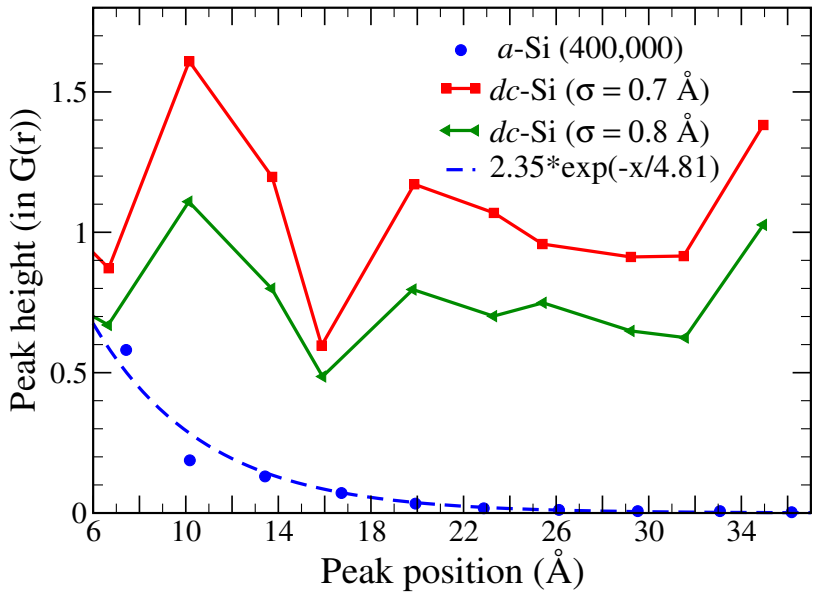

Figure 3.15: The decay of the radial peak heights in $G(r)$ for a-Si (blue) and dc-Si (red and green) with peak distances. The exponential fit of the peak positions (dashed blue line) corresponds to the data for a-Si models of size 400,000 atoms. The decay length for a-Si corresponds to a value of 4.81 Å. The corresponding peak positions for dc-Si structures are shown for comparison.

latter is somewhat higher than the experimental value of 4.23 Å, obtained from the Fourier transform of experimental diffraction data by [124]. It is evident from Fig. 3.15 that the dc-Si models exhibit a rather slow decay, even for considerably large values of σ from 0.7 Å to 0.8 Å.

3.3.5 Relation between ERO and the first sharp diffraction peak in a-Si

In this section, we address the question whether the presence of extended-range oscillations has any bearing on the position and intensity of the first sharp diffraction peak (FSDP) in a-Si. Since the origin of the FSDP is strongly related to the presence of medium-range order (MRO) in glasses, which can extend up to a radial distance of approximately 20 Å, it is instructive to examine whether the ERO in a-Si can produce any observable effect on the intensity of the FSDP near 2.0 Å^{-1}.

The effect of distant radial correlations on the position and intensity of the FSDP in a-Si can be calculated from using Eq. (3.1). However, a direct application of Eq. (3.1) to very large models can be problematic for two reasons. First, the presence of noise in $G(r)$ at large R can introduce errors, depending on the signal-to-noise ratio in $G(r)$. This makes it difficult to identify the optimal value of R_c for large models, by varying the upper limit of

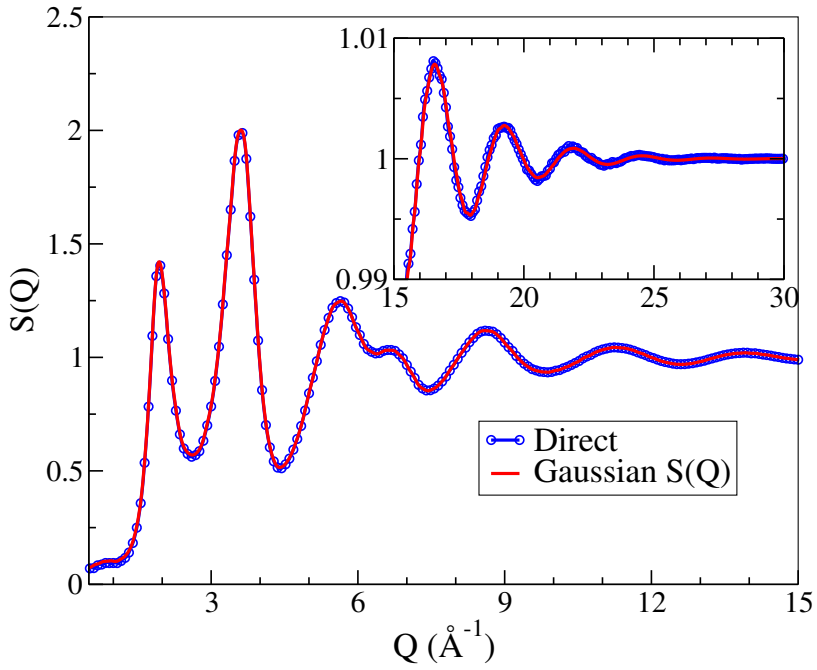

Figure 3.16: The static structure factor, $S(Q)$, of a 21,952-atom WWW model of a-Si obtained from the Gaussian approximation (red line) and from direct numerical calculations (blue circles) using Eq. (3.7).

the integral in Eq. (3.1). Second, for large values of R, the integrand can be highly oscillatory and conventional integration techniques may not suffice to accurately compute $S(Q_0)$ in the presence of a noisy $G(r)$. To ameliorate these issues, we shall address the problem by expressing $G(r)$ in terms of suitable distance-dependent radial basis functions, and calculate the resulting integral analytically to obtain a closed expression for $S(Q)$. Noting that the oscillations are particularly pronounced in $G(r)$, it is useful to write $G(r)$ as a linear combination of Gaussian functions

$$G(r) = \sum_{i=1}^{m} a_i e^{-b_i(r-c_i)^2} \tag{3.6}$$

in an effort to obtain an analytical expression for $S(Q)$ in terms of the Gaussian parameters. The parameters a_i, b_i, and c_i determine the approximate peak/trough height, width, and the (radial) position of the i^{th} peak/trough, respectively, and can be obtained either via a nonlinear fit of Eq. (3.6) to experimental/simulated reduced PCF data, $G(r)$, or by minimizing a suitable cost function with respect to the set of parameters (a_i, b_i, c_i). Here, we have taken the second approach and ensured that $b_i > 0$ for all i. The structure factor can be expressed in terms of

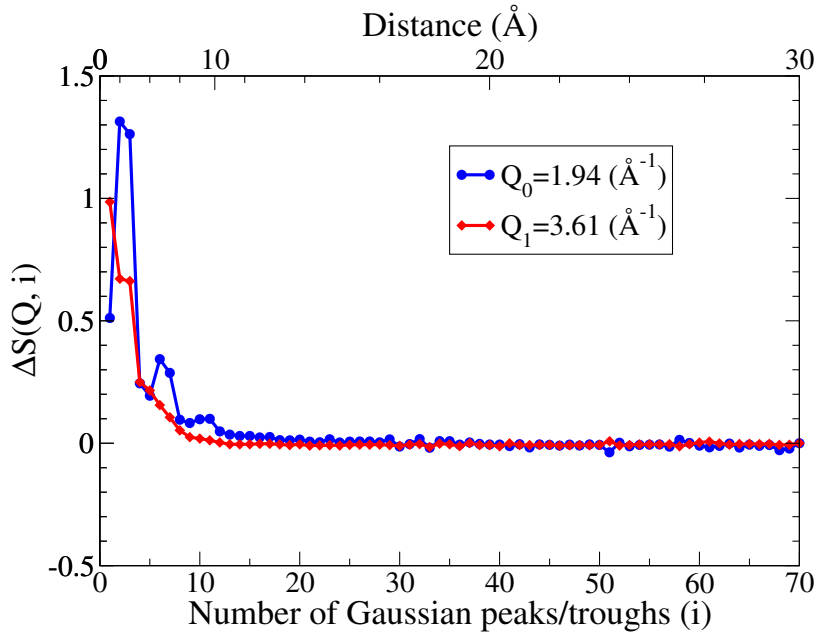

Figure 3.17: The convergence of the intensity of the FSDP (at Q_0) and the principal peak (at Q_1), obtained from Eq. (3.7), with respect to the number (i) of Gaussian peaks/troughs for a 21,952-atom WWW model. The radial length associated with the Gaussian peaks/troughs is indicated in Å on the secondary x axis (top).

the fitted Gaussian parameters:

$$S(Q) = 1 + \int_0^{R_c} rG(r)\,\frac{\sin(Qr)}{Qr}\,dr \tag{3.7}$$

$$= 1 + \frac{1}{Q}\sum_{i=1}^{m} a_i \sqrt{\frac{\pi}{b_i}}\,\sin(Qc_i)\,\exp\left[-\frac{Q^2}{4b_i}\right] \tag{3.8}$$

In writing Eq. (3.8), we have denoted, for notational convenience, the set (a_i, b_i, c_i) as the fitted values of the parameters and assumed that the center of each Gaussian function, c_i, satisfies the condition $0 \ll c_i \ll R_c$ so that $S(Q)$ can be written as a sum of Gaussian integrals (and not error functions) with the integration limit extending from 0 to ∞. This condition is readily satisfied by choosing an appropriate value of m, such that $R_c \gg c_m$, and noting that the first peak of the PCF in a-Si rapidly decays to zero for $r \leq 2.0$ Å. In practical calculations, a value of R_c of the order of 20 Å is found to be sufficient for accurate determination of $S(Q)$ using Eq. (3.7) [see [69] and Fig. 3.17 here]. The structure factor obtained from Eq. (3.8) for a 21,952-atom WWW model of a-Si is plotted in Fig. 3.16, along with the results from direct numerical calculations from Eq. (3.7) for comparison. For clarity, the wavevector region from 15 Å^{-1} to 30 Å^{-1} is shown separately as an inset in Fig. 3.16.

The variation of the intensity of the FSDP and the principal peak (i.e., the peak at 3.6 Å^{-1}) can be studied, by using Eq. (3.8), with respect to the number of Gaussian basis functions m for a given R_c. Writing $\Delta S(Q,i) = S(Q,m) - S(Q,i)$, where m=70 for R_c = 30 Å, Fig. 3.17 shows the convergence of ΔS at Q_0 = 1.94 Å^{-1} and Q_1 = 3.6 Å^{-1} for an increasing number (i) of peaks/troughs. Here, Q_0 and Q_1 correspond to the position of the FSDP and the principal peak, respectively. It is apparent that both $S(Q_0,i)$ and $S(Q_1,i)$ converge to the respective limiting value, $S(Q,m)$, very rapidly as i approaches to 30, which corresponds to a radial length of about 18 Å, as indicated in Fig. 3.17. The length is indicated at the top of the plot as a secondary x axis, which reflects the non-uniform distribution of Gaussian peaks/troughs in the radial-region of 0–30 Å. Figure 3.17 suggests that radial correlations from the region beyond 20 Å do not really play any significant role. This observation can be stated more precisely. The magnitude of the contribution to $S(Q)$ obtained by including an additional peak/trough beyond m in Eq. (3.8) can be written as:

$$\begin{aligned} |\delta S(Q,m)| &= |S(Q,m+1) - S(Q,m)| \\ &= \left| \frac{1}{Q}\sqrt{\frac{\pi a_{m+1}^2}{b_{m+1}}}\, \sin(Qc_{m+1})\, \exp\left[-\frac{Q^2}{4b_{m+1}}\right] \right| \\ &\leq \frac{1}{Q}\sqrt{\frac{\pi a_{m+1}^2}{b_{m+1}}}\, \exp\left[-\frac{Q^2}{4b_{m+1}}\right]. \end{aligned} \tag{3.9}$$

Substituting $Q = Q_0$ = 2 Å^{-1} in Eq. (3.9) for the FSDP in a-Si, one obtains:

$$|\delta S(Q_0,m)| < \frac{a_{m+1}}{\sqrt{b_{m+1}}}\, \exp\left[-\frac{1}{b_{m+1}}\right] \tag{3.10}$$

The asymptotic behavior of $|\delta S(Q_0,m)|$ with respect to m follows from Eq. (3.10). Since $G(r) \to 0$ as $r \to R_c$ for very large models, the parameter a_m, which determines the height of the Gaussian peak, decreases with an increasing value of m, and $|\delta S(Q_0,m)|$ becomes increasingly smaller as m becomes a large number. In practice, however, $|\delta S(Q_0,m)|$ fluctuates between 0 and a small value ε due to the presence of numerical noise at large radial distances, which can be reduced by averaging $S(Q)$ [in Eq. (3.8)] over many independent sets of fitted Gaussian parameters. Further, a value of R_c of about 30 Å is found to be sufficient for the calculation of $S(Q)$ from Eqs. (3.7) and (3.8). The results from our calculations suggest that the average value [139] of ε is typically of the order of 0.025 for radial distances between 20 Å and 30 Å. This roughly translates into an error of 1.7%, assuming $S(Q_0)$=1.5 for as-deposited samples from experiments [101]. Thus, aside from small fluctuations of $S(Q_0)$ owing to numerical noise, the extended-range oscillations in the radial region of 20–30 Å do not seem to play any observable role in determining the intensity of the FSDP in

a-Si. A similar conclusion was reached in a recent study [69], where an alternative argument based on the analysis of the behavior of $rG(r)$ and the sampling of $\sin(Qr)/Qr$ within the radial region from 0 to R_c in Eq. (3.7) was provided by the authors of the study to support this conclusion.

3.4 Conclusions

The present study addresses the origin of the extended-range oscillations in *a*-Si from a real-space point of view. By analyzing a class of large partially-ordered networks of Si atoms with radial ordering up to a distance of 6 Å in the PCF, it has been shown that the inclusion of short-range ordering in the first two coordination shells of the disordered networks can lead to an increased ordering of the atomic radial distribution in distant coordination shells. A comparison of these results with those obtained from large *a*-Si and disordered crystalline configurations reveals that the shell pair-correlation functions for the coordination shells of *a*-Si at radial distances of 20–30 Å are considerably ordered and that this radial ordering manifests in the form of weak oscillations in the total PCF of *a*-Si, which can be expressed as a sum of the partial radial distributions from each coordination shell. By using the full width at half maximum of the peak(s) of the partial PCFs and the Shannon information as a measure of the degree of order/disorder, one arrives at the conclusion that local atomic correlations can considerably affect the distribution of atoms in *a*-Si up to a distance of 40 Å.

An analysis of the amplitude of radial oscillations in the reduced PCF of 400,000-atom MD models of *a*-Si shows that the envelope function of the reduced PCF decays almost exponentially and the resulting decay length (of 4.81 Å) is found to be close to the experimental value (of 4.23 Å), estimated from the Fourier transform of the diffraction data obtained for annealed samples of *a*-Si. Likewise, the period of the extended-range oscillations (for MD models) is found to be about 3.2 Å, which compares well with the corresponding experimental value of 3.03 Å for annealed samples. The study also shows that the structure factor of *a*-Si can be expressed as a linear combination of a series of Gaussian functions, whose amplitude is modulated by a *sinc* function. A convergence study of the intensity of the FSDP, using the structure factor obtained from the Gaussian approximation, with respect to the number of peaks in real space shows that the structure of the FSDP is primarily determined by the radial correlations originating from a distance of up to 20 Å in *a*-Si networks, which leads to the conclusion that the ERO has no discernible effects on the FSDP in *a*-Si.

Chapter 4

ORIGIN AND THE STRUCTURE OF THE FIRST SHARP DIFFRACTION PEAK OF AMORPHOUS SILICON

The discussion presented in this chapter has been adopted from a publication by **D. Dahal, H. Warren, P. Biswas; On the Origin and Structure of the First Sharp Diffraction Peak of Amorphous Silicon,** *Physica Status Solidi B***, 258: 2000447**

4.1 Introduction

The first sharp diffraction peak (FSDP) is a distinct feature of many noncrystalline solids, which are characterized by the presence of a peak in the low wavevector region (1–2 Å^{-1}) of the structure factor of the solids. Although the origin of the FSDP in many multinary glasses is not yet fully understood from an atomistic point of view, it has been shown that the FSDP is primarily associated with the presence of the short-range and medium-range order, which entail voids, chemical ordering, large ring structures, local topology, and atomic correlations between constituent atoms in the amorphous environment of the solids [140, 141, 142, 70, 143].

The FSDP is ubiquitous in many disordered condensed-phase systems. Numerous experimental [140, 141, 144, 145, 60] and theoretical [142, 107, 146] studies have reported the (near) universal presence of the FSDP in glasses and liquids/melts. In glasses, the origin of the FSDP can be largely attributed to the presence of layered structures [147], interstitial voids [142, 70, 143], chemical disorder [70], and large ring structures [60] in the networks, which constitute a real-space description of atomic correlations on the nanometer length scale. Elliott [142] has shown that the FSDP in binary glasses can be interpreted as a prepeak in the concentration-concentration structure factor, which is caused by the presence of the chemical ordering between constituent atoms in the networks. Likewise, the interstitial voids have been found to play an important role in the formation of the FSDP in tetrahedral amorphous semiconductors [70], e.g., *a*-Si. On the other hand, Susman et al. [60] have reported that in binary AX_2 glasses, the A–A and A–X correlations within the extended ring structures can give rise to the FSDP. Busse and Nagel [147] have suggested that the existence of the FSDP in *g*-As_2Se_3 can be ascribed to the inter-layer atomic correlations

in the glassy network. Experimental studies on $GeSe_3$ and $GeSe_5$ glasses by Armand et al. [148] have indicated that the Ge–Ge atomic correlation on the length scale of 6-7 Å is the primary cause of the FSDP, which is supported by molecular-dynamics studies by Vashishta et al. [107].

The behavior of the FSDP in covalent glasses often shows an anomalous dependence with respect to temperature [141, 149], pressure [149, 68], and composition [144, 150]. Following the well-known Debye-Waller [151] behavior, one may assume that the peaks in the structure factor should decrease with the increase of the temperature of the system. However, the first (sharp) diffraction peak of many glassy systems has been found to remain either invariant or become more intense and narrower at high temperature [141, 67]. A notable exception is vitreous silica (v-SiO_2), which does not follow the behavior stated above. The intensity of the FSDP of v-SiO_2 has been observed to decrease with increasing temperature, due to the thermally induced motion of the atoms and the associated diffused scattering [152], leading to the broadening of the first peak [149]. Likewise, the position and the width of the FSDP have been observed to vary with the pressure or density of the glasses [67, 68]. Neutron diffraction [153] and molecular-dynamics studies of densified v-SiO_2 [154] have indicated that the intensity and the width of the FSDP can change with the density of the samples/models. These changes can be attributed to the frustration induced by the reduction of Si–O–Si bond angles and the changes in the Si–Si and O–O atomic correlations on the length scale of 4–10 Å when the system is densified. A similar conclusion can be made for GeO_2 glass, when the glass is densified [106]. The addition of extrinsic atoms in glassy networks has been also found to affect the first sharp diffraction peak. Lee and Elliott [150] have noted that the inclusion of extrinsic atoms in v-SiO_2 can change the chemical ordering of the interstitial voids in the glassy network, which can alter the shape/width of the FSDP.

While the great majority of earlier studies mostly examined the origin and the behavior of the FSDP in borate, chalcogenide, oxide, and silicate glasses [143, 155, 58, 156], there exist only a few studies [142, 70, 100] that address the structure of the FSDP in tetrahedral amorphous semiconductors, such as a-Si and a-Ge. Elliott and coworkers [70, 100] have addressed the problem at length, but their studies are primarily focused on the origin of the extended-range oscillations (ERO) in a-Si. The results from their studies, which are based on the (Fourier) inversion of experimental structure-factor data of Fortner and Lannin [29] and highly defective a-Si models of Holender and Morgan [123], suggest that the ERO arise from the preferential propagation of second-neighbor correlations in the network, which in turn can significantly affect the intensity of the FSDP up to a radial length scale of 20 Å. However, no systematic analysis of the results with respect to the size of models is

provided and, thus, in the absence of direct numerical evidence, it is not clear to what extent the intensity of the FSDP is truly affected by atomic correlations originating from radial distances beyond 15 Å.

The key purpose of this chapter is to provide a systematic study of the structure of the FSDP, chapter with an emphasis on the position, intensity, and width of the peak, with the size of the models. In addition, the origin of the FSDP in *a*-Si is addressed by obtaining a quantitative estimate of the contribution of atomic pair correlations from different radial shells and their effect on the intensity and position of the FSDP. The relationship between the peaks in the structure factor and its real-space counterpart, the reduced pair-correlation function, is addressed, and an approximate functional relation between the position of the FSDP in *a*-Si and the radial distance of the atoms in the second radial shell of the amorphous network is obtained. Throughout this chapter, we shall use the term FSDP to refer to the first peak of the structure factor of *a*-Si at $Q_0 = 1.9$–2 Å^{-1} in discussing our results. Likewise, the term principal peak will be used to indicate the second peak at $Q = 3.6$ Å^{-1}. For amorphous silicon, this terminology has been used previously by others [70, 100], and it is consistent with the fact that the peak at Q_0 is indeed the first peak of $S(Q)$ and that it is reasonably sharp and strong with a value of the intensity $S(Q_0)$, which is about 67% of the intensity of the principal peak.

The rest of the chapter is planned as follows. Section 4.2 provides a brief description of the simulation method for producing atomistic models of *a*-Si via the modified Wooten-Winer-Weaire (WWW) [26, 38] method, the calculation of the radial pair-correlation function, and the structure factor for these models. This is followed by results and discussion in section 4.3, with an emphasis on the origin and the structure of the FSDP. The conclusions of this study are presented in section 4.4.

4.2 Models and Methods

For the purpose of generating atomistic models of *a*-Si, we have employed the well-known WWW method. The details of the method can be found in Refs. [26, 38]. Here, we have used the modified version of the method, developed by Barkema and Mousseau (BM) [38]. In the modified WWW approach, one starts with a random configuration that consists of N atoms in a cubic supercell of length L. The volume of the supercell is chosen in such a way that the mass density of the model corresponds to about 2.28 g.cm^{-3}, as observed in *a*-Si samples produced in laboratories [101, 28]. Initially, following the BM ansatz, the nearest neighbors of each atom are so assigned that a tetravalent network is formed [157]. This is achieved by choosing a suitable nearest-neighbor cutoff distance, up to 3 Å, between Si

atoms. The resulting tetravalent network is then used as the starting point of the WWW bond-switching algorithm. New configurations are generated by introducing a series of WWW bond switches, which largely preserve the tetravalent coordination of the network and the energy of the system is minimized using Monte Carlo (MC) simulations. The acceptance or rejection of a proposed MC move is determined via the Metropolis algorithm [158] at a given temperature. Here, the energy difference between two configurations is calculated locally by using the Keating potential [34], which employs an atomic-index-based nearest-neighbor list of the tetravalent network during MC simulations. In addition, the total energy of the entire system is relaxed from time to time using the Stillinger-Weber potential [76]. Finally, the configurations obtained from the modified WWW method were relaxed using the first-principles density-functional code SIESTA [159]. For the models with 216 atoms to 3000 atoms, a full self-consistent-field calculation, using the generalized-gradient approximation (GGA) [86] and a set of double-zeta basis functions, was carried out. The remaining models of size from 4096 atoms to 6000 atoms were treated using the non-self-consistent Harris-functional approach [160] with a single-zeta basis set in the local density approximation (LDA) [85]. To conduct configurational averaging of simulated data, we have generated 10 models for each size starting with different random configurations using independent runs.

Once the atomistic models are generated, the calculation of the structure factor proceeds by computing the reduced pair-correlation function. The latter is defined as $G(r) = 4\pi r n_0[g(r)-1]$, where $g(r)$ and n_0 are the pair-correlation function and the average number density of a model, respectively. Assuming that the distribution of the atoms in a disordered network is isotropic and homogeneous, the structure factor, $S(Q)$, can be written as,

$$\begin{aligned} S(Q) &= 1 + \frac{1}{Q}\int_0^{\infty} G(r)\sin(Qr)\,dr \\ &\approx 1 + \frac{1}{Q}\int_0^{R_c} G(r)\sin(Qr)\,dr, \end{aligned} \tag{4.1}$$

where R_c is the length of the half of the cubic simulation cell. The conventional periodic boundary conditions are used to minimize surface effects and to calculate the pair-correlation function in Eq. (4.1).

4.3 Results and Discussion

Equation (4.1) suggests that the shape of the FSDP can be fully determined via the Fourier (sine) transformation of the reduced pair-correlation function $G(r)$, provided that $G(r) \to 0$ as $r \to R_c$. Since the shape of the FSDP is primarily determined by the structure factor in the

vicinity of $Q_0 \approx 2$ Å^{-1}, it is apparent that one requires sufficiently large models of *a*-Si, in order to satisfy the condition above, for an accurate determination of the FSDP. To this end, we first validate the structural models of *a*-Si, obtained from the modified WWW method. Since the latter is a well-established method, we restrict ourselves to the pair-correlation function (PCF), the bond-angle distribution (BD), and the coordination number (CN) of Si atoms in the network. It has been shown elsewhere [48] that the knowledge of the PCF, the BD, and the CN of the atoms are sufficient to establish whether a structural model can produce the correct electronic and vibrational properties of *a*-Si or not. The full structure factor and the normalized bond-angle distribution, obtained from a set of 3000-atom models of *a*-Si, are plotted in Figs. 4.1 and 4.2, respectively. For the purpose of configurational averaging, the results were averaged over 10 independent models of an identical size. The simulated values of $S(Q)$ in Fig. 4.1 can be seen to agree well with the corresponding experimental data reported in Ref. [28]. Likewise, the full width at half maximum (FWHM) of the bond-angle distribution in Fig. 4.2, about 21.4°, matches with the observed value of 18°–24° obtained from the Raman "optic peak" measurements [161]. The FWHM of the bond-angle distribution for the WWW models is also found to be consistent with those obtained from high-quality molecular-dynamics simulations [162, 163], and data-driven information-based approaches [48, 49], developed in recent years. A further characterization of the models is possible by examining the statistics of the CN of Si atoms, the dihedral-angle distribution, and the presence of various irreducible rings in the amorphous structures. However, since the WWW models have been extensively studied and validated in the literature, we will not linger over the validation issue and get back to the central topic of this chapter by listing the coordination-number statistics of the atoms and some key structural properties of the WWW models in Table 4.1. The corresponding results for the DFT-relaxed models are provided in Table 4.2.

4.3.1 Characterization, origin, and the structure of the FSDP in amorphous silicon

Figure 4.3 shows the structure factor of *a*-Si obtained from four different models, of size from 216 atoms to 3000 atoms, and experiments [101]. As before, the simulation data are obtained by averaging over 10 independent models for each size, whereas the experimental data refer to as-implanted samples of *a*-Si in Ref. [101]. An examination of Fig. 4.3 leads to the following observations. Firstly, it is apparent that the 216-atom model shows a marked deviation from the experimental data near the FSDP, indicating noticeable finite-size effects originated from small models of linear size of about 16 Å. By contrast, the larger models, consisting of 1000 to 3000 atoms, have produced the peak

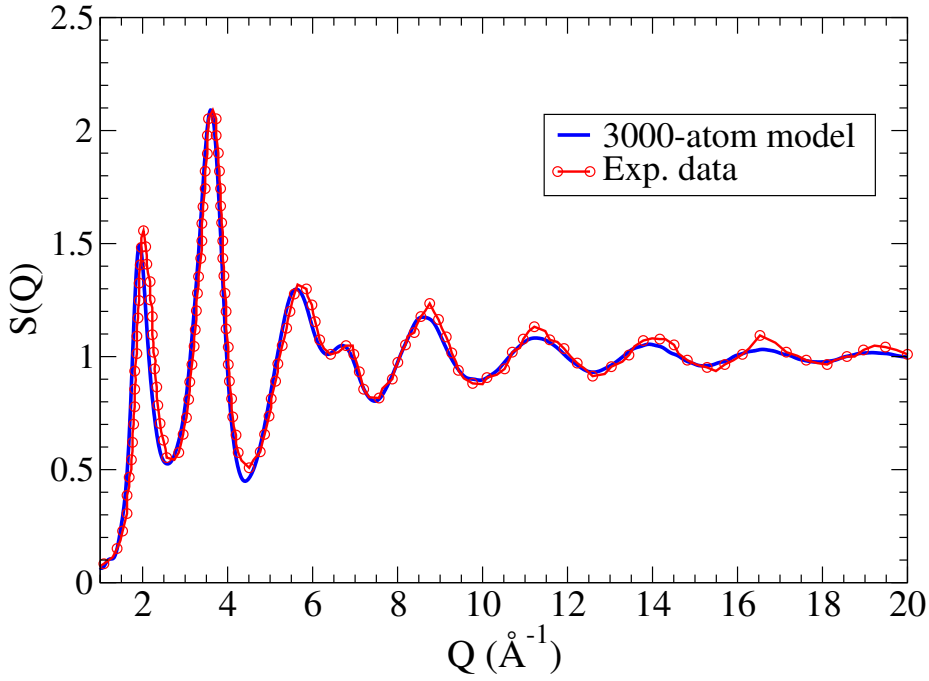

Figure 4.1: The structure factor of *a*-Si obtained from simulations and experiments. The simulated data are from 3000-atom WWW models of density 2.28 g.cm^{-3}, whereas the experimental data correspond to those from Ref. [28]. The simulated data are obtained by averaging over 10 models from independent runs.

Table 4.1: Structural properties of *a*-Si models before DFT relaxation. The number of i-fold-coordinated atoms (in percent) in the network is indicated as n_i. Bond lengths and bond angles/widths are expressed in Å and degree, respectively. The results are obtained by averaging over 10 configurations using a nearest-neighbor cutoff value of 2.8 Å.

Size	Bond angle & width		Coordination number			Bond length
N	$\langle\theta\rangle$	$\Delta\theta$	n_4	n_3	n_5	$\langle r\rangle$
216	109.25	9.11	100	0	0	2.35
300	109.25	9.32	100	0	0	2.35
512	109.26	9.41	100	0	0	2.35
1000	109.27	9.16	100	0	0	2.35
2000	109.27	9.31	99.95	0	0.05	2.35
3000	109.26	9.39	99.94	0	0.06	2.35
4096	109.26	9.26	99.95	0	0.05	2.35
5000	109.27	9.31	99.97	0	0.03	2.35
6000	109.26	9.39	99.96	0	0.04	2.35

intensity more accurately. Secondly, all the models consistently underestimate the position of the experimental FSDP [101] at Q_0=1.99 Å^{-1}, by an amount of 0.045 Å^{-1}. One can surmise a number of possible reasons for this discrepancy. These include the inadequacy of

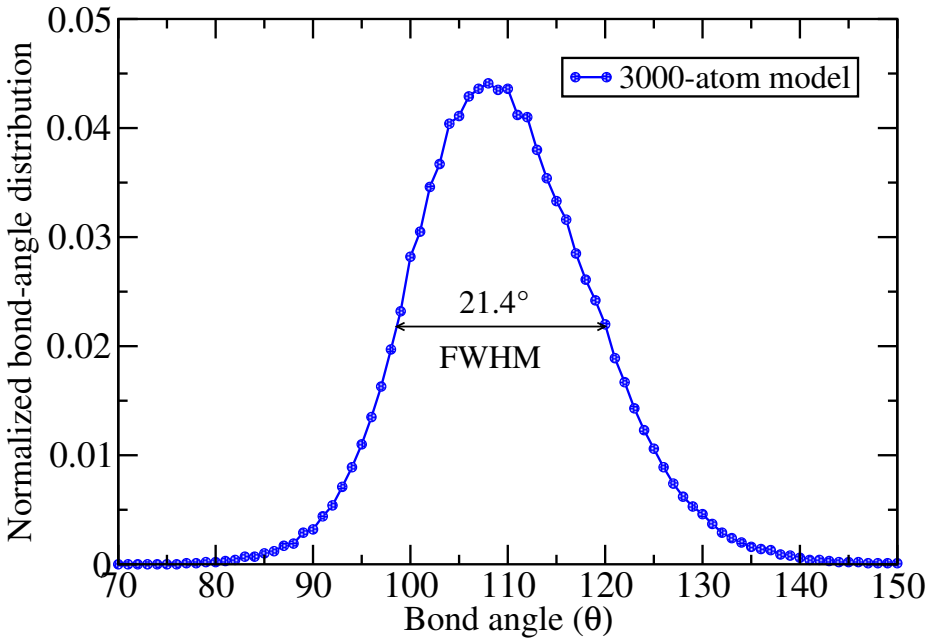

Figure 4.2: The normalized bond-angle distribution for *a*-Si, obtained for 3000-atom WWW models. The full width at half maximum (FWHM) corresponds to a value of 21.4°. The distribution is obtained by averaging over 10 independent models.

Table 4.2: Structural properties of DFT-relaxed models of *a*-Si. The total number of *i*-fold-coordinated atoms (in percent) present in the relaxed networks is indicated as n_i. Average bong lengths and bond angles/widths are expressed in Å and degree, respectively. Asterisks indicate the use of single-zeta basis functions and the non-self-consistent Harris-functional approximation for relaxation of large models.

Model size	Bond angle & width		Coordination number			Bond length
N	$\langle\theta\rangle$	$\Delta\theta$	n_4	n_3	n_5	$\langle r\rangle$
216	109.11	10.14	100	0	0	2.36
300	109.15	10.22	100	0	0	2.36
512	109.13	10.45	100	0	0	2.36
1000	109.15	10.14	100	0	0	2.36
2000	109.14	10.3	99.95	0	0.05	2.36
3000	109.13	10.4	99.96	0.01	0.03	2.36
4096*	109.02	10.82	99.95	0.01	0.04	2.37
5000*	109.01	10.9	99.94	0.01	0.05	2.37
6000*	109.01	10.92	99.95	0.01	0.04	2.37

the classical potentials, the uncertainty of the actual density of the *a*-Si sample(s) used in experiments, and a possible sample-to-sample dependence of the experimental results. The last point can be appreciated by noting that the experimental value of Q_0, for as-implanted

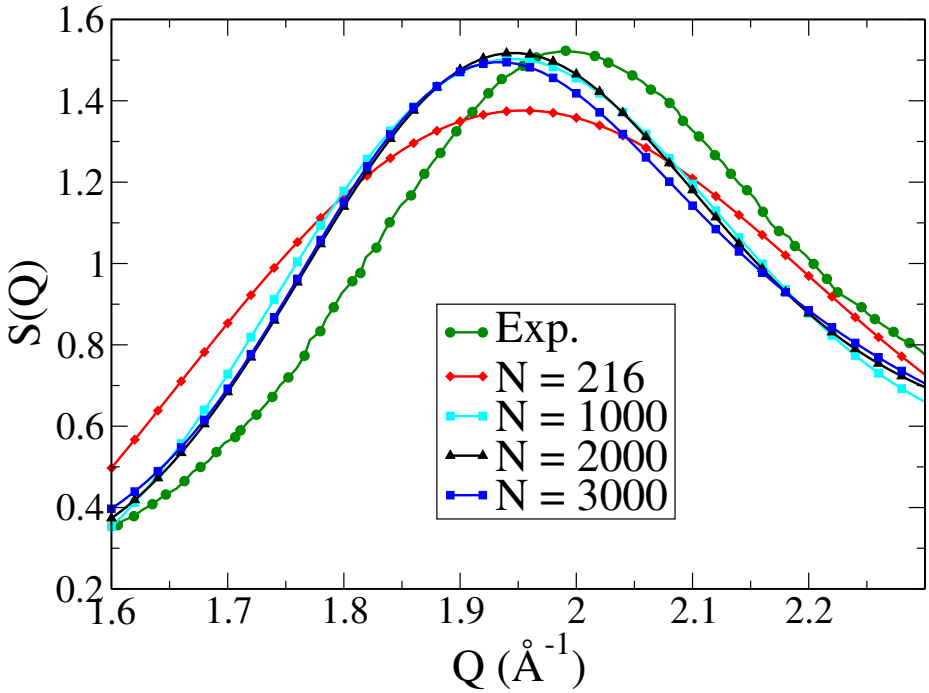

Figure 4.3: The structure factor of *a*-Si in the vicinity of the FSDP from simulations and experiments. Experimental data (•) correspond to as-implanted samples from Ref. [101], whereas simulated data refer to 216-atom (♦), 1000-atom (■), 2000-atom (▲), and 3000-atom (■) unrelaxed WWW models.

samples of *a*-Si, reported in Refs. [29], [101], and [28] differ from each other by about 0.07 Å^{-1} (see Fig. 4.11). Finally, a first-principles total-energy relaxation of the models, using the density-functional code SIESTA [159], somewhat remedies this issue at the expense of the reduction of the peak intensity. This is illustrated in Fig. 4.4, where we have plotted both the reduced pair-correlation function (see inset) and the configurational-average structure factor from ten 3000-atom models before and after total-energy relaxation. The increase of the peak height of $G(r)$ upon relaxation is not surprising in view of the fact that first-principles relaxations minimized the total energy of the system by reducing the bond-length disorder at the expense of a minor increase of the bond-angle disorder. The latter is reflected in the root-mean-square (RMS) width, $\Delta\theta$, of the bond-angle distribution before and after relaxation in Tables 4.1 and 4.2, respectively. By contrast, the shape of the structure factor near the FSDP remains more or less the same after relaxation, except for a small shift of the FSDP toward the higher values of Q.

Having addressed the overall shape of the structure factor and the FSDP for a number of models of varying sizes, we now examine the origin of the FSDP in terms of the real-space structure of *a*-Si networks. While it is well-understood that the FSDP in *a*-Si arises from

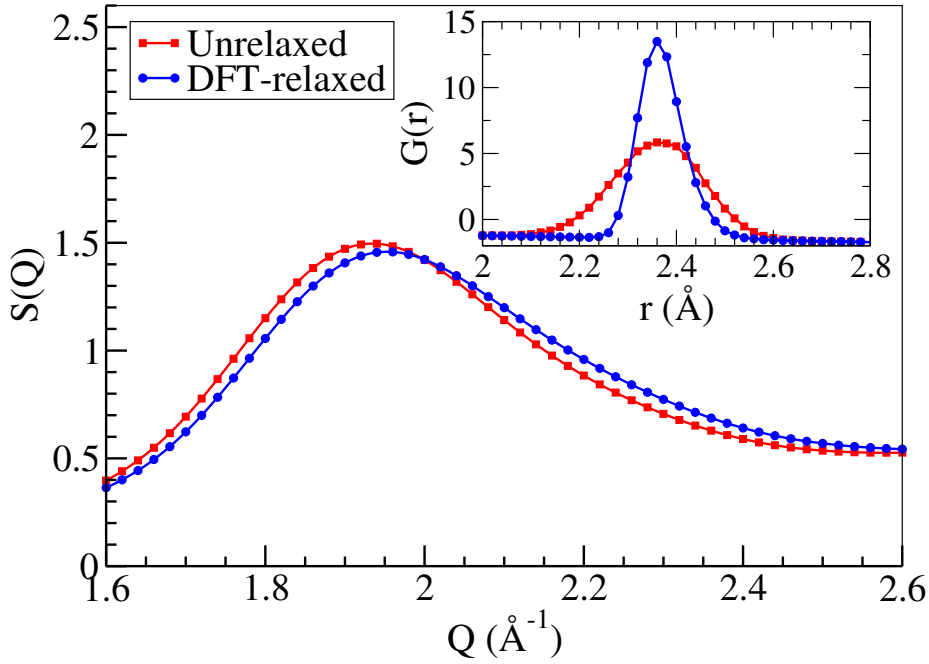

Figure 4.4: Effects of approximate first-principles relaxations on the position and the intensity of the FSDP of *a*-Si for a 3000-atom model before (■) and after (●) relaxation. A small shift of the diffraction peak toward higher values of Q is accompanied by a slight reduction of the peak intensity in the relaxed model. The corresponding reduced pair-correlation functions near the first peak are shown in the inset.

the medium-range order in the network, which entails a length scale of a few to several angstroms, a quantitative characterization of the contribution from different radial shells is still missing in the literature. We address this aspect of the problem by examining the role of radial atomic correlations in forming the FSDP, via the Fourier transform of the reduced PCF, and provide a quantitative measure of the contributions that originate from the increasingly distant radial shells in the amorphous environment of silicon. This can be achieved by writing,

$$S(Q) = 1 + F(Q) = 1 + \sum_{i=1}^{n} F_i(Q; R'_i, R'_{i+1}),$$

where,

$$F_i(Q; R'_i, R'_{i+1}) = \frac{1}{Q} \int_{R'_i}^{R'_{i+1}} G(r) \sin(Qr)\, dr. \tag{4.2}$$

In Eq. (4.2), $F_i(Q; R'_i, R'_{i+1})$ is the contribution to $F(Q)$ from the reduced PCF, $G(r)$, at distances between R'_i and R'_{i+1}. The contribution from a given radial shell can be obtained by a suitable choice of R'_i and R'_{i+1}, where $R'_{i+1} > R'_i$, and an appropriate set $\{R'_1, \ldots, R'_n\}$ covers the entire radial (integration) range to obtain the full $F(Q)$. For example, a choice

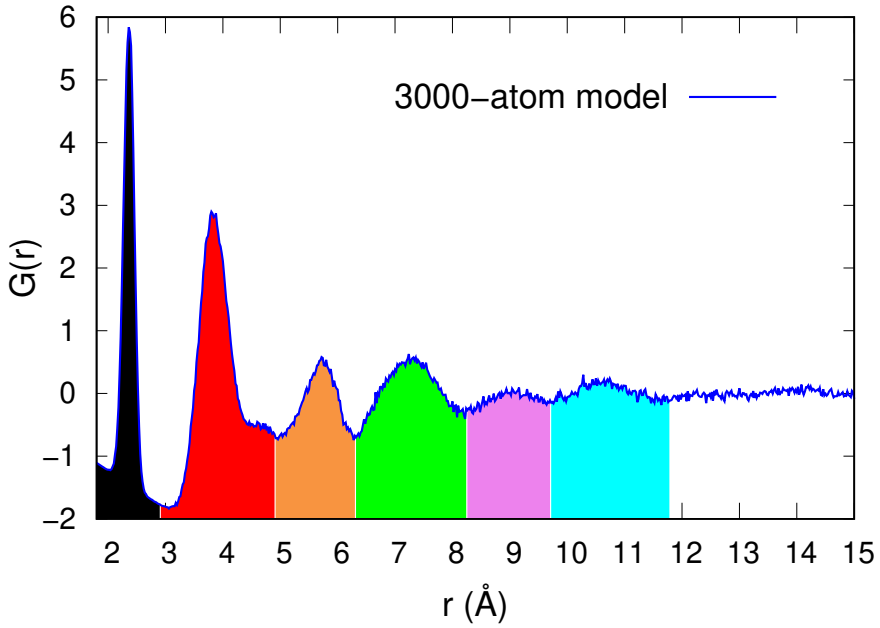

Figure 4.5: The reduced pair-correlation function, $G(r)$, of a-Si obtained from configurational averaging of ten 3000-atom WWW models. The presence of the first six radial shells, which extend up to a distance of $\approx$ 12 Å, is highlighted in different colors.

of R'_1 = 0 Å and R'_2 = 2.8 Å yields $F_1(Q;R'_1,R'_2)$, and R'_2=2.8 Å and R'_3=4.9 Å provides $F_2(Q;R'_2,R'_3)$. The origin of the FSDP and the principal peak can be studied by computing various $F_i(Q)$ in the vicinity of 2 Å^{-1} and 3.6 Å^{-1}, respectively. The appropriate values of R'_i for different radial shells can be obtained by inspecting the reduced PCF of a-Si. This is illustrated in Fig. 4.5, by plotting the configurational-average $G(r)$ obtained from a set of ten 3000-atom models. We should emphasize that the radial shells correspond to the radial regions between two neighboring minima in the reduced PCF. Except for the first radial shell, the radial regions, defined by a pair of consecutive minima in $G(r)$, are not necessarily identical to the corresponding atomic-coordination shells due to the overlap of the atomic distribution from different coordination shells.

Figure 4.6 shows the contribution to $F(Q)$ in the vicinity of 2 Å^{-1} from the first six radial shells. The plots for different radial shells are indicated by the corresponding shell color as depicted in Fig. 4.5. It is evident that the chief contribution to the FSDP comes from $F_2(Q)$, which is followed by $F_4(Q)$ and $F_6(Q)$ in the descending order of magnitude. $F_2(Q)$ and $F_4(Q)$ play a crucial role in determining both the intensity and the position of the FSDP, while $F_3(Q)$ and $F_5(Q)$ contribute very little to none. By contrast, $F_1(Q)$ monotonically changes in the vicinity of the FSDP and thus contributes to the intensity (and the shape) of the FSDP near Q_0 to some degree but does not play any noticeable role in determining the

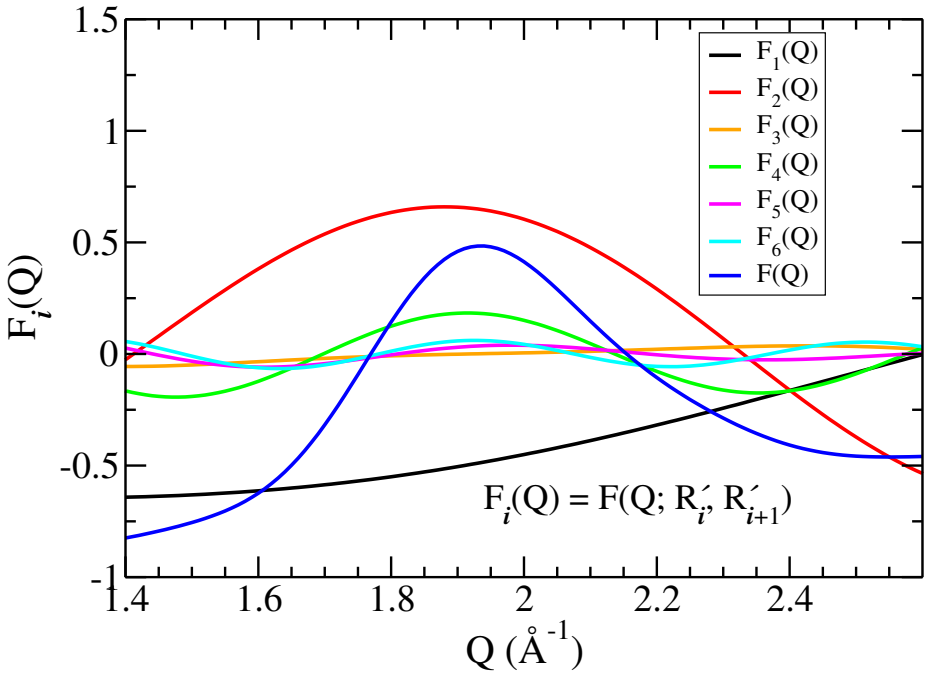

Figure 4.6: The contribution to the FSDP, $F_i(Q)$, near Q_0, originating from the first six radial shells and the total $F(Q)$ (blue). The results correspond to 3000-atom WWW models, and are averaged over ten configurations. The color of the plots corresponds to the color of the radial shells in Fig. 4.5.

position of Q_0. It is therefore apparent that the position of the FSDP in *a*-Si is primarily determined by the information from the second radial shell, followed by the fourth and sixth radial shells, whereas the rest of the distant radial shells provide small perturbative corrections. The enumeration of the radial shell-by-shell contribution to $F(Q)$ is a significant result to our knowledge, which cannot be quantified from a phenomenological understanding of the Fourier transform of $G(r)$ in Eq. (4.1). A similar analysis reveals that the contribution to the principal peak at 3.6 Å^{-1} mostly arises from $F_2(Q)$, $F_1(Q)$, $F_4(Q)$, and $F_3(Q)$, in the decreasing order of magnitude. Once again, $F_1(Q)$ is found to provide a positive but monotonically decreasing contribution with increasing Q in the vicinity of the principal peak. Thus, the peak at 3.6 Å^{-1} is principally contributed by the first four radial shells in the reduced PCF. This observation amply justifies the use of the term 'principal peak' to describe the peak at 3.6 Å^{-1} in the structure factor of *a*-Si. Figure 4.7 shows the results for the principal peak using the same color code as in Fig. 4.5.

4.3.2 Relation between peaks in $S(Q)$ and $G(r)$

The results presented in the preceding section on the basis of the partitioning of $F(Q)$ reveal that the information from the second and fourth radial shells largely determine the structure, i.e., the position, intensity, and width, of the FSDP in *a*-Si. We now provide a physical interpretation of the numerical results and demonstrate that the emergence of the first two peaks in $S(Q)$, near 2 Å^{-1} and 3.6 Å^{-1}, respectively, can be deduced simply from the knowledge of the reduced PCF and the behavior of the integral, involving the sinc(x) (i.e., $\sin x/x$) function, which defines the structure factor. Noting that the structure factor can be written as,

$$\begin{aligned} S(Q) &= 1+F(Q) = 1+\frac{1}{Q}\int_0^{R_c} G(r)\sin(Qr)\,dr \\ &= 1+\int_0^{R_c} rG(r)\left[\frac{\sin(Qr)}{Qr}\right]dr, \end{aligned} \tag{4.3}$$

it is elementary that the peaks in $F(Q)$ (and hence $S(Q)$) should appear approximately for those values of Qr for which both $\sin(Qr)/Qr$ and $rG(r)$ are maximum. Here, the r values in Qr are given by the maxima of $rG(r)$. Since the maxima of $\sin(Qr)/Qr$ and $\sin(Qr)$ are very close to each other [164] for $Qr > 0$, and the maxima of $G(r)$ and $rG(r)$ practically coincide, one may use the maxima of $\sin(Qr)$ and $G(r)$ in determining the approximate location of the first two peaks in $S(Q)$. This implies Qr must satisfy, $\sin(Qr) = 1$, or $Qr = (4m+1)\pi/2$, where m=0, 1, 2, ... etc. Since the first two maxima of $G(r)$ are given by $r_1 \approx 2.35$ Å and $r_2 \approx 3.8$ Å, respectively, and $m = 0$ does not admit a physical solution [164], the first major contribution to the $F(Q)$ comes from the second radial shell for $r_2 = 3.8$ Å and $m = 1$. This gives, $Q_0 = 5\pi/(2\times r_2) = 2.07$ Å^{-1}. Likewise, the next contribution comes from, for $m = 2$, the fourth radial shell with a peak at $r_4 \approx 7.24$ Å in $G(r)$. This yields, $Q_0 = 9\pi/(2\times r_4) = 1.95$ Å^{-1}. A similar analysis shows that the principal peak (Q_1) gets its share from the first radial shell, for $m = 1$, at $Q_1 = 5\pi/(2\times r_1) = 3.34$ Å^{-1}, which is followed by the second radial shell, for $m = 2$, at $Q_1 = 9\pi/(2\times r_2) = 3.72$ Å^{-1}, the fourth radial shell, for $m = 4$, at $Q_1 = 17\pi/(2\times r_4) = 3.69$ Å^{-1}, and the third radial shell, for $m = 3$ and $r_3 = 5.72$, at $Q_1 = 13\pi/(2\times r_3) = 3.57$ Å^{-1}. The exact position of a peak in $S(Q)$ is determined by the sum of the contribution from the relevant radial shells, which introduce a minor deviation from the individual estimate above due to the approximate nature of our calculations. Table 4.3 presents a summary of the results obtained from the reasoning above. The estimated position of the peaks in $F_i(Q)$, for i=1 to 6, is listed in the Table. The first column, shown in light gray shading, corresponds to the maxima (r_i) of $G(r)$ up to a radial distance of 11 Å, whereas the second row, indicated by dark gray cells, lists the values of $Qr = (4m+1)\pi/2$

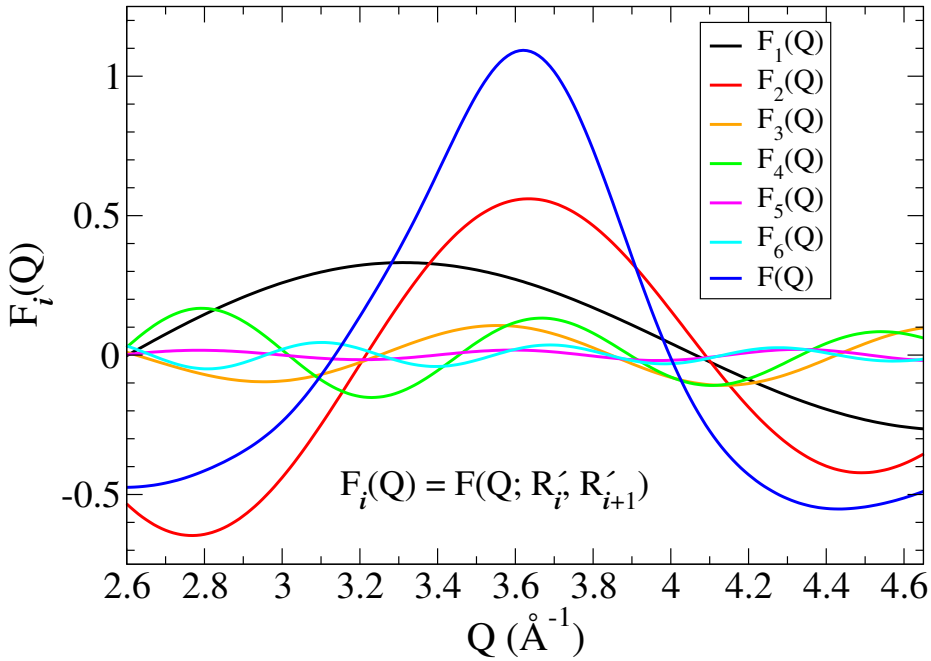

Figure 4.7: The contribution, $F_i(Q)$, to the principal peak at Q_1 = 3.6 Å^{-1} from the first six radial shells of the reduced pair-correlation function. The total $F(Q)$ is shown in blue color for comparison. The results are obtained via configurational averaging of data from ten 3000-atom models.

for m=1 to 6. The remaining six rows, between columns 1 and 8, indicate the peak positions in $F_i(Q)$ that are obtained by dividing the Qr values by the corresponding r_i value from the first column. The estimated positions of the FSDP and the principal peak for a number of combination of (r_i, m) are shown in Table 4.3 by green and red colors, respectively.

Conversely, assuming that the FSDP is located at $Q_0 \approx 2$ Å^{-1}, one arrives at the conclusion, by dint of our logic, that the contribution to the FSDP should come from $r = (4m+1)\pi/(2\times Q_0) = \pi/4, 5\pi/4, 9\pi/4$, and $13\pi/4$, etc., for m = 0 to 3. The first value of r, for m = 0, does not provide a physical solution but the remaining values at 3.93 Å, 7.07 Å, and 10.21 Å approximately correspond to the second peak, the fourth peak, and the sixth peak of $G(r)$ (cf. Fig. 4.5). A similar analysis can be done for the principal peak. The argument presented here suffices to explain why the information from the distant radial shells, for $r \geq 15$ Å, cannot contribute significantly in the formation of the FSDP. At large radial distances, when the reduced PCF rapidly vanishes and the concomitant numerical noises in $G(r)$ become increasingly stronger, $\sin(Qr)/Qr$ cannot find, or sample, suitable values of r with a large $G(r)$, for Q values near the FSDP, to satisfy the condition above.

Table 4.3: Estimated values of the peak positions, Q, in $F_i(Q)$, obtained from $Qr = (4m+1)\pi/2$ (dark gray cells in the second row for m=1 to 6) and the maxima of $G(r)$ (first column) in Å. The positions of the FSDP and the principal peak (PP) in F_is are indicated by green and red colors, respectively. The radial shells that contribute to the FSDP and the PP can be directly read off the first column.

Maxima	1	2	3	4	5	6	$\leftarrow m$
of $G(r)$	7.854	14.137	20.42	26.704	32.987	39.27	$\leftarrow Qr$
2.35	3.34	6.02	8.69	11.36	14.04	16.71	Peaks in F_1
3.8	2.07	3.72	5.37	7.03	8.68	10.33	Peaks in F_2
5.72	1.37	2.47	3.57	4.67	5.77	6.87	Peaks in F_3
7.24	1.08	1.95	2.82	3.69	4.56	5.42	Peaks in F_4
9.16	0.86	1.54	2.23	2.92	3.6	4.29	Peaks in F_5
10.74	0.73	1.32	1.9	2.49	3.07	3.66	Peaks in F_6

This leads to small $F_i(Q)$ for the distant radial shells. We have verified that the analysis presented here is consistent with the results from numerical calculations of $F_i(Q)$.

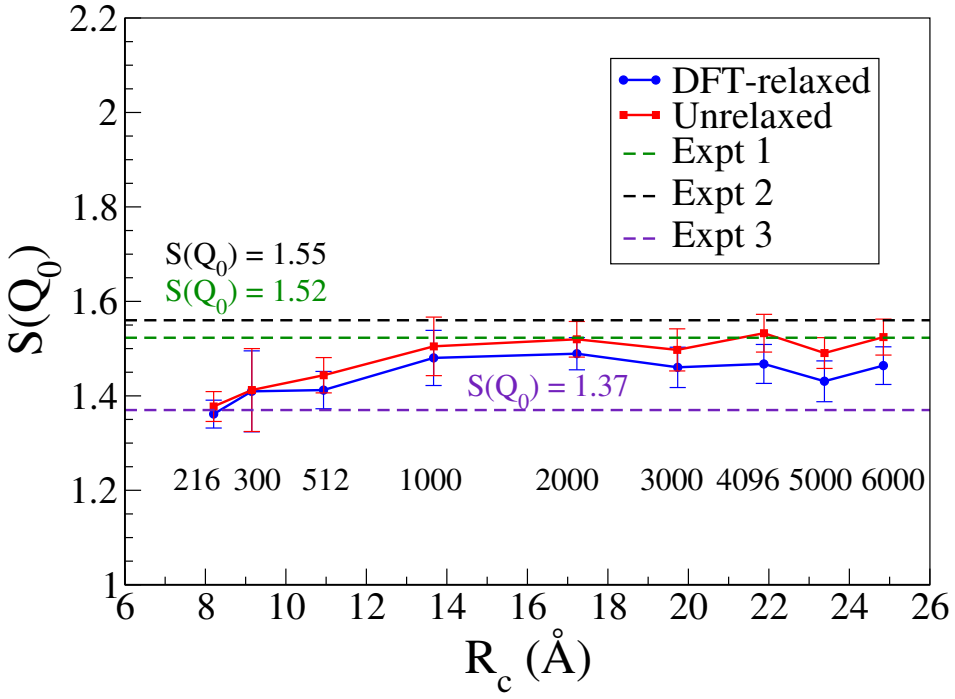

Figure 4.8: The dependence of the intensity of the FSDP, $S(Q_0)$, with the radial cutoff distance, R_c, for a number of models of different sizes, as indicated in the plot. The experimental values of $S(Q_0)$ reported in the literature are shown as horizontal dashed lines: 1) $S(Q_0)$=1.52 from Ref. [101]; 2) $S(Q_0)$=1.37 from Ref. [29]; and 3) $S(Q_0)$=1.55 from Ref. [28].

The results and discussion presented so far indicate that the radial information from the reduced PCF of up to a length scale of 15 Å plays a significant role in the formation of the FSDP. To further establish this point, we now conduct a systematic study of the structure of the FSDP in terms of the intensity and the width of the peak. The variation of the peak intensity with the size of the models is studied by plotting the value of $S(Q_0)$ against R_c for a number of DFT-relaxed/unrelaxed models, consisting of 216 atoms to 6000 atoms. Since R_c is given by the half of the linear size of the models, Fig. 4.8 essentially shows the dependence of $S(Q_0)$ on the radial pair correlations up to a distance of R_c, through the Fourier transform of $G(r)$. It is clear from the plots (in Fig. 4.8) that the intensity of the FSDP for both the relaxed and unrelaxed models varies considerably until R_c increases to a value of the order of 14 Å. This roughly translates into a model of size about 1000 atoms. For even larger values of R_c, the peak intensity is more or less converged to 1.48 for the unrelaxed models but considerable deviations exist for the value of DFT-relaxed models from the experimental value of $S(Q_0)$ of 1.52 in Ref. [101]. The deviation of the peak intensity from the experimental value for small models of *a*-Si can be readily understood. Since $G(r)$ carries considerable real-space information up to a radial distance of 15 Å, possibly 20 Å for very large models, small models with R_c values less than 15 Å cannot accurately produce the peak position using Eq. (4.1). On the other hand, the peak intensity for the DFT-relaxed models deviates noticeably (about 0.2–12%) from their unrelaxed counterpart and the experimental value for as-implanted samples in Refs. [101], [29], and [28]. This apparent deviation for the bigger models is not particularly unusual and it can be attributed, at least partly, to: 1) the use of approximate total-energy calculations in the relaxation of large models, via the non-self-consistent Harris-functional approach using minimal single-zeta basis functions; 2) the intrinsic difficulties associated with quantum-mechanical relaxations of large models; and 3) the sample dependence of experimental results, showing a considerable difference in the value of $S(Q_0)$ for as-implanted samples in Fig. 4.8, which is as high as 0.18 from one experiment to another. Thus, the results obtained in this study are well within the range of the experimental values reported in the literature [29, 101, 28].

The full width at half maximum, or FWHM, of the FSDP for different models is plotted against R_c in Fig. 4.9. A somewhat high value of the FWHM for the large DFT-relaxed models is a consequence of the reduction of the peak intensity. As the intensity of the peak reduces, the FWHM increases slightly due to the widening of the diffraction plot away from the peak. An inspection of Figs. 4.8 and 4.9 appears to suggest that the values of FWHM and $S(Q_0)$ are somewhat correlated with each other. In particular, amorphous-silicon models exhibiting smaller values of $S(Q_0)$ (in Fig. 4.8) tend to produce somewhat larger values of FWHM in Fig 4.9, irrespective of the size of the models and DFT relaxation. This is

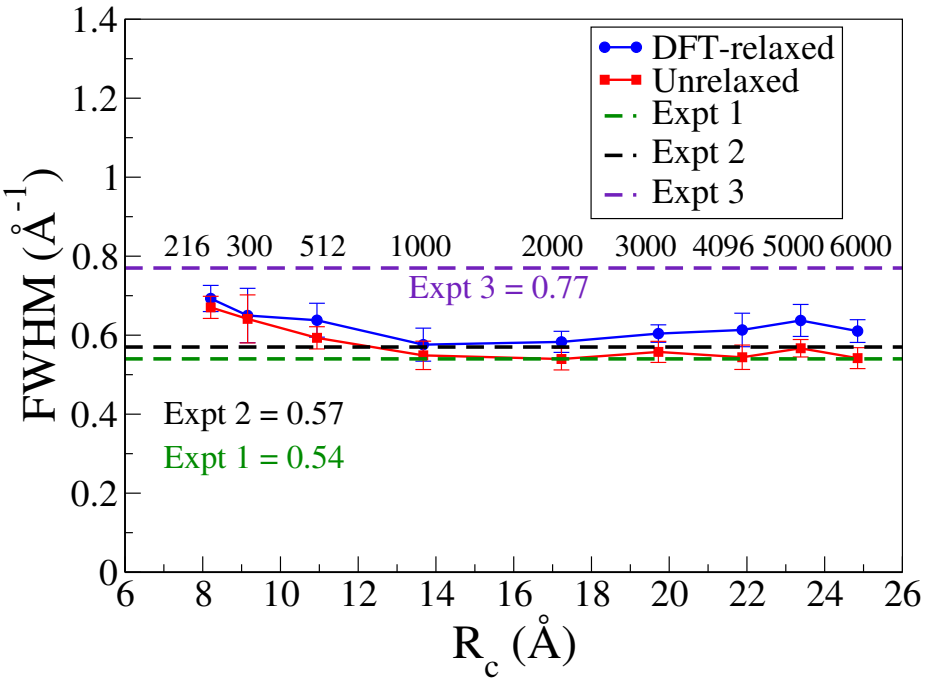

Figure 4.9: The full width at half maximum (FWHM) of the FSDP at Q_0 for a number of models before (■) and after (●) DFT relaxations. The horizontal dashed lines indicate the experimental values of 0.54 Å^{-1} (green), 0.57 Å^{-1} (black), and 0.77 Å^{-1} (indigo) for as-implanted samples of *a*-Si from Refs. [101], [28], and [29], respectively.

apparent in Fig. 4.10, where FWHM and $S(Q_0)$ values for all configurations and sizes are presented in the form of a scattered plot. A simple analysis of FWHM and $S(Q)$ data by computing the Pearson correlation coefficient, r_{XY}, confirms the suggestion that FWHM and $S(Q_0)$ values are indeed linearly correlated with each other and have a correlation coefficient of $r_{XY} = -0.9$. The linear least-square (LS) fit of the data are also shown in Fig. 4.10 by a solid (red) line. The great majority of the FWHM and $S(Q)$ values in Fig. 4.10 can be seen to have clustered along the straight line within a rectangular region bounded by the experimental values of FWHM and $S(Q_0)$, from 0.54 to 0.77 Å^{-1} and 1.37 to 1.55, respectively.

Likewise, the dependence of the position of the FSDP with R_c for the unrelaxed and DFT-relaxed models is illustrated in Fig.4.11. For the unrelaxed models, Q_0 is observed to converge near 1.95 Å^{-1}, whereas the corresponding value for the DFT-relaxed models hovers around 1.97 Å. In both the cases, Q_0 is within the range of the experimental values, from 1.95 Å^{-1} to 2.02 Å^{-1}, shown in Fig. 4.11.

In summary, a systematic study of *a*-Si models, consisting of 216 to 6000 atoms, firmly establishes that the structure of the FSDP in *a*-Si is mostly determined by radial pair

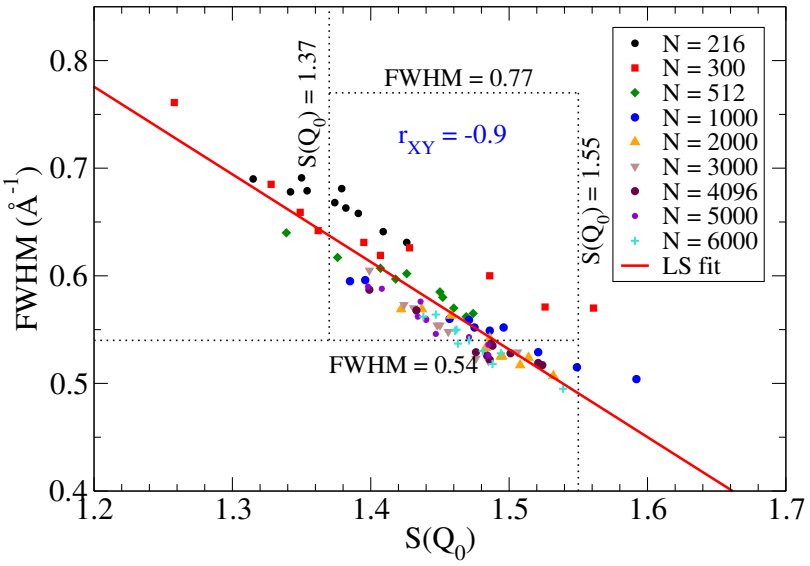

Figure 4.10: A scattered plot showing the presence a clear correlation between the FWHM and $S(Q_0)$ of the FSDP for a number of models of varying system sizes. The solid (red) line corresponds to the linear least-square (LS) fit of the data, whereas $r_{XY} = -0.9$ indicates the Pearson correlation coefficient for the data sets. The horizontal and vertical dotted lines indicate the experimental values of FWHM and $S(Q_0)$, respectively, obtained for as-implanted samples of *a*-Si.

correlations up to a distance of 15 Å, as far as the size of the largest models employed in this study is concerned. Further, the major contribution to the FSDP arises from the second and fourth radial shells, along with small residual contributions from the distant radial shells at a distance of up to 15 Å.

4.3.3 The FSDP and the radial shell structures of *a*-Si

Earlier, in sections 4.3.1 and 4.3.2, we have demonstrated that the position of the FSDP, Q_0, is primarily determined by $F_2(Q)$ and, to a lesser extent, $F_4(Q)$. This leads to a possibility of the existence of a simple functional relationship between Q_0 and a suitable length scale in the real space involving the radial atomic correlations in the network. In this section, we will show that an *approximate* relationship between Q_0 and the average radial distance, $\langle R_2 \rangle$, of the atoms in the second (radial) shell does exist. Below, we first provide a rationale behind the origin of this relationship, which is subsequently corroborated by results from direct numerical calculations.

The first hint that an approximate relationship may exist follows from the behavior of Q_0 with the (mass) density, ρ, of the models. In Fig. 4.12, we have plotted the variation of Q_0 against ρ for *a*-Si. For this purpose, the density of a set of 3000-atom models is

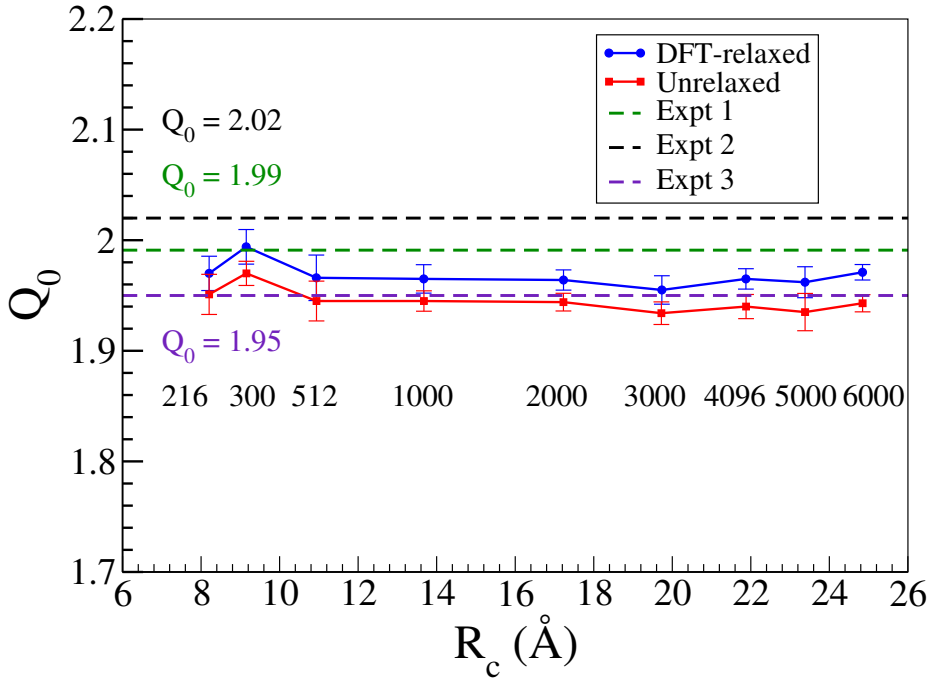

Figure 4.11: The dependence of the position of the FSDP, Q_0, with the size of the models before (▪) and after (•) DFT relaxations. The horizontal lines correspond to the experimental value of Q_0 for as-implanted samples of *a*-Si from Refs. [101] (green), [28] (black), and [29] (indigo).

varied, within the range from 2.12 g.cm^{-3} to 2.32 g.cm^{-3}, by scaling the length of the cubic simulation cell and the position of the atoms therein. This involves a tacit assumption that for a small variation of the density, by about ±5%, the atomistic structure of the network would remain unchanged and that a simple scaling approach should suffice to generate low/high-density models. Given that the WWW models of *a*-Si do not include any extended defects and voids in the network, the scaling assumption is reasonably correct and suitable to produce models with a small variation of the density. Figure 4.12 presents the results from our calculations, which show a linear relationship between Q_0 and the density, ρ, of the models. This linear variation of Q_0 with ρ is not particularly unique to *a*-Si; a similar behavior has been observed experimentally by Inamura et al. [68, 67] for densified silica.

The results from Fig. 4.12 and the experimental data from Refs. [68] and [67] suggest that Q_0 can vary approximately linearly with the average density, ρ, of the models/samples. Since ρ is inversely proportional to the cubic power of the simulation cell size (L) for a given number of atoms, Q_0 also varies as $1/L^3$ when the density is varied by rescaling the volume. Thus, for homogeneous and isotropic models with no significant variation of the local density, which the WWW models satisfy in the absence of extended defects

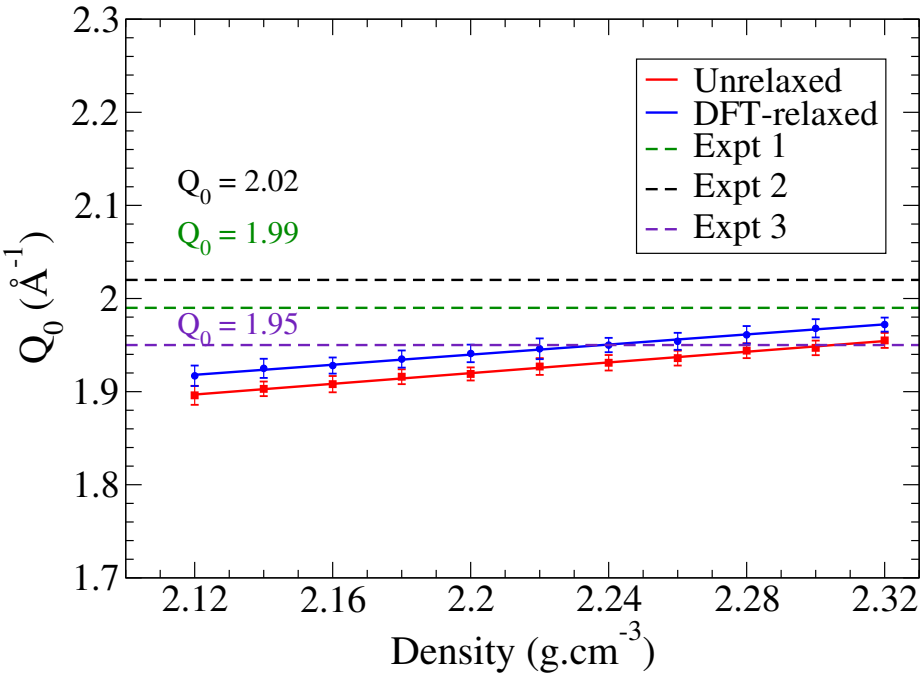

Figure 4.12: The variation of the peak position (Q_0) for 3000-atom models of *a*-Si with its mass density before (▪) and after (•) DFT relaxations. The value of Q_0 has been observed to vary linearly with the density of the model. The experimental values of Q_0 (horizontal dashed lines) correspond to as-implanted samples of density 2.28 g.cm^{-3} from Refs. [28] (black), [101] (green), and [29] (indigo).

and voids, it is reasonable to assume that $Q_0 \propto 1/r_{ij}^3$, where $r_{ij}(\rho)$ is the distance between any two atoms in the network, at sites i and j, of average density ρ. In view of our earlier observation that the position of the FSDP is largely determined by $F_2(Q)$(see Fig. 4.6), one may posit that r_{ij} values between R_2 and R_3 in $G(r)$ mostly affect the peak position at Q_0. These considerations lead to the suggestion that by substituting r_{ij}^3 by its average value of $\langle r_{ij}^3 \rangle = \langle R_2^3 \rangle$ for the atoms in the second radial shell, $Q_0 \langle R_2^3 \rangle$ should remain constant, on average, upon density variations via volume rescaling. Likewise, one can invoke the same reasoning and may expect $Q_0 \langle R_4^3 \rangle$ should be also constant but only approximately, due to the limited role and contribution of the atoms in the fourth radial shell in determining the position of Q_0.

The efficacy of our argument can be verified by results from direct numerical calculations. A plot of $Q_0 \langle R_2^3 \rangle$ (and $Q_0 \langle R_4^3 \rangle$) versus the average density ρ in Fig. 4.13 (and Fig. 4.14) indeed confirms our prediction. It may be noted that the observed (absolute) deviation, Δ, of $Q_0 \langle R_2^3 \rangle$ values in the density range 2.15–2.3 g.cm^{-3} in Fig. 4.13 is of the order of $\pm 0.46\,\sigma$, where σ is the (largest) standard deviation obtained by averaging results from 10 independent models for each density. By contrast, the corresponding deviation for $Q_0 \langle R_4^3 \rangle$ in

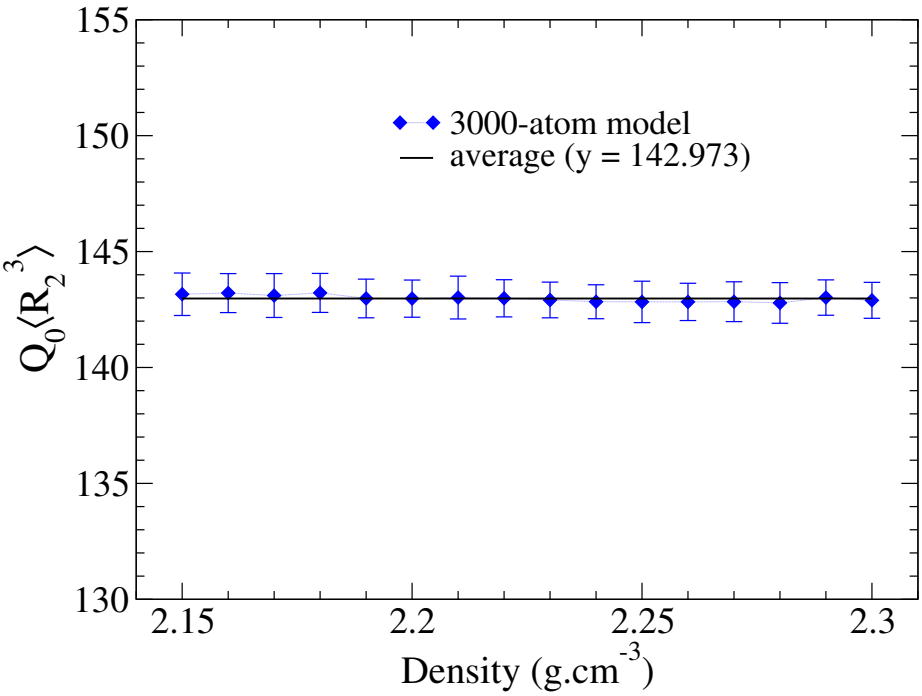

Figure 4.13: The relation between Q_0 and $\langle R_2^3\rangle$ of the atoms in the second radial shell. A constant value of $Q_0\langle R_2^3\rangle$ with respect to the density of a-Si models indicates that Q_0 is approximately proportional to the inverse of $\langle R_2^3\rangle$. The horizontal black line indicates the average value of $Q_0\langle R_2^3\rangle$ within the density range shown in the plot.

Fig. 4.14 is found to be more than two standard deviation, as indicated in the plot. The large deviation of $Q_0\langle R_4^3\rangle$ values is not unexpected in view of the small contribution of $F_4(Q)$ (to the FSDP) that originates from the fourth radial shell. Thus, the results from Fig. 4.13 lead to the conclusion that Q_0 is approximately proportional to the inverse of the average cubic power of the radial distance, $\langle R_2^3\rangle$, of the atoms in the second radial shell in a-Si. It goes without saying that the use of $\langle R_2\rangle^3$, instead of $\langle R_2^3\rangle$, does not change the conclusion of our work, as the difference between these two values is found to be about 1.92–2.1 Å^3, for the mass density in the range of 2.15 to 2.3 g.cm^{-3}, which simply shifts the plot (in Fig. 4.13) vertically downward by a constant amount.

We end this section by making a comment on the possible role of distant radial atomic correlations, or extended-range oscillations (ERO), in $G(r)$ on the FSDP, based on our preliminary results from 6000-atom models. Although the presence of ERO in ultra-large models of a-Si beyond 15 Å is an undisputed fact [100], a direct determination of the effect of the ERO on the FSDP in a-Si is highly nontrivial due to the presence of intrinsic noises in $G(r)$ at large radial distances. Numerical calculations using 6000-atom models of a-Si indicate that only a minute fraction of the total intensity of the FSDP results from the radial

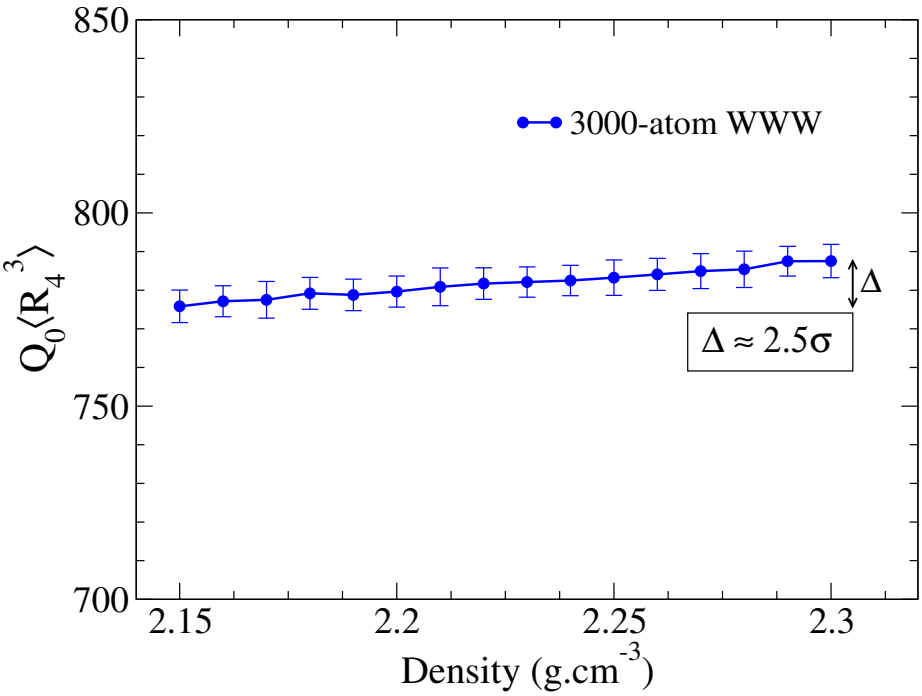

Figure 4.14: The dependence of Q_0 and $\langle R_4^3 \rangle$ for the atoms in the fourth radial shell of *a*-Si in the density range from 2.15 to 2.3 g.cm^{-3}. The large deviation of $Q_0\langle R_4^3\rangle$ values, indicated by $\Delta \approx 2.5\,\sigma$, from a constant value suggests that no simple relationship between Q_0 and $\langle R_4^3 \rangle$ exists.

region beyond 15 Å. These calculations do not include any possible artifacts that may arise from the noises in $G(r)$ at large distances. The observed deviation in the peak intensity, due to the truncation of the radial distance at 15 Å and at higher values, is found to be about 1–2%, which is less than one standard deviation (σ) associated with $S(Q_0)$, obtained from using the maximal radial cutoff distance $R_c(= L/2)$, as far as the results from 6000-atom models are concerned. Figure 4.15 shows the variation of the intensity near the FSDP for five different cutoff values from 15 Å to 18 Å and 24.85 Å. It is apparent that the changes in $S(Q)$ near Q_0 are very small as the radial cutoff value increases from 15 Å to 18 Å. These small changes in the intensity values are readily reflected in Fig. 4.16, where the fractional errors associated with the calculation of $S(Q, r_i)$ are plotted against Q for r_i = 15 Å to 18 Å. Thus, as far as the present study and the maximum size of the models are concerned, the ERO do not appear to contribute much to the FSDP. However, an accurate study of the ERO in *a*-Si would require high-quality ultra-large models, consisting of several tens of thousands of atoms, and a suitable prescription to handle noises in $G(r)$ at large distances. These and some related issues concerning the origin of the ERO in *a*-Si and their possible role in $S(Q)$ will be addressed in a future communication.

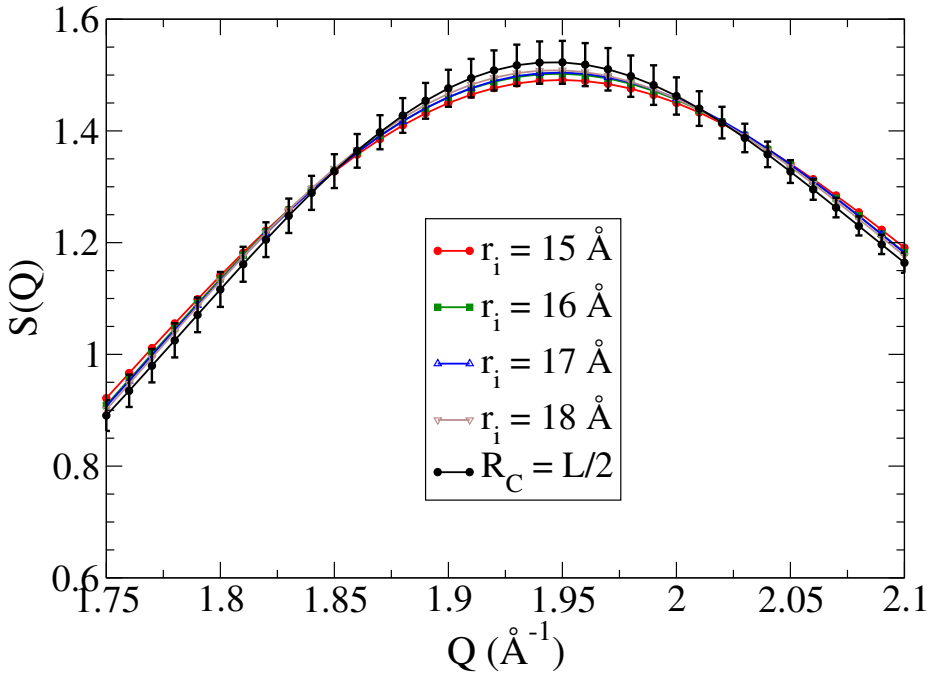

Figure 4.15: The structure factor, $S(Q)$, in the vicinity of the FSDP from 6000-atom a-Si models. The change in $S(Q)$ due to varying radial cutoff distances, r_i, is found to be less than one standard deviation ($\Delta S(Q_0) \approx 0.85\,\sigma$ for r_i = 15 Å, and $0.46\,\sigma$ for r_i = 18 Å). The standard deviation, σ, is obtained from using the maximal radial cutoff $L/2$, which is given by 24.85 Å. The results correspond to the average values of $S(Q)$ obtained from 10 configurations.

4.4 Conclusions

In this chapter, we have studied the origin and structure of the FSDP of a-Si with an emphasis on the position, intensity, and width of the diffraction peak. The study leads to the following results: 1) By partitioning the contribution of the reduced PCF to the FSDP, which originates from the Fourier transform of radial atomic correlations in the real space, a quantitative measure of the contribution to the FSDP from different radial shells is obtained. The results show that the position of the FSDP in a-Si is principally determined by atomic pair correlations in the second, fourth, and sixth radial shells, in the descending order of importance, supplemented by small residual contributions from beyond the sixth radial shell; 2) A convergence study of the position, intensity, and width of the FSDP, using a set of models of size from 216 to 6000 atoms, suggests that the minimum size of the models must be at least 1000 atoms or more in order for the results to be free from finite-size effects. This approximately translates into a radial length of 14 Å, which is consistent with the results obtained from the radial-shell analysis of the reduced PCF; 3) A theoretical basis for the

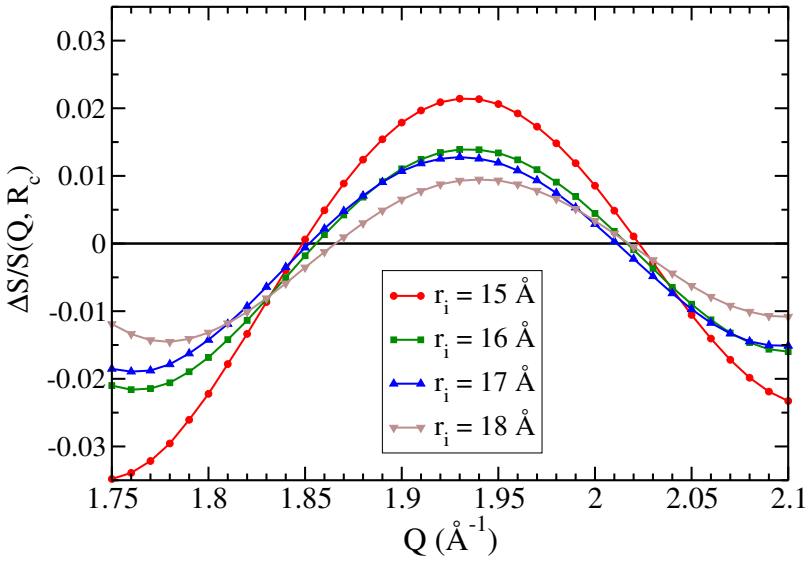

Figure 4.16: The fractional error associated with the calculation of the structure factor in the vicinity of the FSDP with a varying radial cutoff distance, r_i, from 15 Å to 18 Å. $\Delta S(Q)$ is the absolute error and R_c (=24.85 Å) is the half-length of the cubic simulation cell for 6000-atom models. The error due to the truncation of the radial distance at r_i can be seen to be around 1–2%, which is well within one standard deviation of $S(Q_0)$ (see Fig. 4.15).

results obtained from numerical calculations is presented by examining the relationship between the peaks in the structure factor and the reduced PCF. Contrary to the common assumption that the peaks in the structure factor and the reduced PCF are not directly related to each other, we have shown explicitly that the knowledge of the reduced PCF alone is sufficient not only to determine the approximate position of the FSDP and the principal peak but also the relevant radial regions that are primarily responsible for the emergence of these peaks in the structure factor, and vice versa; 4) The study leads to an approximate relation between the position of the FSDP and the average radial distance of the atoms in the second radial shell of *a*-Si networks. For homogeneous and isotropic models of *a*-Si with no significant variation of the local density, it has been shown that the position of the FSDP is inversely proportional to the cubic power of the average radial distance of the atoms in the second radial shell. The result is justified by providing a phenomenological explanation – based on experimental and computational studies of the variation of the FSDP with the average density of *a*-Si samples and models – which is subsequently confirmed by direct numerical calculations for a range of density from 2.15 to 2.3 g.cm^{-3}.

Chapter 5

RADIAL SHELL CORRELATIONS AND FIRST SHARP DIFFRACTION PEAK OF AMORPHOUS SILICA

5.1 Introduction

Amorphous silica, a-SiO_2, is one of the extensively studied covalent material in solid state physics. Many experimental [165, 166, 167] and theoretical studies [61, 168, 169] have shown that the first sharp diffraction peak (FSDP) of a-SiO_2 appears at the low wavevector region near 1–1.5 $Å^{-1}$ of the structure factor of a-SiO_2. Origin of the FSDP of a-SiO_2 is primarily due to medium-range orders such as ordering of the interstitial voids around the network-forming cations [61] and crystalline layers or quasilattice planes [58].

The first sharp diffraction peak of a-SiO_2 depends on the radial correlations of medium-range order [168]. In an atom-void cluster model of a-SiO_2, Elliott (1991) has indicated the origin of FSDP is due to the low atomic occupancy zones in cluster networks [61]. On the other hand, the partial structure factor obtained from density-density or charge-charge correlations shows the FSDP of a-SiO_2 has significant contribution from the chemical ordering on the amorphous network of atoms extended up to 4-8 Å, with a negligible contribution of the radial correlations beyond 8 Å [168]. Which is identical as in a-$GeSe_2$ and a-$SiSe_2$ glasses [107], even though connectivity of those glasses is different as compared to a-SiO_2. In oxides and chalcogenide glasses the FSDP arises as a prepeak of concentration-concentration structure factor [170].

Significant variation on the position and intensity of the FSDP of a-SiO_2 with mass density have been observed in diffraction experiments [166, 149]. The position of the FSDP shifted towards the larger-Q region and intensity/height of the FSDP decreased with incresing mass density. In silica glass, densification shows no changes in the short-range order of the system. Even though densification can lower the Si-Si and O-O bond-length, densification cause nearly negligible change in Si-O bond-length with nearly no changes in the short-range order of the system, which indicates FSDP as the feature arises due to the intermediate-range orders [149]. The decrease in Si-O-Si bond-angles changes real-space structure ordering that shifted FSDP at the larger-Q region [166, 149], however the changes are inconsistent with elastic compression of silica glass [166].

Uchino *et al.* (2005), in a real-reciprocal space analysis of silica using continuous wavelet transform technique, have shown the dominant correlation on the FSDP of silica is associated with second-neighbor correlations, such as Si-O-Si-O-Si and O-Si-O-Si-O extended up to 5 Å [171]. The Si-Si, O-O, and Si-O correlations all contribute on the FSDP of a-SiO_2, an anti-correlation from Si-O is inevitable on the diffraction peak at the vicinity of 3 $Å^{-1}$ [169].

In this chapter, we have analyzed the origin of the FSDP of a-SiO_2 using real-space radial correlations from different radial shells. Rest of the chapter is aligned as follows, in section 5.2, the methods implemented in model generation and calculation of the reduced scattering intensity, F(Q), of a-SiO_2 are presented in brief. Contribution of the radial shell correlations on the FSDP of a-SiO_2, including those for the partial reduced scattring intensity, are discussed in section 5.3. The relevent conclusions thereafter are stated in section 5.4.

5.2 Computational Methods

The atomistic model of a-SiO_2 is generated using decorated and relax method [172] from a 216-atom supercell of a-Si with four-fold coordination and no defects, as a starting point. Amorphous silica consist of tightly centered bond angles at the tetrahedral angle. Later, bond-center VI (Si) is added to all IV-IV (O-O) bonds and the coordinates are adjusted to match the experimental density of a-SiO_2 about 2.20 $g.cm^{-3}$. [173] The final configuration is then relaxed using the first-principles density functional code SIESTA [159], for full self-consistent-field calculation using generalized-gradient approximation [86] and a set of double-zeta basis functions.

For an isotropic binary system with N atoms, the reduced scattering intensity factor [87] is given as,

$$F(Q) = Q\Big[\frac{\frac{I}{N} - \langle f^2\rangle}{\langle f\rangle^2}\Big] = \frac{Q}{\langle f\rangle^2}\Big[\sum_{ij} x_i x_j f_i f_j \left(I_{ij} - 1\right)\Big]$$

$$F(Q) = Q\Big[\frac{f_1^2}{\langle f\rangle^2} x_1^2 \left(I_{11} - 1\right) + \frac{f_2^2}{\langle f\rangle^2} x_2^2 \left(I_{22} - 1\right) + \frac{2 f_1 f_2 x_1 x_2}{\langle f\rangle^2} \left(I_{12} - 1\right)\Big] \tag{5.1}$$

I_{ij} is the partial interference function, given as,

$$I_{ij} = 1 + \frac{4\pi\rho_0}{Q}\int_0^\infty r\left[g_{ij}(r) - 1\right]\sin\left(Qr\right)dr \tag{5.2}$$

where $g_{ij}(r) = \frac{\rho_{ij}(r)}{\rho_0 x_j}$, $\rho_{ij}(r)$ is the average number density of type j atoms at distance r from type i, and $\rho_0 = \frac{N}{V}$ the number density of the system. The structure factor, S(Q), in terms of F(Q), is hence,

$$S(Q) = 1 + \frac{F(Q)}{Q} \tag{5.3}$$

For actual calculation the upper limit of the integeral in Eq. 5.2 is trancated to the radial cut off, R_c, half of the box length of the cubic simulation cell.

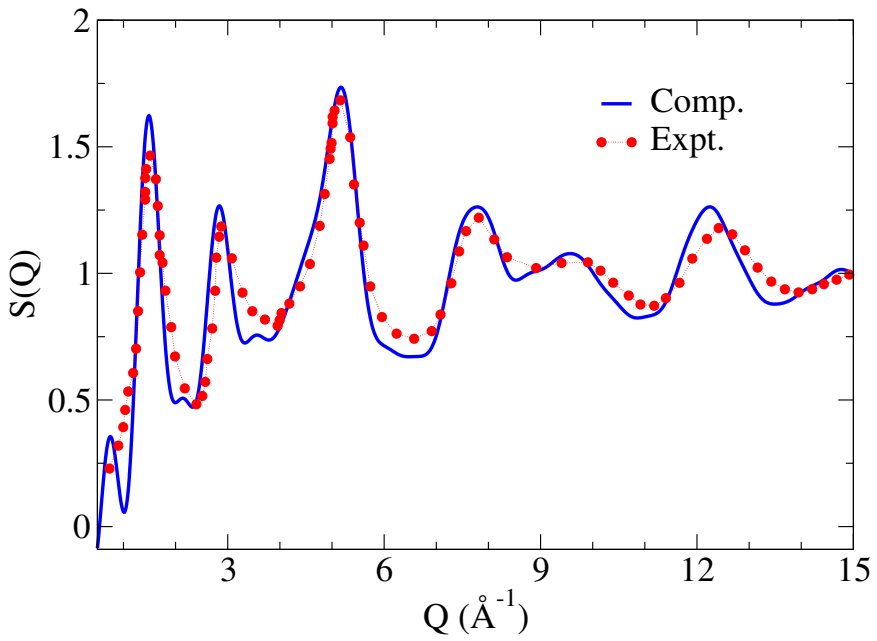

Figure 5.1: The total neutron structure factor of a-SiO_2 from simulation (blue line). The experimental S(Q) of v-SiO_2 by Susman *et al.* [149] is given for comparison (red dots).

5.3 Results and Discussion

Figure 5.1 shows the total neutron structure factor, S(Q), of a-SiO_2 consist of 648 (216 Si and 432 O) atoms, calculated using Eq. 5.3 in Faber-Ziman approach [174] compared with S(Q) of v-SiO_2 obtained from neutron diffraction experiment [149]. Including the diffraction peaks at the larger Q region, which are associated with the short-range correlations in SiO_4 tetrahedral units, the FSDP from simulation shows good agreement with the result from neutron diffraction experiment at room temperature. The position of the FSDP of a-SiO_2 is observed near 1.5 Å^{-1}, within the Q-range, 1- 2 Å^{-1}, suggested in diffraction experiments [165, 166] and molecular dynamic simulations [61, 169]. The bond angle distribution for O-Si-O and Si-O-Si bonds are represnted in figure 5.2. The model implemented here shows the average bond angle for O-Si-O and Si-O-Si bonds are $109.5^\circ \pm 3.5^\circ$ and $141.5^\circ \pm 12.5^\circ$, close to the experimental results, 109° and 144-152°, respectively. [175, 176]

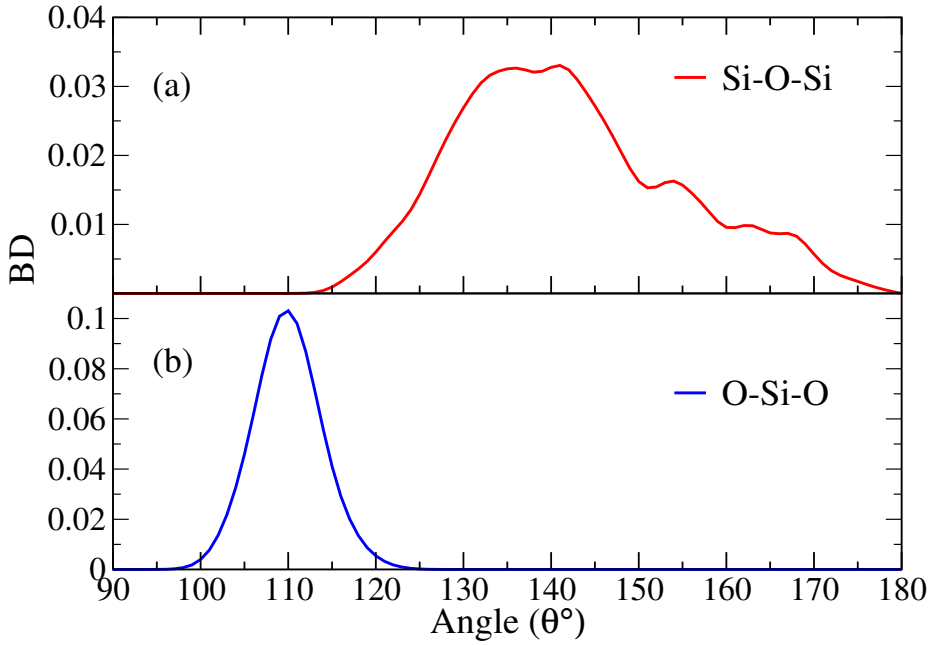

Figure 5.2: The Si-O-Si (top) and O-Si-O (bottom) bond angle distribution of *a*-SiO_2. The average bond angle for Si-O-Si and O-Si-O bonds are found to be 141.5° and 109.5°, respectively.

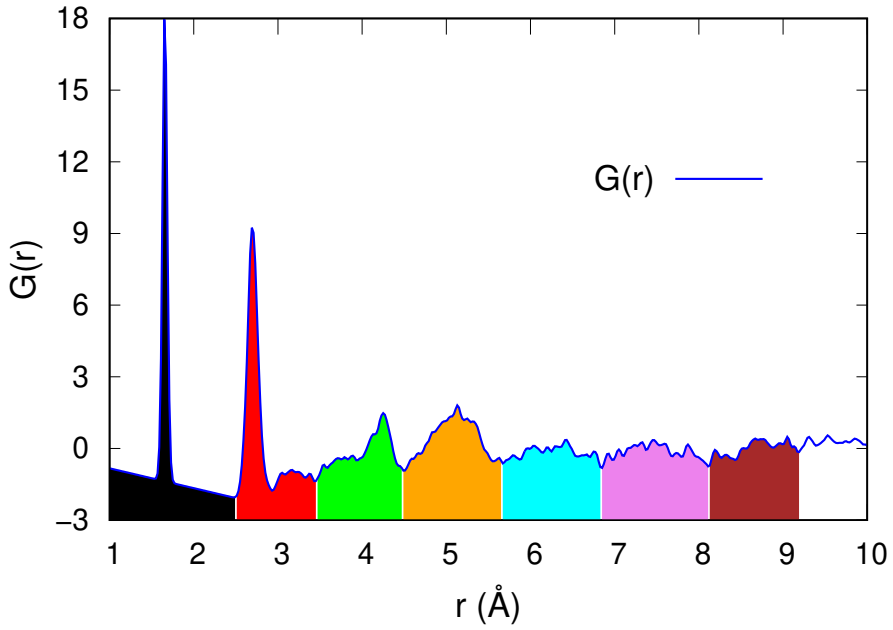

Figure 5.3: The reduced pair-correlation function, G(r), of *a*-SiO_2 extended up to 10 Å. The first seven distinct radial shells are highlighted with different colors.

5.3.1 Radial shell analysis of the reduced scattering intensity (F(Q))

Figure 5.3 shows the reduced PCF, G(r), of *a*-SiO_2, the distinct radial shells, extended up to ≈ 10 Å, are highlighted with different colors. The reduced scattering intensity for an

isotropic binary system is given as,

$$F(Q) = \int_0^\infty G(r)\,\sin(Qr)\,dr$$

where, $G(r)(=4\pi r\rho_0[g(r)-1])$ is the reduced pair correlation function. For the contribution of real space correlations arises from different radial shells to the FSDP of the reduced scattering intensity factor, Eq 5.4 is further defined as,

$$F(Q) = \sum_{i=1}^{n} F_i(Q;R_i,R_{i+1})$$

where,

$$F_i(Q;R_i,R_{i+1}) = \int_{R_i}^{R_{i+1}} G(r)\,\sin(Qr)\,dr.$$

is the contribution to $F(Q)$ from a radial shell at between R_i and R_{i+1}. For clarity, the term F(Q) used in this chapter differs with the similar notation used in monoatomic system as discussed in the previous chapter.

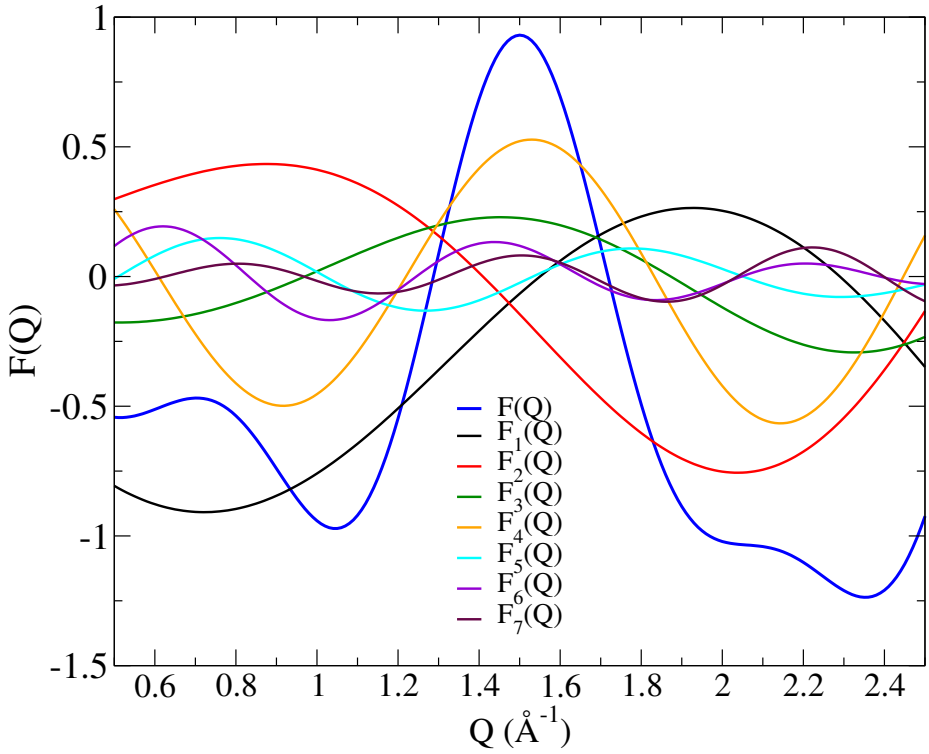

Figure 5.4: Contribution to the FSDP of a-SiO_2 from different radial shells, colors used for the plots are consistent with the colors of the corresponding radial shells presented in Fig. 5.3.

The contribution of the real-space correlations from the different radial shells to the FSDP of a-SiO_2 near the vicinity of 1.5 $Å^{-1}$ is given in Fig. 5.4. The majority of structure

of the FSDP is coming from the third and fourth radial shell extended between 3-6 Å. Some minimal positive contribution is from the sixth and seventh shell. The impact of radial shell correlations on the FSDP indicates the radial correlations of 3-6 Å play a vital role in the origin of the FSDP, when entire radial correlations are considered.

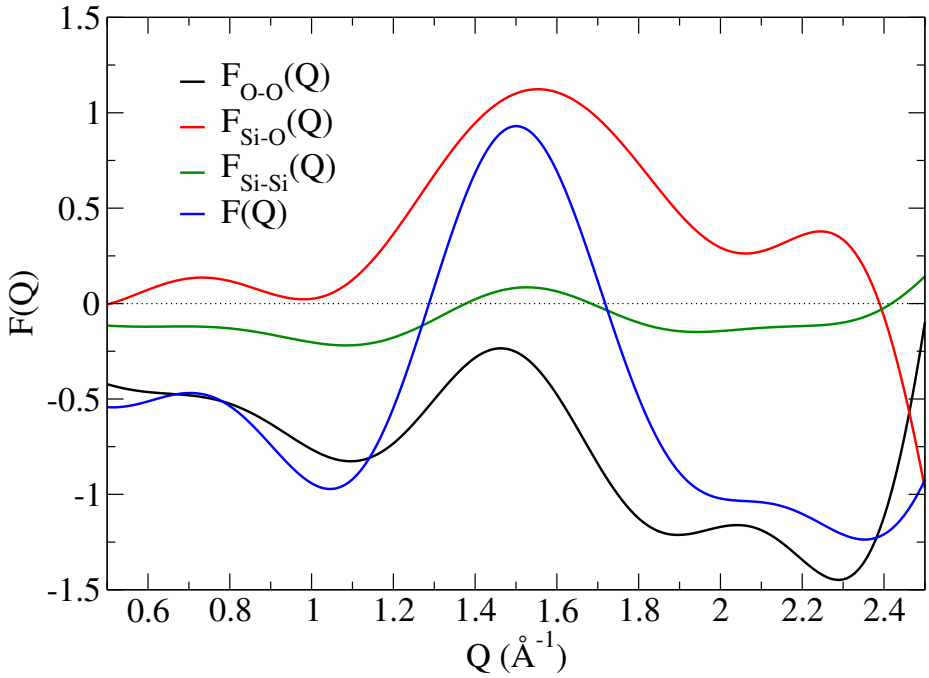

Figure 5.5: The reduced scattering intensity, F(Q), of a-SiO_2 at the vicinity of the FSDP (blue), the contribution from Si-Si (green), Si-O (red), and O-O (black) correlations, in terms of the (weighted) partial reduced scattering intensity, $F_{\alpha\beta}(Q)$, are compared for their contribution to the FSDP.

A comparison of the FSDP of a-SiO_2 with the weighted partial reduced scattering intensities due to atomic correlations of types Si-Si, Si-O, and O-O is presented in Fig. 5.5. At the vacinity of the FSDP, a majority of structure of the FSDP appears from Si-O and O-O correlations with minimal background contribution from Si-Si correlations, consistent with the diffraction pattern observed via neutron scattring experiments. [169]

Till now, from the radial shell analysis of the FSDP, contribution of third and fourth radial shells or the Si-O and O-O correlations is observed inevitebal to the FSDP of a-SiO_2. To understand the role of the real-space correlation on the origin of the FSDP, a comparison of the partial atomic pair-correlation functions is given in Fig. 5.6. Figure 5.6 reveals the impact of O-O-O and Si-O-Si correlations on the structure of the FSDP. In countary to the oxides and chalcogenide glasses, Si-Si correlations plays minimal role in the origin of the FSDP of a-SiO_2.

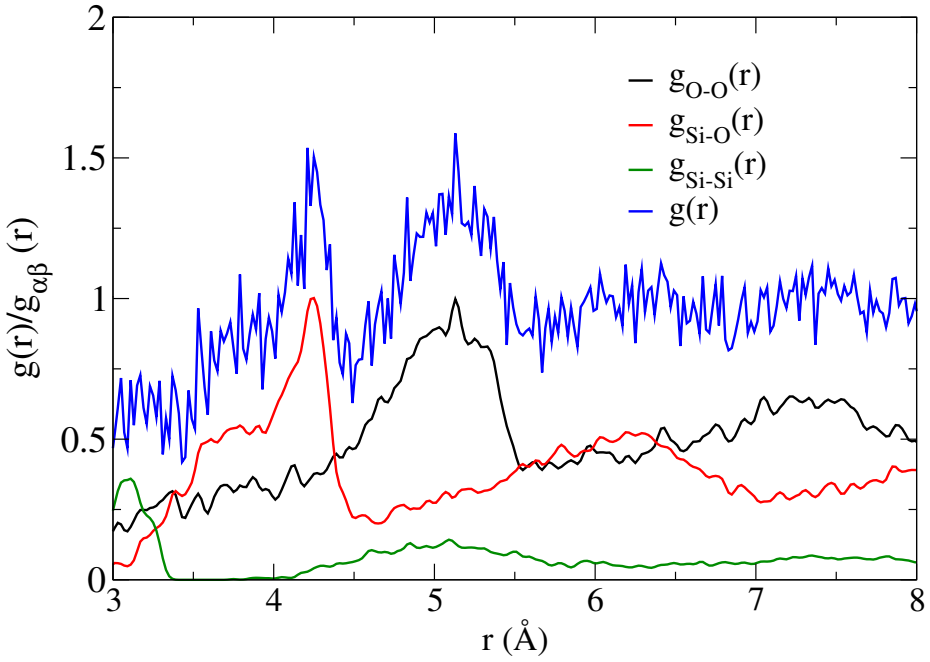

Figure 5.6: Contribution of the partial atomic pair-correlations on the total atomic pair-correlation, g(r), of a-SiO_2 (blue). The Si-Si (green), Si-O (red), and O-O (black) pair correlations are presented within 3-8 Å radial length scale.

5.3.2 Real space contribution to the partial reduced scattering intensity factors

The partial reduced scatering intensity, $F_{\alpha\beta}(Q)$; $\alpha,\beta = Si,O$, are analyzed based on the partial real space correlations obtained from the radial shells on the corresponding partial pair-correlation function, $G_{\alpha\beta}(r)$. The total $F_{\alpha\beta}(Q)$ is given as,

$$F_{\alpha\beta}(Q) = \sum_j F^j_{\alpha\beta}(Q;R^j_{\alpha\beta},R^{j+1}_{\alpha\beta})$$

where,

$$F^j_{\alpha\beta}(Q;R^j_{\alpha\beta},R^{j+1}_{\alpha\beta}) = \int_{R^j_{\alpha\beta}}^{R^{j+1}_{\alpha\beta}} G_{\alpha\beta}(r)\,\sin(Qr)\,dr.$$

where, $R^j_{\alpha\beta}$ and $R^{j+1}_{\alpha\beta}$ representes the lower and higher end of the j^{th} radial shell.

Figures 5.7- 5.9, represent the partial correlations, $G_{\alpha\beta}(r)$, separated in to diffrenet radial shells, with corresponding partial reduced scattering intensity, $F_{\alpha\beta}(Q)$, and the contribution of each radial shell of $G_{\alpha\beta}(r)$ to the $F_{\alpha\beta}(Q)$ at the vicinity of the FSDP of a-SiO_2. The major contribution to the FSDP of a-SiO_2, as observed in Fig. 5.5 is from the Si-O correlations. Later, we analyzed the contribution of the radail shells of $G_{O\text{-}O}(r)$ to the $F_{O\text{-}O}(Q)$. as presented in Fig. 5.7. The second and fourth radial shell of $G_{O\text{-}O}(r)$ play constructive role to the first diffraction peak of the $F_{O\text{-}O}(Q)$. On the other hand, major role on the $F_{Si\text{-}O}(Q)$ is

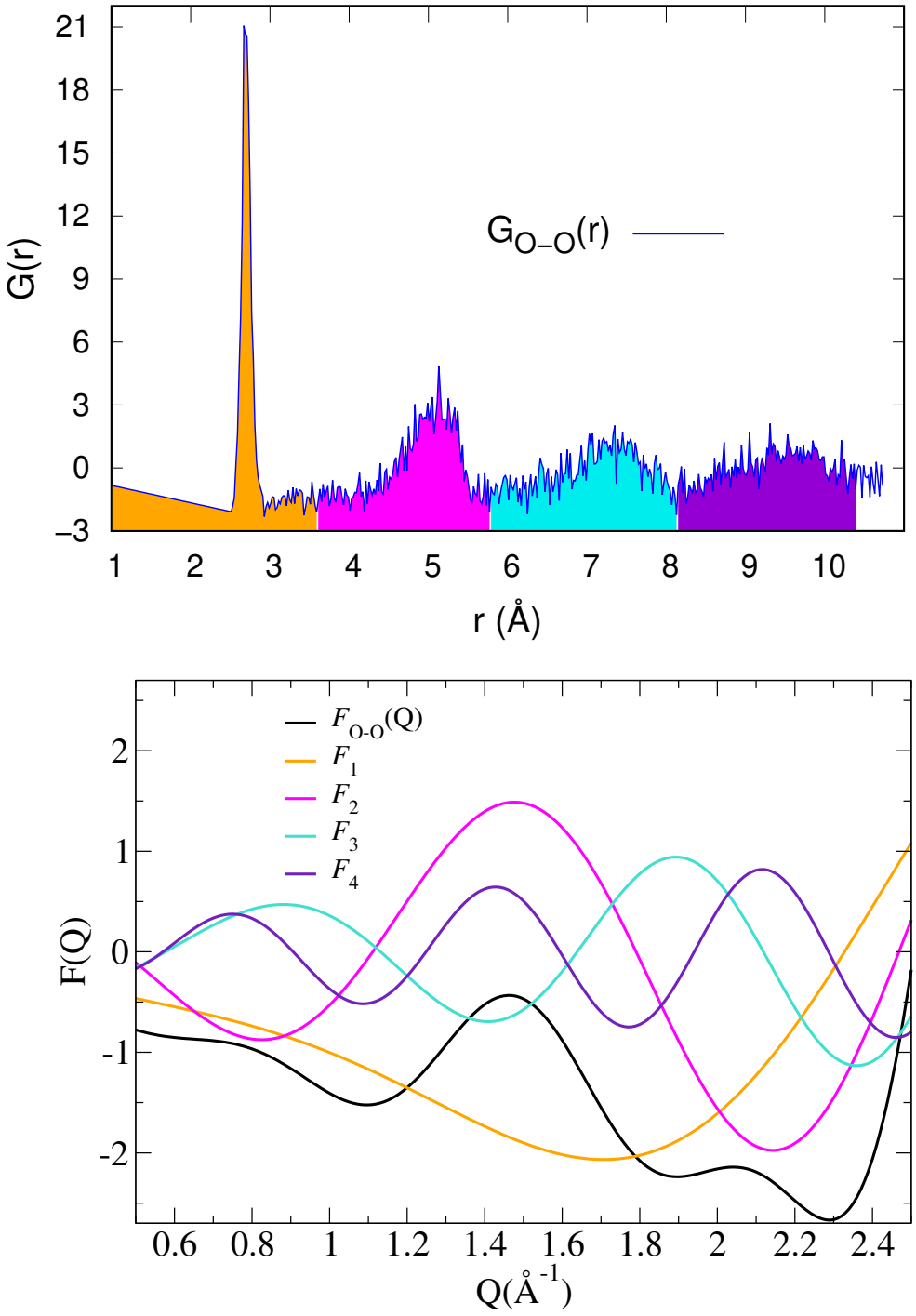

Figure 5.7: The radial shells in the partial reduced pair-correlation function $G_{\text{O-O}}(r)$(upper plot) and the radial shell contribution to the partial reduced intensity factor, $F_{\text{O-O}}(Q)$, (lower plot) at the vicinity of the FSDP.

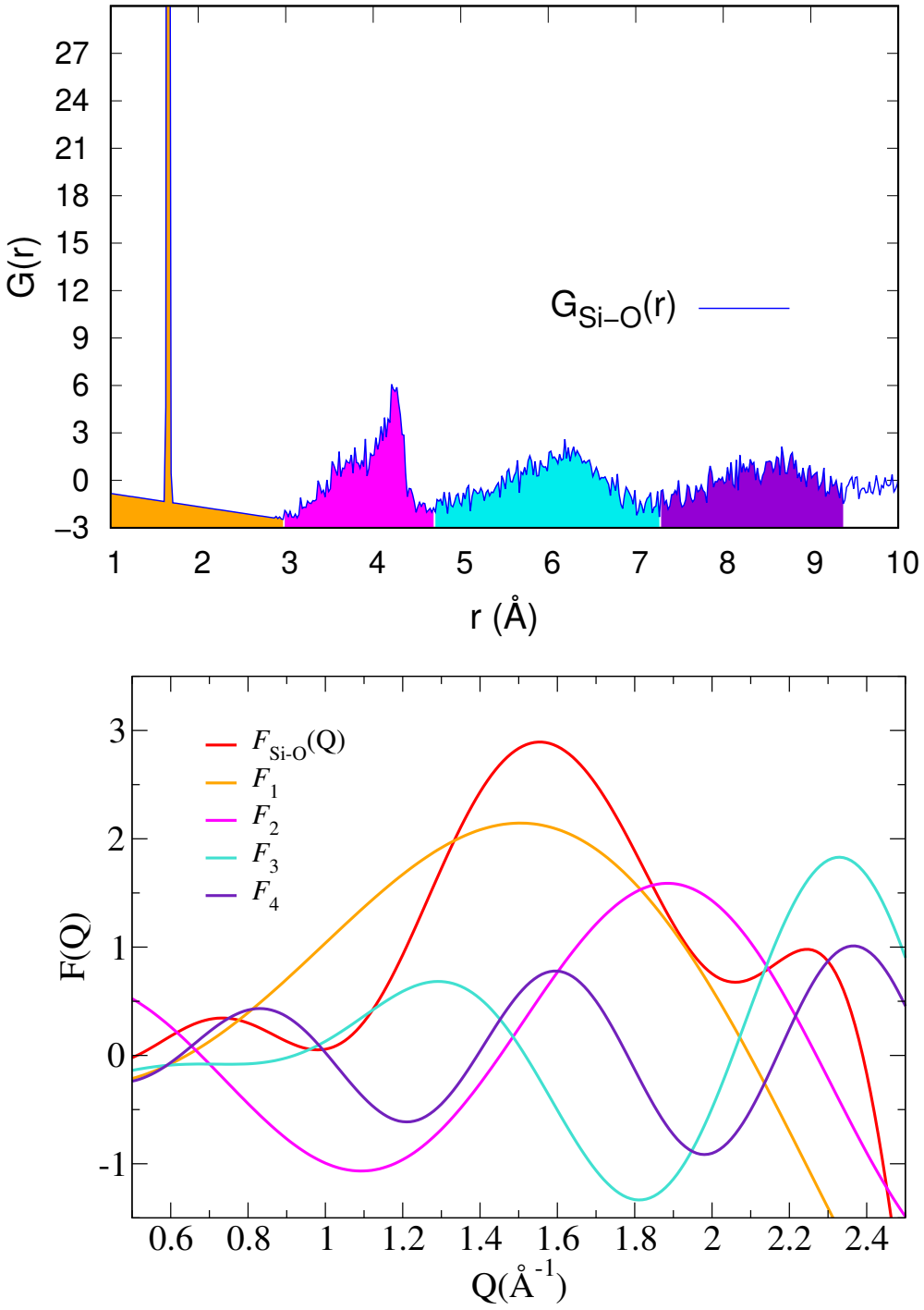

Figure 5.8: (Top) Distinct radial shells separated on the basis of peak positions on the reduced pair-correlation function $G_{\text{Si-O}}(r)$, and (bottom) contribution of the radial correlations on the partial reduced scattering intensity $F_{\text{Si-O}}(Q)$.

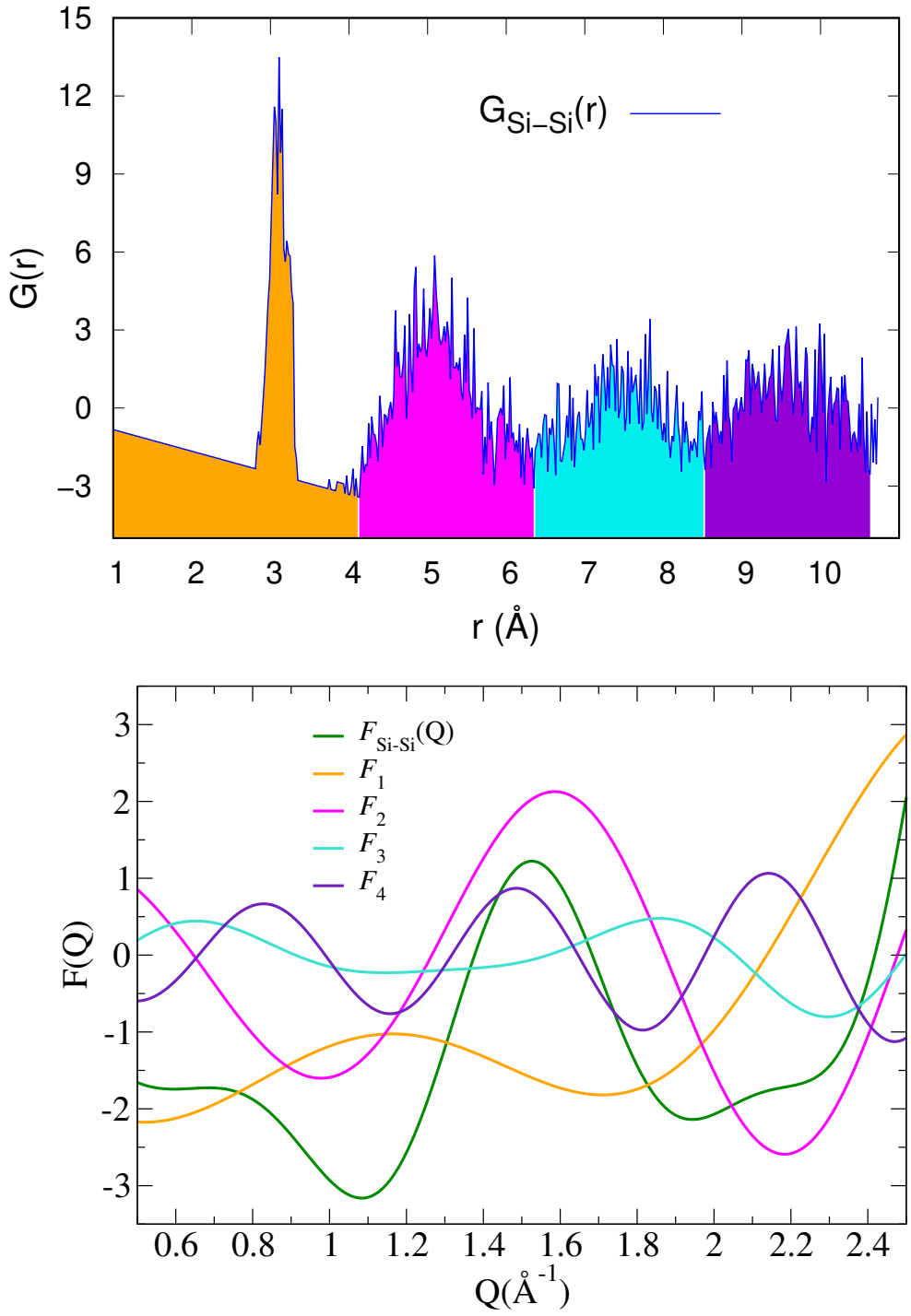

Figure 5.9: Distinct radial shells of $G_{\text{Si-Si}}(r)$ (above) and the contribution to the FSDP of $F_{\text{Si-Si}}(Q)$ arises from the corresponding radial shells (below).

obtained from the first radial shell, as shown in Fig. 5.8. Likewise, the second and fourth shell contributed must of the structure of the $F_{\text{Si-Si}}(Q)$, as given in Fig. 5.9.

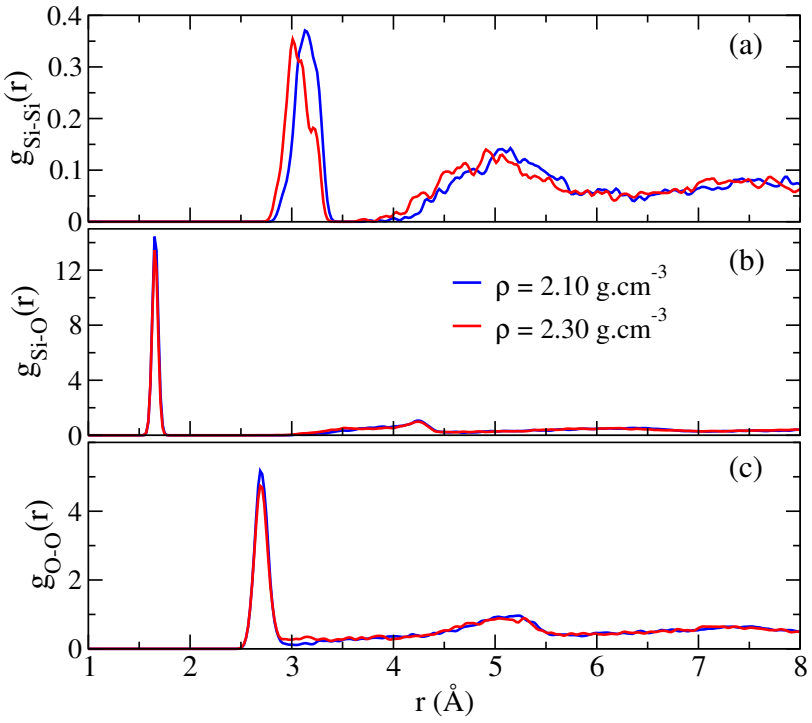

Figure 5.10: The partial PCF $g_{\alpha\beta}(r)$ obtained from a-SiO_2 system of density 2.10 $g.cm^{-3}$ (blue) and 2.30 $g.cm^{-3}$ (red), respectively

After analyzing the impact of the real-space correlations arises from different radial shells of the total or partial pair correlation function, it is apparent to that the real-space correlations extended up to 8-10 Å have their role on the existance of the FSDP in wave-vector space structure of a-SiO_2, the correlations related with MROs in the amorphous network of a-SiO_2.

5.3.3 Variation of the FSDP with density

The variation of the position and intensity of the FSDP of a-SiO_2 with mass density is presented in figure 5.12. Figure 5.12 suggests that the position of the FSDP increases approximately linearly with the mass density. A rapid decrease on the intensity, $S(Q_0)$, of the FSDP is oserved at higher density The structural difference between the silica models at 2.10 $g.cm^{-3}$ and 2.30 $g.cm^{-3}$ are given in figure 5.10 and figure 5.11. Figure 5.10 represents the partial pair correlation function of a-SiO_2 at densities 2.10 $g.cm^{-3}$ and 2.30 $g.cm^{-3}$, respectively. Minimal changes are observed in the atomic correlations with density, depending on the connectivity of the atom-atom types. The reduced scattering intensity at two different densities, are shown in Fig. 5.11. Except for $F_{\text{O-O}}(Q)$, position of the first peak in partial reduced scattering intensity is observed shifted towards the higher Q region where

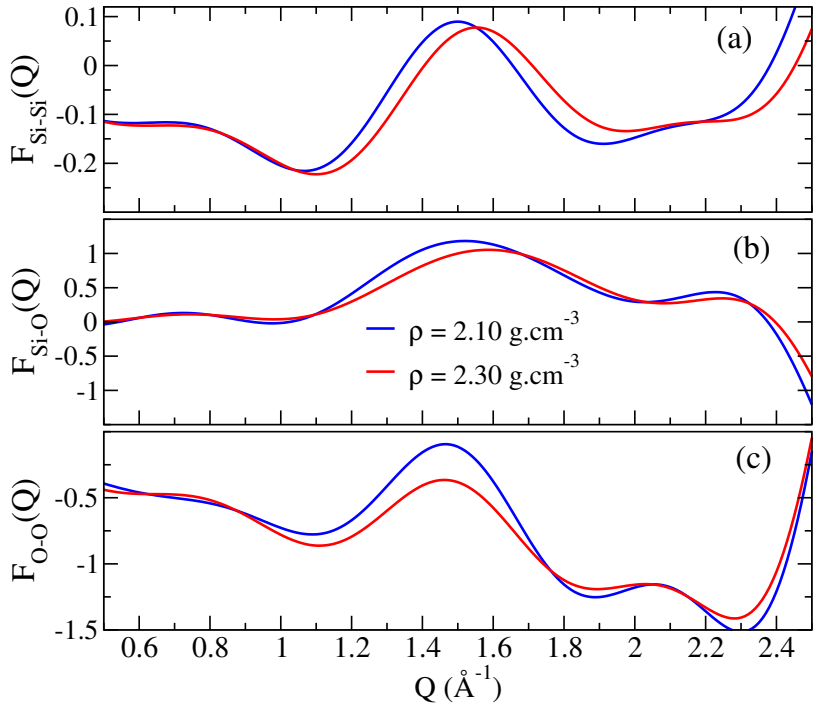

Figure 5.11: The partial reduced scattering intensity $F_{\alpha\beta}(Q)$ of a-SiO_2 of density 2.10 $g.cm^{-3}$ (blue) and 2.30 $g.cm^{-3}$ (red), respectively

minimal change in the intensity of the diffraction peak is obtained. The structural ordering at the medium-range length scale can vary with density of a amorphous system as change in bond angles or connectivity of the atoms occur. [177] Increasing density of a silica glass introduces 5 and 6 folds in Si-O coordinations [178] which reduce the Si-Si and O-O bond length, as a consequence of which the position of the FSDP shifted towards the higher Q region. [178]

5.4 Conclusion

A through analysis of the first sharp diffraction peak of the reduced scattering intensity, $F(Q)$, of a-SiO_2 in atomic point of view, using computer simulated model of 648 atoms, at density of 2.20 $g.cm^{-3}$, is presented in this study. The real space information obtained from the diffrent radial shells, characterized by distinct correlations, are analyzed for their impact on the FSDP of a-SiO_2 at the vicinity of 1.5 Å^{-1}. The major contribution to the FSDP of a-SiO_2 is observed coming of the radial correlations of the third and fourth radial shell of the reduced pair correlation function, located between 3-10 Å radial length. The impact of the real-space correlations is further varified from similar analysis of the partial reduced scattering intensity factor. Comparison of the partial reduced scattering intensity due to Si-O,

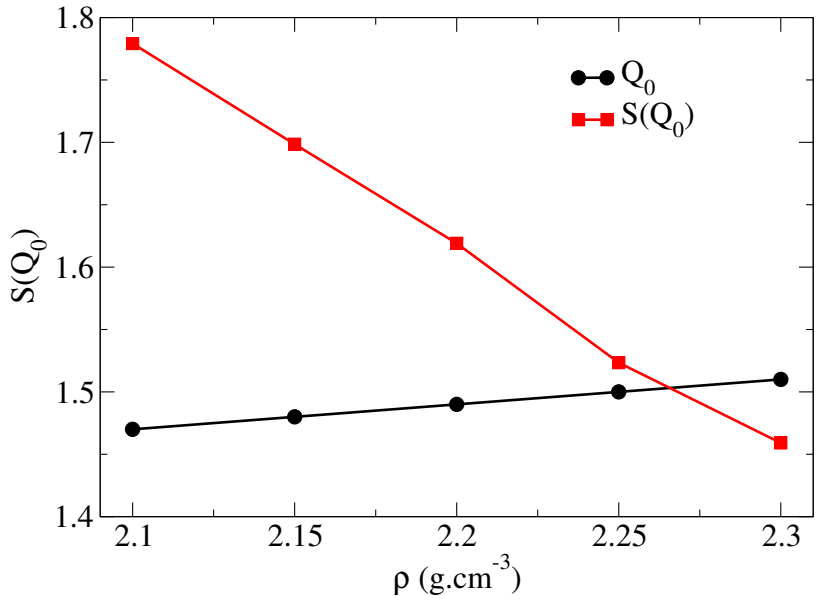

Figure 5.12: Variation on the position, Q_0, and intensity, $S(Q_0)$, of structure factor, S(Q), of *a*-SiO_2 with density.

O-O, and Si-Si correlations indicated Si-O and O-O correlations have significant impact on the FSDP of *a*-SiO_2, with minimal contribution from Si-Si correlations. As reported in the previous literature, the radial correlations beyond the SRO are observed having their role in the origin and structure of the FSDP of *a*-SiO_2.

Also, within the range of the density considered in this study, intensity of the FSDP is found rapidly decreses with mass density. In opposite, the position of the FSDP shifted towards the higher Q-region, as a consequences of the rearrangment of the atoms beyound SRO. However, the observation made in this study are not completely noval, we have presented a detail study based on the radial shell analysis approach to reveal the role of the real-space correlations arises from some discrete radial shells to the origin of the FSDP of *a*-SiO_2, a binary covalent solid.

Chapter 6

DEBYE-WALLER FACTOR AND DYNAMICAL PROPERTIES OF AMORPHOUS SILICON

6.1 Introduction

The influence of thermal vibrations on the intensity of diffraction maxima in crystals has been extensively studied in the literature [151, 179, 180, 181, 182]. Following Debye's original work [151], where vibrations in crystals were assumed to be independent of the position of atoms in a lattice, more accurate calculations by Faxén [179] and Waller [180] showed that thermal vibrations reduce the intensity of the diffraction maxima but do not affect the sharpness of the diffraction lines. The missing intensity from the spectra was found to be present in the general background, which is known as the temperature diffuse scattering (TDS). The intensity reduction factor, e^{-2M}, is known as the Debye-Waller factor [183], where $M = 8\pi^2\langle u^2\rangle \sin^2\theta/\lambda^2$ for elemental solids. The mean-square displacement (MSD) of atoms, $\langle u^2\rangle$, along a direction $\mathbf{Q}$, is perpendicular to the reflecting plane and θ is the glancing angle of incidence with the plane. The vector $\mathbf{Q}$ is given by $(\mathbf{k}-\mathbf{k}_0)$, where $\mathbf{k}$ and $\mathbf{k}_0$ are the wavevectors for the scattered and incident beams, respectively. In Bragg geometry, the scattering angle 2θ is given by the angle between $\mathbf{k}$ and $\mathbf{k}_0$, and $|\mathbf{k}| = |\mathbf{k}_0|$ for elastic scattering with $|\mathbf{Q}| = 2|\mathbf{k}|\sin\theta = 4\pi\sin\theta/\lambda$, where λ is the wavelength of the scattering radiation.

The relationship between the Debye-Waller factor and finite-temperature atomic vibrations in solids was extensively studied in the last century [151, 179, 180, 181, 182, 184, 185, 186, 187, 188, 150]. However, the great majority of these studies are primarily focused on elemental and molecular *crystals* using a variety of theoretical methods. Among these methods, the so-called statistical-moment approach [189], Green function techniques [184, 185], and lattice-dynamical calculations, employing valence force fields, shell models, and adiabatic bond-charge models [186, 187], are particularly noteworthy. In recent years, the calculation of the Debye-Waller factor of crystalline materials has been addressed by using total-energy and forces from density-functional theory (DFT) [190, 188, 150]. By contrast, there exist only few studies that address the effect of the Debye-Waller factor in the amorphous state, e.g. As, SiO_2 and InP [191, 192, 193]. Unlike monoatomic crystals, the MSD of an atom in an amorphous solid varies from site to site and depends on the local topology of the network.

As a result, the MSD of amorphous solids can significantly depend on the structural quality of the models employed in the calculations. It is therefore absolutely necessary to compute the Debye-Waller factor using high-quality structural models of amorphous solids obtained from density-functional calculations.

The absence of translational symmetry in amorphous solids means that the normal modes and frequencies of vibrations have to be determined in the coordinate space by computing the environment-dependent atomic force constants without the benefit of any symmetry considerations. It is therefore necessary to calculate the Debye-Waller factor of amorphous solids by computing the MSD of atoms in real space. Since the MSD of an atom at high temperatures can be shown to be proportional to the inverse square of the normal-mode frequencies in the harmonic approximation, it is also necessary to employ a reasonably large model of amorphous solids in an effort to include the contribution of atomic displacements from low-frequency normal modes of the system. This requirement can pose a computational impediment to accurate *ab initio* calculations of the MSD of atoms in real space for large models using an extended set of basis functions [194]. In this paper, we undertake such a task and study the effect of local disordering and atomic coordination on the MSD of atoms in amorphous silicon (*a*-Si). The effect of the Debye-Waller factor on the intensity of diffraction peaks is studied with emphasis on the first sharp diffraction peak (FSDP) and the principal peak of *a*-Si. The variation of the MSD of atoms with temperature in the presence of coordination defects and short- and medium-range ordering in *a*-Si networks is discussed. We also examine the effect of the temperature-induced anharmonicity on the vibrational dynamics of Si atoms in *a*-Si at high temperatures and the possible role of low-frequency vibrations on the molar specific heat of *a*-Si at low temperatures. Furthermore, the Debye temperature of *a*-Si is computed using the harmonic and quasiharmonic approximations and the results are compared with the same obtained from experiments.

Section 6.2 is devoted to the development of model *a*-Si networks and incorporation of defects and extended-range inhomogeneties, which are followed by quantum-mechanical lattice-dynamical calculations of the MSD of atoms in real space in the harmonic approximation and direct *ab initio* molecular dynamics (AIMD) simulations without the use of the harmonic approximation. Section 6.3 presents results and discussion, where the role of short-range ordering and coordination defects on the MSD of atoms is examined at low and high temperatures. The Debye temperature and the molar specific heat of *a*-Si are calculated and compared with the corresponding experimental values from the literature. A discussion of role of the low-frequency vibrations of *a*-Si and their effects on the molar specific heat is presented and the effect of anharmonicity on the MSD of atoms at high temperatures is discussed in this section. The conclusions of our work in given in Sec 6.4 .

6.2 Method and Models

In this study, we have used a set of high-quality *a*-Si models obtained from a combination of classical and AIMD simulations. The term 'high-quality' here refers to the fact that structural, electronic, and vibrational properties of the models are in good agreement with experimental data and that the models are free from any coordination defects. Below, we give a brief description of the simulation method for model construction, which is followed by lattice-dynamical calculations of the MSD of atoms in the harmonic approximation. The calculation of the MSD from direct AIMD simulations that take into account the volume expansion of *a*-Si and the anharmonicity in atomic forces at high temperatures is also discussed in this section.

6.2.1 Generation of *a*-Si models

The simulation method employed here consists of two steps. In the first step, several 500-atom and 1000-atom defect-free configurations, confined in a cubic simulation cell with the experimental mass density of *a*-Si of 2.28 g cm^{-3} [125], were produced using the modified Stillinger-Weber (SW) potential [195] via classical MD simulations. The simulations were performed in canonical ensembles with a time step of 1 fs, and the temperature of the system was maintained by a chain of Nosé-Hoover thermostats [127, 128]. The second step involved thermalization of the resulting classical models at 300 K using AIMD simulations. The AIMD runs were conducted for 5 ps using the density-functional code SIESTA [196] by employing a set of double-zeta (DZ) basis functions [194]. The use of the DZ basis functions is necessary for the calculation of the mean-square displacement (MSD) of atoms, which was found to be dependent on the choice of the basis functions. The total energy and forces were computed by solving the Kohn-Sham equation in the self-consistent field approximation, and the exchange-correlation contribution to the total energy was obtained by using the generalized gradient approximation (GGA). The resulting configurations from the AIMD runs were further relaxed geometrically via the limited-memory Broyden-Fletcher-Goldfarb-Shanno algorithm [197] to obtain a set of final structures for studying the Debye-Waller factor in *a*-Si. A detailed discussion of the method employed here and the validation of the resulting models can be found in Ref. [129]. For the calculation of the MSD of tetrahedral sites, we have used two independent 500-atom models of *a*-Si with no coordination defects in the networks.

In order to examine the effect of coordination defects and extended-range inhomogeneities on the Debye-Waller factor of *a*-Si, we have also studied a few defective models with dangling bonds and voids. Specifically, we have used five independent configurations

with 2–3 at. % of dangling bonds and two additional independent configurations with no coordination defects but a pair of spherical voids of radius 4 Å to generate robust MSD statistics. The dangling bonds (DB) studied in this work are of two types. The first type of DBs are vacancy-induced, which can be produced by removing a tetrahedrally-bonded Si atom from a 100% defect-free *a*-Si network. The removal of a tetrahedrally-bonded atom creates four neighboring dangling bonds (DB) at the vacancy site. Several such quartets of DBs were introduced in the network and the resulting network was annealed at 300 K (and 600 K) for a time period of 5 ps, followed by *ab initio* total-energy relaxation of the networks. Care was taken to ensure that at least 2–3 at. % of the total DBs persist in the final configurations. The second type of DBs studied here are sparsely distributed in the network, with no neighboring DBs in the vicinity of 10 Å. Since direct MD simulations cannot produce these isolated DBs in a controlled manner, we have employed an accelerated metadynamics simulation method to generate these models. Metadynamics simulations of *a*-Si [198] can produce configurations with a given concentration of *n*-fold-coordinated Si atoms, with *n*=2–5, for generating a sparsely distributed DBs in the networks. A description of the method in the context of simulating *a*-Si models via metadynamics simulations was discussed by some of us in Ref. [198]. The configurations obtained from metadynamics simulations were thermalized at 300 K (and 600 K) for 5 ps, followed by *ab initio* total-energy relaxation. Likewise, two independent 100% defect-free *a*-Si models were used to produce models with a pair of nanometer-size voids by thermalizing and relaxing the configurations. The final configurations were used to study the effect of voids on the MSD of Si atoms.

6.2.2 Debye-Waller factor from lattice-dynamical calculations

To study the temperature dependence of the MSD of atoms in a vibrating solid, we have taken two distinct approaches. The first approach involves lattice-dynamical calculations in the harmonic approximation, whereas the second approach relies on direct AIMD simulations in canonical and microcanonical ensembles. The latter enables us to include some aspects of temperature-induced anharmonic effects that can appear at high temperatures. Assuming that $u_{i\alpha}(t)$ is the displacement of atom i along the α direction, where $\alpha = (x,y,z)$, the potential energy of the vibrating system can be written as a Taylor expansion about the equilibrium positions of the atoms. Neglecting the cubic and higher-order terms for small atomic displacements and noting that the linear terms vanish at the equilibrium position, the equations of motion can be written as

$$m_i \ddot{u}_{i\alpha}(t) = -\sum_{j\beta} K_{i\alpha,j\beta}\, u_{j\beta}. \tag{6.1}$$

The coefficient $K_{i\alpha,j\beta}$ is an element of the force-constant matrix and it denotes the magnitude of the force acting on the i-th atom along the α direction when the j-th atom is displaced by a unit distance along the β direction. Substituting $v_i = \sqrt{m_i}u_i$, and assuming the solution of (6.1) to be simple harmonic, $v(t) = v_0 \exp(-\imath\omega t)$, the system of linear equations in (6.1) can be expressed in a matrix form

$$\mathbf{D} - \omega^2 \mathbf{I} = \mathbf{0}. \tag{6.2}$$

Here, $\mathbf{D}$ is a real symmetric $3N \times 3N$ matrix, which is known as the mass-adjusted force-constant matrix or the dynamical matrix, $D_{i\alpha,j\beta} = K_{i\alpha,j\beta}/\sqrt{m_i m_j}$, and $\mathbf{I}$ is the identity matrix. The eigenvalues and the normalized eigenvectors of $\mathbf{D}$ give the squared frequencies (ω^2) and the polarization vectors ($\hat{\mathbf{e}}$) of the atoms for the normal modes, respectively. For a system in stable mechanical equilibrium, all the eigenvalues of $\mathbf{D}$ are positive. The atomic displacement at site i is obtained from a linear combination of the normal modes

$$\mathbf{u}_{i\alpha}(t) = \frac{1}{\sqrt{m_i}} \sum_n A_0(n)\, \hat{\mathbf{e}}_{i\alpha}(n)\, e^{-\imath\omega_n t} \ (\alpha = x, y, z). \tag{6.3}$$

In Eq. (6.3), $A_0(n)$ is the vibrational amplitude for the n-th normal mode, which may include a phase factor, and $\hat{\mathbf{e}}_{i\alpha}(n)$ are the three polarization vectors of atom i, for $\alpha = (x, y, z)$, associated with the mode n. The value of $A_0(n)$ is indeterminate from Eq. (6.2), but it can be obtained by calculating the average kinetic/potential energy of the system in thermal equilibrium. Assuming $\mathcal{T}$ is the average kinetic energy, we have

$$\begin{aligned}
\mathcal{T} &= \left\langle \sum_{i,\alpha} \frac{1}{2} m_i \dot{u}_{i,\alpha}^2 \right\rangle \\
&= \left\langle \sum_{\substack{i,\alpha \\ n,n'}} \frac{\omega_n \omega_{n'}}{2} A_0(n) A_0^*(n') \hat{\mathbf{e}}_{i\alpha}(n) \cdot \hat{\mathbf{e}}_{i\alpha}^*(n') e^{\imath(\omega_{n'} - \omega_n)t} \right\rangle \\
&= \left\langle \sum_{n,n'} \frac{\omega_n \omega_{n'}}{2} A_0(n) A_0^*(n')\, \delta_{nn'}\, e^{-\imath(\omega_n - \omega_{n'})t} \right\rangle \\
&= \left\langle \sum_n \frac{1}{2} \omega_n^2 A_0^2(n) \right\rangle = \left\langle \sum_n \frac{1}{2} E_n \right\rangle = \sum_n \frac{1}{2} \langle E_n \rangle
\end{aligned} \tag{6.4}$$

where we have used the orthonormality condition

$$\sum_{i,\alpha} \hat{\mathbf{e}}_{i\alpha}(n) \cdot \hat{\mathbf{e}}_{i\alpha}^*(n') = \delta_{nn'}$$

and the last step in Eq. (6.4) follows from the non-interacting nature of the normal modes in solids. A similar calculation shows that the average potential energy, $\mathcal{V}$, of the system is also

given by Eq. (6.4). Since the normal modes can be treated as a set of independent harmonic oscillators, the average energy $\langle E_n \rangle$ for each mode in thermal equilibrium at temperature T is given by the quantum-mechanical expression

$$\langle E_n \rangle = \hbar\omega_n \left[\frac{1}{2} + \frac{1}{\exp(\hbar\omega_n / k_B T) - 1} \right] \tag{6.5}$$

and the MSD follows from Eqs. (6.3)–(6.5)

$$u_{i\alpha}^2 = \sum_n \frac{\langle E_n \rangle}{m_i \omega_n^2} |\hat{\mathbf{e}}_{i\alpha}(n)|^2 \tag{6.6}$$

$$= \sum_n \frac{\hbar |\hat{\mathbf{e}}_{i\alpha}(n)|^2}{m_i \omega_n} \left[\frac{1}{2} + \frac{1}{\exp(\hbar\omega_n / k_B T) - 1} \right]. \tag{6.7}$$

The MSD, $\langle u^2 \rangle$, can be readily obtained from averaging over all atoms and coordinate directions and the Debye-Waller factor follows from

$$M = \frac{8\pi^2 \sin^2\theta}{\lambda^2} \langle u^2 \rangle, \tag{6.8}$$

where λ and 2θ are the wavelength of the scattering radiation and the angle of scattering, respectively.

At high temperatures, when $\hbar\omega_n / k_B T \ll 1$, one obtains the classical expression of the MSD by substituting $\langle E_n \rangle \approx k_B T$ in Eq. (6.6). The first term in Eq. (6.7) gives the contribution to the MSD from the zero-point motion (ZPM) of atoms, which leads to weak inelastic scattering even at absolute zero temperature [199]. The effect of thermal vibrations of atoms is reflected in the second term. The computation of the MSD in the lattice-dynamical approach can now be summarized as follows: (i) Thermalize the models at each temperature of interest for 5 ps, followed by *ab initio* total-energy optimization to prepare the system for the calculation of the **D** matrices; (ii) Construct the **D** matrices numerically in the harmonic approximation, by displacing each atom, say by 0.005 Å, along the six coordinate directions ($\pm x$, $\pm y$, and $\pm z$); (iii) Diagonalize **D** to obtain the squared frequencies and the polarization vectors of the atoms for each mode, and calculate the MSD from Eq. (6.7). To produce good statistics, the results in Sec 6.3.1 were obtained from defect-free networks by averaging over two independent configurations, whereas those in Sec IIIB are obtained from five to ten independent configurations with 2–3% dangling bonds in the network.

6.2.3 Debye-Waller factor from direct AIMD simulations

The lattice-dynamical approach presented earlier does not include any anharmonic effects and it is suitable for temperatures well below the Debye temperature of solids. The effects

of anharmonicity on the vibrational dynamics of atoms in a-Si can be studied via direct AIMD simulations in canonical and microcanonical ensembles. In this approach, the system is first equilibrated at a given temperature in canonical ensembles so that the vibrational dynamics of the atoms are reflective of any temperature-induced structural changes that may take place in the system. Once the system is in equilibrium at a given temperature in canonical ensembles, it is then allowed to evolve in microcanonical ensembles. The use of microcanonical ensembles maintains the hamiltonian structure of the dynamics and conserves the total energy of the system in the absence of any thermostatting mechanism. Since the use of constant-volume NVE ensembles can partly restrict the system to include the effect of anharmonicity due to thermal expansion, the volume of the system before NVE runs was adjusted for each temperature as

$$V(T) = V(T_0)[1 + \gamma(T - T_0)]^3, \tag{6.9}$$

where γ is the coefficient of linear expansion of a-Si, $V(T)$ is the volume of the system at temperature T, and T_0 = 300 K. For annealed samples of a-Si, the experimental value of γ is of the order of 4×10^{-6} K^{-1}[200]. This value leads to a change of volume of about 0.36% at 600 K from the original volume at T_0 = 300 K. Thus, it is unlikely that a change of temperature from 300 K to 600 K would induce a notable change of MSD values due to the volume expansion of the solid.

The MSDs of the atoms were calculated from equilibrium microcanonical trajectories, and averaging the results over time and independent configurations during microcanonical runs. The MSD of atom i at temperature T can be written as

$$\langle u_i^2(T)\rangle = \langle\langle (r_i(t,T) - r_i^0(T))^2\rangle_t\rangle_{\text{config}}, \tag{6.10}$$

where $r_i(t)$ is the position of atom i at time t and the symbol $\langle\ldots\rangle_X$ denotes averaging with respect to a variable X. Since the approach involves conducting long AIMD simulations in canonical and microcanonical ensembles, using double-zeta (DZ) basis functions for several independent configurations and temperatures, it becomes computationally prohibitive for large system sizes. We shall see later in Sec 6.3.4 that the use of extended or DZ basis functions is of paramount importance to accurately calculate the MSD and the molar specific heat of a-Si. We have therefore restricted our simulations to three 216-atom models of a-Si for the calculation of the MSD. The canonical and microcanonical runs were conducted for a time period of 10 ps each, with a time step of 1 fs, and the atomic trajectories were collected by evolving the system for an additional 10-ps microcanonical run beyond equilibration. The MSD of the atoms were then calculated from Eq. (6.10) for three independent configurations at several temperatures in the range from 300 K to 600 K.

6.3 Results and Discussion

6.3.1 Temperature dependence of the Debye-Waller factor in *a*-Si

In discussing our results, we begin with the variation of the MSD of atoms with the density of model *a*-Si networks. Since the density of *a*-Si samples can depend on preparation methods and experimental conditions, which may affect the local structure of *a*-Si and hence local atomic force constants, it is important to examine whether the vibrational motion of Si atoms is sensitive to the density of *a*-Si in the temperature range of 300–600 K. Figure 6.1 shows the variation, or the lack thereof, of the MSD, $\langle u^2 \rangle$, of atoms with the density of *a*-Si at 300 K and 600 K. The data correspond to the average values obtained from two independent 500-atom model configurations. The results suggest that the MSD is almost independent of the density of *a*-Si within the range of 2.14–2.30 g cm^{-3}. This observation is not surprising, noting that the models studied in this work have no coordination defects and that a small variation of the density – obtained via a homogeneous scale transformation of atomic distances, followed by thermalization at 300 K (and 600 K) for 5 ps and total-energy optimization – from 2.3 to 2.14 g cm^{-3} affects atomic distances by a linear scale factor of s = 1.024. Assuming that the system behaves as a harmonic solid, it can be shown that the MSD remains practically unchanged in the long-wavelength limit under a scale transformation from $\mathbf{r} \rightarrow s\mathbf{r}$ in the nearest-neighbor approximation between atoms. However, a small change of the MSD may result from the high-frequency modes and the deviation from the nearest-neighbor approximation of the atomic force constants [201]. This is apparent from the results shown in Fig. 6.2, where a small shift of the MSD is found to lie well within one standard deviation of the distribution. It may be noted that the results for the model with the lowest density at 300 K and 600 K have been explicitly verified by constructing the model from a starting random configuration with a density of 2.14 g cm^{-3}.

In the lattice-dynamical approach, the dependence of the MSD on temperature is generally studied in the harmonic approximation. Elementary calculations in Sec 6.2.2 show that, for small oscillations in the classical limit, the contribution to the MSD from thermal vibrations is directly proportional to the temperature of the system. However, this linear relationship may not hold at high temperatures, when the presence of thermally-induced anharmonic vibrations and the thermal expansion of a solid can lead to a coupling between normal modes. The anharmonicity in atomic vibrations results in an increase of the MSD of atoms at high temperatures, which we shall discuss in Sec 6.3.5.

Figure 6.3 shows the variation of the MSD, $\langle u^2 \rangle$, with temperature for model *a*-Si networks with a density of 2.28 g cm^{-3}. The contributions to $\langle u^2 \rangle$ from the zero-point motion (ZPM) and thermal vibrations of the atoms are shown separately in the figure. The

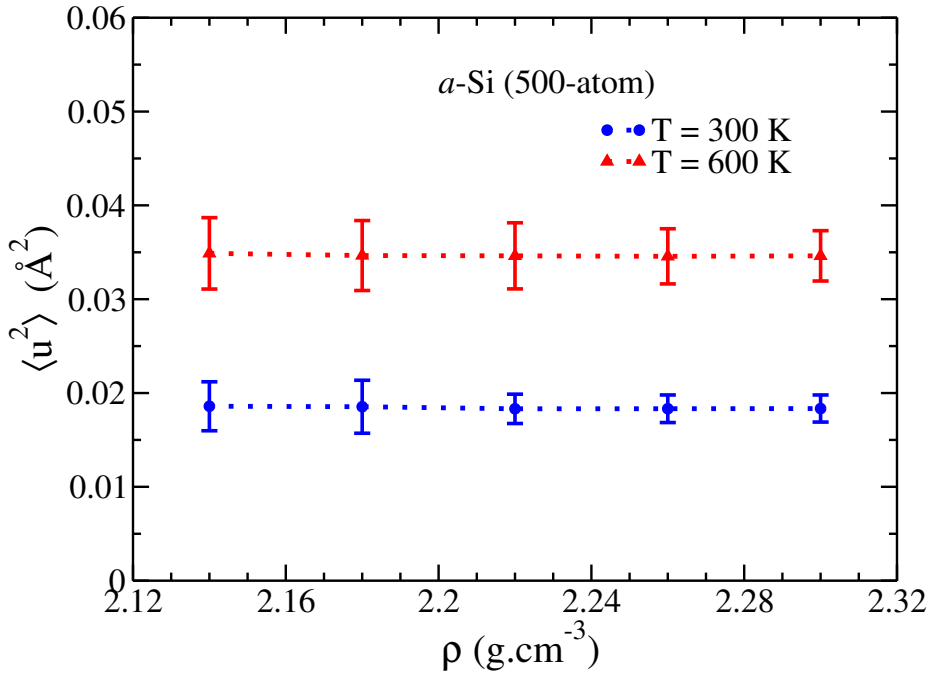

Figure 6.1: The MSD, $\langle u^2 \rangle$, of Si atoms in *a*-Si with its density in the harmonic approximation from lattice-dynamical calculations. The MSD values can be seen to be practically independent of the density at 300 K (blue) and 600 K (red).

MSD values due to thermal vibrations can be seen to increase linearly with temperature in Fig. 6.3, an observation which is consistent with the theoretical results obtained from the harmonic approximation in the temperature range of 300–600 K. For comparison, the MSD values for diamond-structure *c*-Si are also presented in Fig. 6.3. A somewhat higher value of $\langle u^2 \rangle$ in *a*-Si compared to *c*-Si can be attributed to the disorder associated with the local tetrahedral environment of *a*-Si. In *a*-Si, the atoms are bonded to four neighboring atoms in an approximate tetrahedral arrangement, which is characterized by the disorder in the bond-angle and bond-length distributions. The presence of disorder reduces the strength of Si–Si bonds in the amorphous phase. This is in contrast to *c*-Si, where Si atoms are strongly bonded to each other in an ideal tetrahedral arrangement. This strong and compact tetrahedral bonding results in slightly stiffened atomic force constants (and relatively high values for normal-mode frequencies in the harmonic approximation) compared to its amorphous counterpart. Thus, following Eq. (6.6), the MSD of Si atoms in *a*-Si can be expected to be somewhat larger than that in *c*-Si when an identical thermal perturbation is applied to excite the system.

The temperature dependence of the Debye-Waller factor, e^{-2M}, is plotted in Fig. 6.4 for Q = 1.99 Å^{-1} and 3.6 Å^{-1}. These two values of Q correspond to the position of the

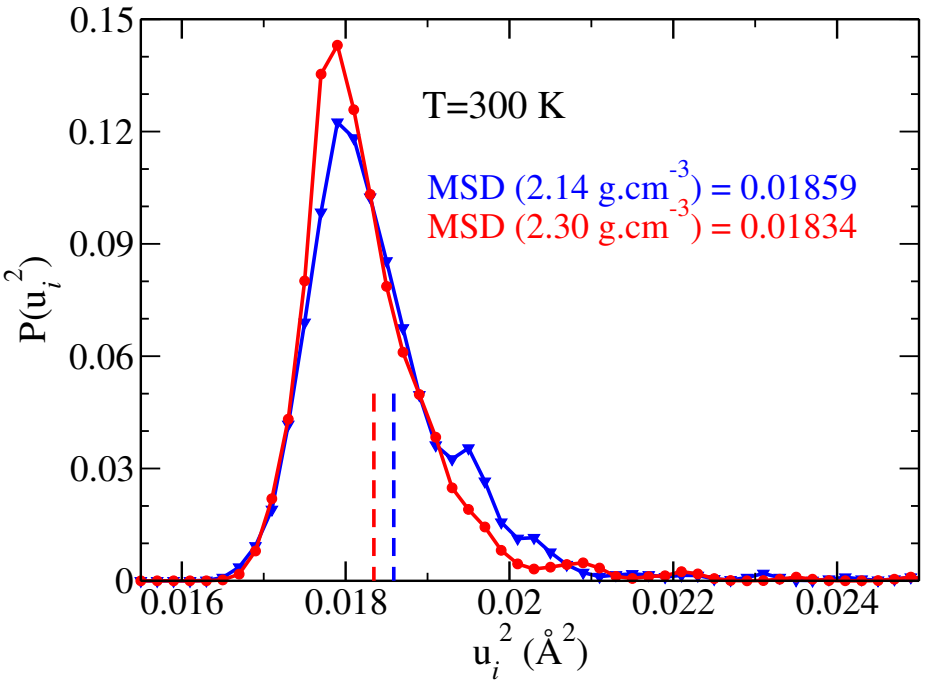

Figure 6.2: A comparison of the distributions of u_i^2 of atoms in a low-density model (blue) and a high-density model (red) of *a*-Si at 300 K obtained from two independent models with no coordination defects. The MSD values for the distributions are indicated as dashed vertical lines.

first sharp diffraction peak (FSDP) and the principal peak in the static structure factor of *a*-Si, respectively. Since the wavevector transfer $|Q| = 4\pi\sin(\theta)/\lambda$, the value of the Debye-Waller factor at different temperatures for the two peaks can be readily calculated for a given scattering wavelength λ. Figure 6.4 shows a plot of e^{-2M} versus T for CuK$_\alpha$ X-radiation with λ = 1.54 Å. The results suggest that the intensity of the principal peak in *a*-Si is considerably affected by thermal motion of the atoms in solids even at 300 K. The intensity of the FSDP at 300 K, however, is reduced by a factor of about 0.94, leading to small inelastic scattering at 300 K. The missing intensity can be found to be present in the background, which originates from temperature-diffuse scattering.

We now examine the role of short-range ordering on the MSD of atoms in amorphous Si networks. Unlike crystals, where one expects a narrow distribution of u_i^2, induced by thermal vibrations of atoms in an identical atomic environment, the MSD of an atom in amorphous networks varies from site to site, and it largely depends on the local atomic coordination and the disorder associated with bond lengths and bond angles. Figure 6.5 shows the distributions of atomic displacements, $P(u_i^2)$ versus u_i^2, in *a*-Si at temperatures 300 K and 600 K, along with their crystalline counterparts. The results correspond to the

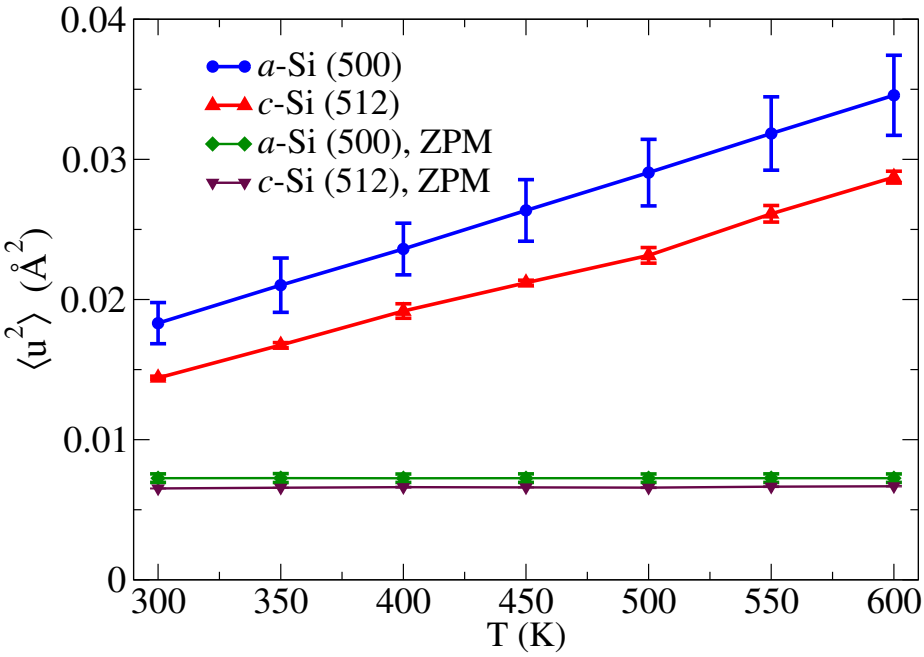

Figure 6.3: The variation of the MSD, $\langle u^2 \rangle$, with temperature in the harmonic approximation for *a*-Si and *c*-Si. The contribution to the MSD from the zero-point motion (ZPM) of the atoms is explicitly shown as horizontal lines.

average values of u_i^2 obtained from two independent defect-free of configurations of 500 atoms. Owing to the crystalline symmetry of atomic positions, the distributions for *c*-Si in Fig. 6.5 are found to be rather narrow and with a root-mean-square width that increases with the temperature of the system. The heights of these distributions are intentionally truncated at a value of 0.1 for clarity of presentation and comparison. By contrast, the distributions for *a*-Si appear almost gaussian for small atomic displacements, except for a weak non-gaussian tail for high values of u_i^2. For crystals, the gaussian shape of $P(u_i^2)$ readily follows from lattice-dynamical considerations and it can be shown analytically [202] that the Fourier transform of $P(u_i^2)$ is directly related to the temperature factor of atoms. However, the presence of local atomic ordering/disordering in amorphous networks can considerably influence the otherwise random thermal motion of atoms, which leads to a notable deviation from an ideal gaussian behavior arising from highly disordered sites. We shall see soon that the non-gaussian behavior of $P(u_i^2)$ is significantly enhanced in the presence of coordination defects and other inhomogeneties in the network.

The origin of the non-gaussian tail, associated with high u_i^2 values, in defect-free *a*-Si networks can be traced back to a few clusters of Si atoms, which are sporadically distributed in the network. These atoms vibrate with relatively high amplitudes compared to the rest of the atoms in the network. This is illustrated in Fig. 6.6, using a 500-atom model of *a*-Si

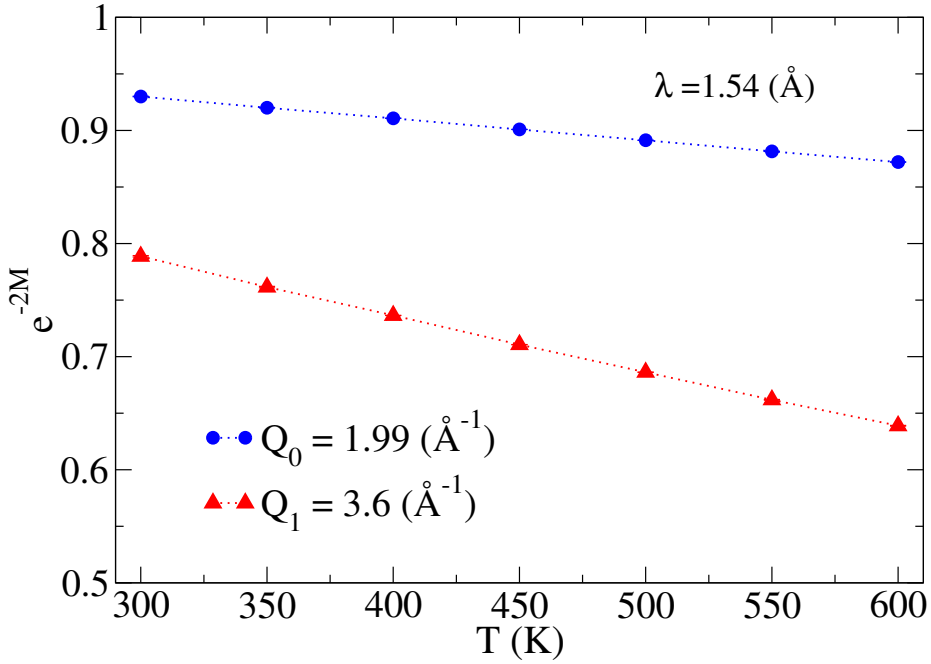

Figure 6.4: The variation of the Debye-Waller factor of *a*-Si, e^{-2M}, with temperature for Q = 1.99 Å^{-1} (blue circles) and 3.6 Å^{-1} (red triangles). The results are obtained by using λ = 1.54 Å, which corresponds to Cu K$_\alpha$ lines. The Q values chosen correspond to the FSDP (1.99 Å^{-1}) and the principal peak (3.6 Å^{-1}) in the structure factor of *a*-Si.

at 300 K. Silicon atoms that are associated with high u_i^2 values, with $u_i^2 > 0.0195$ Å^2, are shown in red color. This translates into a value of atomic displacement, which is about 6% of the average Si–Si bond length of 2.36 Å. An examination of the sites with high u_i^2 values reveals that these sites are characterized by the presence of long Si–Si bonds, the length of which is about 2–5% larger than the average bond length of 2.36 Å. The additional stretching introduces disorder in the bond-length distribution and weakens the bonds. This affects the nearest-neighbor force constants (K) between Si atoms with long bonds and results in a reduction of some normal mode frequencies (as ω^2 typically decreases with decreasing K), leading to a larger value of u_i^2 for these sites from Eq. (6.6) upon thermal excitation.

6.3.2 Effects of defects and inhomogeneities on the MSD

Turning now to discuss the role of structural defects on the MSD and individual squared displacements, we examine the effect of three-fold-coordinated atoms, or dangling bonds, and extended inhomogeneities, such as voids, on the vibrational MSD of atoms. To this end, we have studied two types of dangling bonds. The first type of DBs are vacancy induced, which were produced by removing a tetrahedrally-bonded Si atom, whereas the second type of DBs are sparsely distributed in the network. The creation of these DBs is discussed in

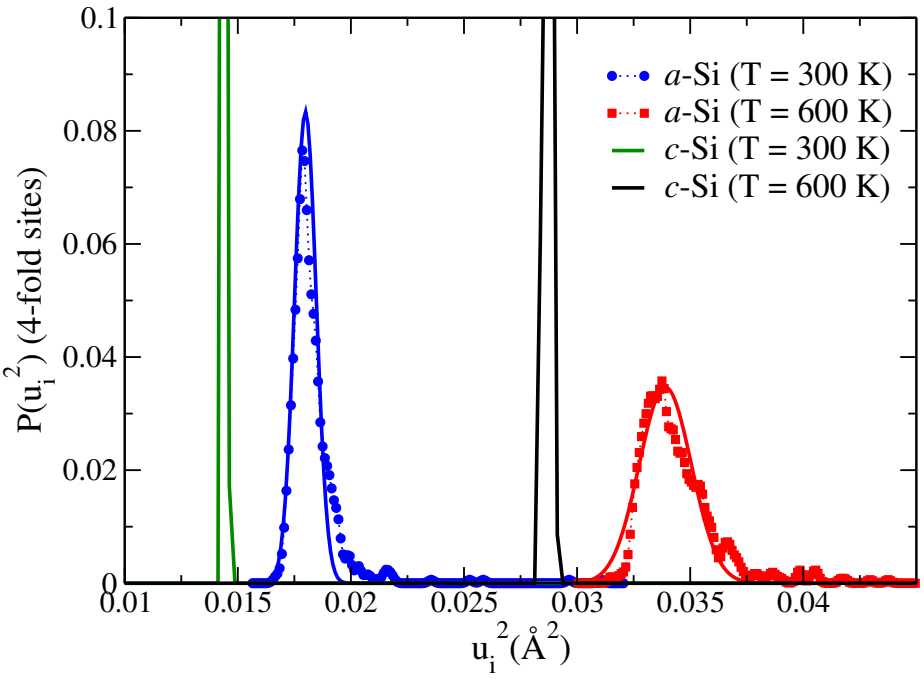

Figure 6.5: The distributions of local squared displacements, u_i^2, for *a*-Si at 300 K (blue) and 600 K (red). The solid lines (blue and red) indicate a gaussian fit of the data. The corresponding results for *c*-Si are also shown in the plot (as green and black lines), which are truncated for visual clarity and comparison. The results for *a*-Si correspond to 100% defect-free networks.

section 6.2.1. In the following, we shall refer to these dangling bonds as clustered (or type I) and isolated (or type II) DBs, respectively. The results of our calculations, which are presented in Figs. 6.7–6.10, enable us to make the following remarks.

First, a comparison of u_i^2 values obtained for the tetrahedral sites with no defects and clustered DB sites (in Fig. 6.7) shows that atomic displacements of the DB atoms are notably larger than their tetrahedral counterpart by a factor of two or more. Second, a small number of DB atoms can be seen to have u_i^2 values larger than 0.05 Å^2 at 300 K, and 0.1 Å^2 at 600 K. This indicates substantial local movement of some atoms near the defective sites and the subsequent healing of a dangling bond to form a tetrahedrally-bonded atom. Indeed, it was observed that a considerable number of clustered DBs introduced in the network reorganized themselves to form stable tetrahedral bonding following thermalization and structural relaxation. Third, a relatively large value of u_i^2 at the DB sites can be partly attributed to the presence of reduced atomic coordination, which renders the atoms more susceptible to move. A normal-mode analysis reveals that a few low-energy modes contribute considerably to u_i^2 of the DBs compared to the tetrahedral sites. This is evident from Fig. 6.8, where a color-map representation of $u_i^2(\nu_j)$ – the contribution to u_i^2 at the

DB site i from the normal mode ν_j – is presented against the normal-mode frequencies and atomic sites. The left panel in Fig. 6.8 corresponds to the results obtained for the clustered DBs at 300 K, whereas the right panel shows the same for an identical number of tetrahedrally-bonded atoms. Atomic indices of sixty-five clustered/tetrahedral sites are indicated along the abscissa, whereas the first eighty low-frequency normal modes are indicated along the ordinate. The color in the plot is indicative of the partial contribution of $u_i^2(\nu_j)$ (in percent) to the total MSD of atom i. The significant presence of red specks in the left panel is indicative of high contributions arising from a few tens of low-frequency normal modes at the clustered DB sites. The vertical indices along the Y axis correspond to the frequency range of 0 to 110 cm^{-1} for j=1 to 80. A similar observation applies to Fig. 6.9 where the results for the isolated DBs are presented.

The distributions of u_i^2 obtained for the clustered and isolated DBs are found to be quite different from each other. This is evident from Fig. 6.10, where the distributions resulting from the clustered (filled red) and isolated (filled green) DBs at 300 K are plotted. The fine structure in the distribution for the latter is reflective of the degree of sparsity of the isolated DBs in the network. The first green peak in Fig. 6.10 indicates the presence of several truly isolated DBs in the network. The subsequent green peaks are reflective of a somewhat lesser degree of sparsity of the remaining isolated DBs in the network. An analysis of the

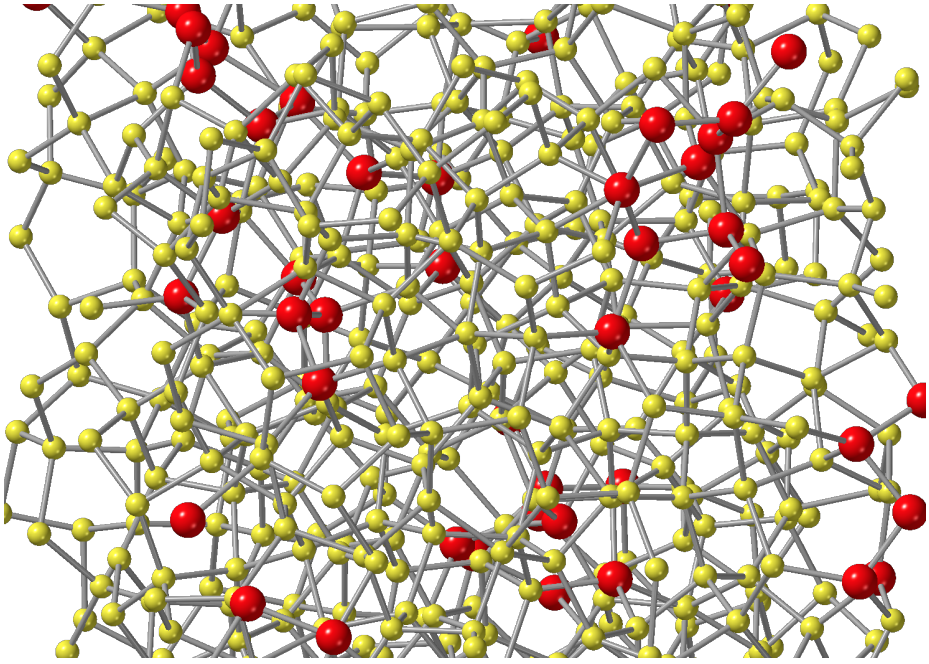

Figure 6.6: A 500-atom model of *a*-Si showing several Si atoms with a large value of u_i^2 at 300 K. Silicon atoms with top 10% of u_i^2 values are shown in red color with a slightly larger radius. The rest of the atoms are shown in yellow color.

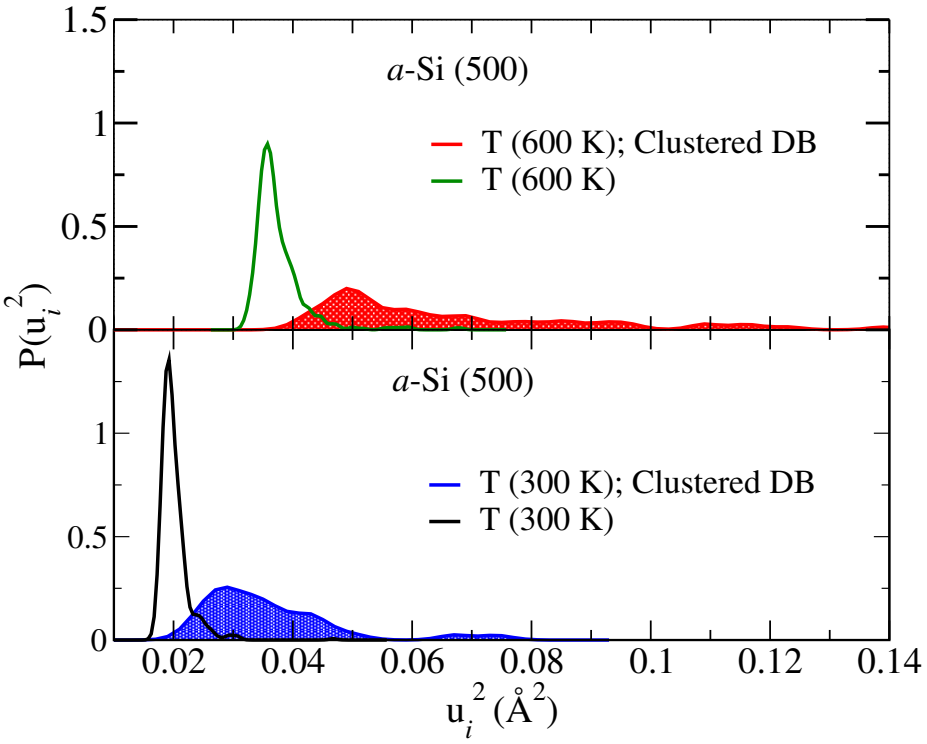

Figure 6.7: A comparison of the distributions of u_i^2 for the tetrahedral sites (black and green) of 100% defect-free *a*-Si networks and the clustered DBs (filled blue and red) at 300 K and 600 K. The distributions are normalized to an integrated value of 10^{-2}.

distribution of the isolated DBs in the networks shows that almost half of the 65 DBs are sparsely distributed in the network with an average separation distance of 10.3 Å, and a good majority of these sites contribute to the first (green) peak.

Likewise, the effect of microvoids on the MSD of atoms can be studied by introducing a couple of voids in the network. Figure 6.11 shows the MSD at 300 K, 450 K and 600 K, before and after introducing two voids of diameter 8 Å in two 500-atom models of *a*-Si. The plots in Fig. 6.11 show that the MSD has considerably increased due to the presence of several defective atoms on the surface of the voids. The presence of local disorder and reduced coordination considerably weakens the effective force constants between neighboring atoms that leads to an increase of the MSD of the atoms on the surface of the voids.

6.3.3 Debye temperature of *a*-Si from the MSD of atoms

Having discussed the variation of the MSD of atoms with temperature in the presence of disorder and defects, we now obtain estimates of the Debye temperature, Θ_d, and compare the results with those from experiments. To this end, we first note the following caveat

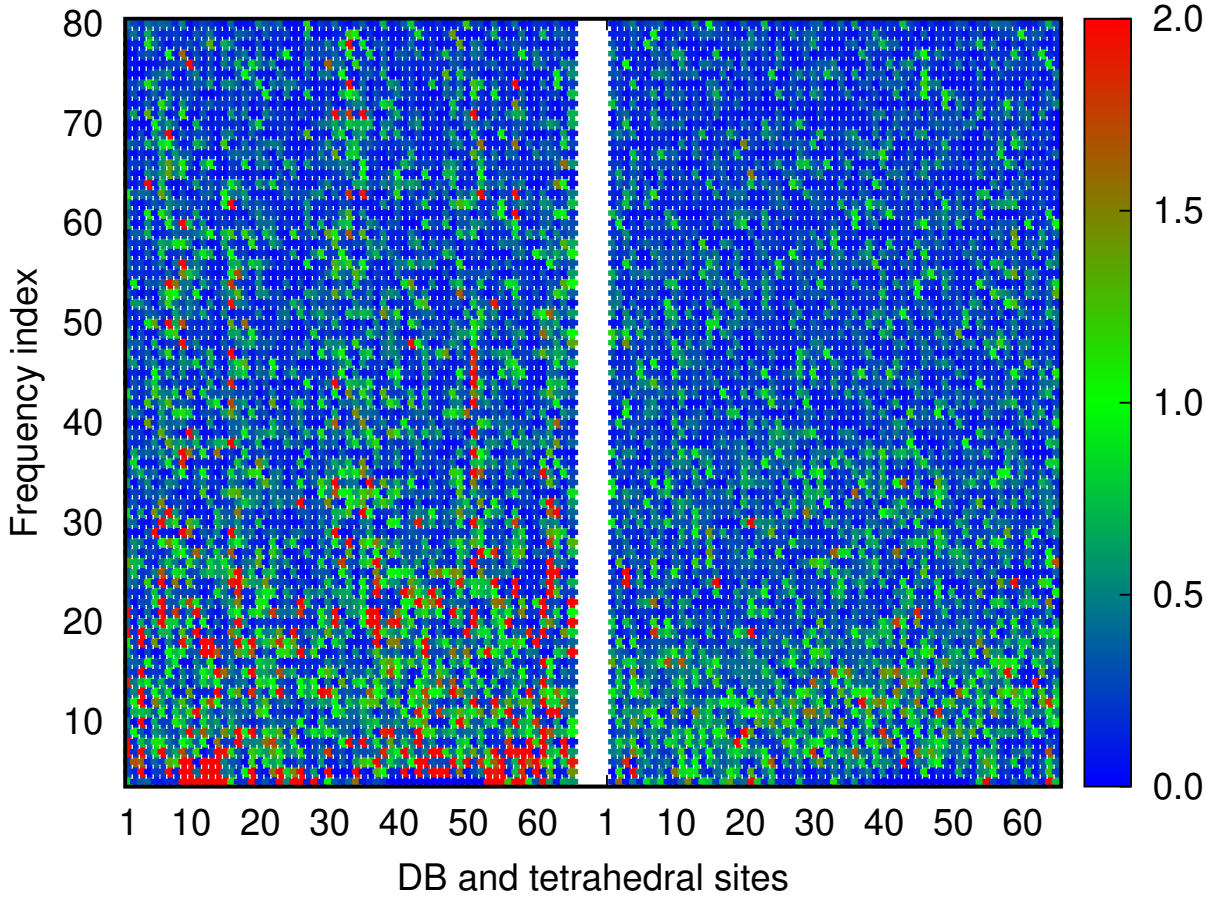

Figure 6.8: A color map showing the contribution to u_i^2 at *clustered* DB sites (left panel) and tetrahedral sites (right panel) from the first eighty normal modes (indexed along Y axis) at 300 K, distributed in the frequency range of 0 and 110 cm^{-1}. The abundance of red specks in the left panel indicates a large contribution at the DB sites from the low-frequency modes. The rightmost vertical bar indicates the percentage contribution of $u_i^2(\nu_j)$ to total u_i^2. The results correspond to 65 DB sites and tetrahedral sites selected from the same models.

about the definition of the Debye temperature for amorphous solids. In experiments, the Debye temperature of crystalline solids is generally determined by comparing the measured specific-heat data at low temperatures (below 25 K) with the expression for the specific heat given by $c_1T + c_3T^3$ in the Debye approximation, where the coefficient c_1 is related to the contribution from the electronic degrees of freedom and c_3 involves the Debye temperature Θ_d. At sufficiently low temperatures, the density of states (DoS) of low-frequency vibrations in crystals can be adequately represented by a quadratic function of the frequency, which results in a T^3 dependence of the specific heat. This justifies the use of the Debye approximation and the resulting Debye temperature as a physical parameter for crystalline solids. For amorphous solids, however, the above reasoning is weakened by

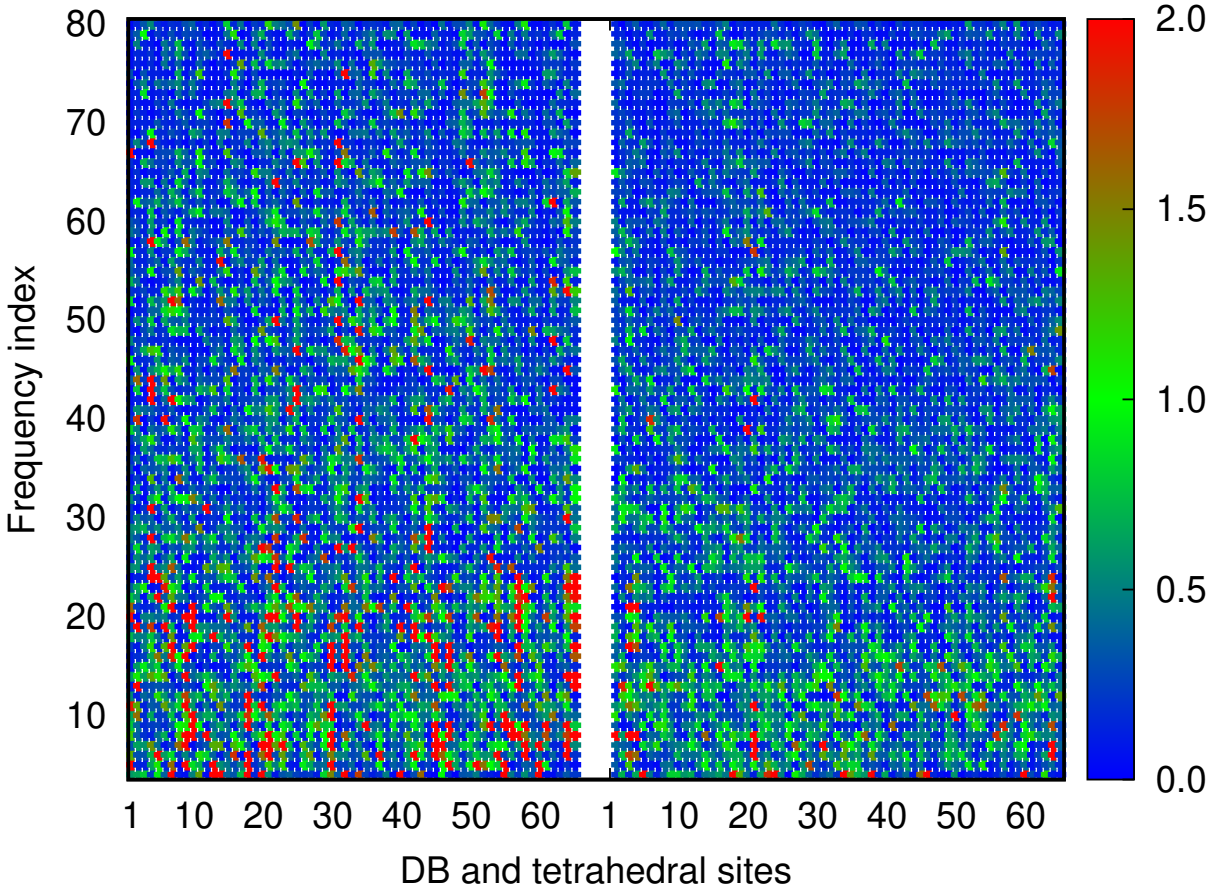

Figure 6.9: A color map showing the contribution to u_i^2 at *isolated* DB sites (left panel) and tetrahedral sites (right panel) from individual low-frequency normal modes at 300 K. The left panel is awash with red specks indicating a high contribution from the low-frequency in the range of 0–110 cm^{-1} modes at the DB sites. The results correspond to 65 DB sites and tetrahedral sites from the models.

the presence of excess low-frequency vibrations in some systems, leading to vibrational DoS that may not be well represented by a quadratic function of frequency. This in turn can affect the temperature dependence of the specific heat of amorphous solids. For a number of glassy systems the coefficient c_3 can be greater than the Debye coefficient c_3^d even if the T^3 dependence of the specific heat is assumed to hold at low temperatures. Since the experimental values of Θ_d of a-Si reported in refs. [203] and [204] are obtained by assuming $c_3 = c_3^d$, we make the same assumption to calculate Θ_d for the purpose of comparison in section 6.3.4.

In this section, we calculate an estimate of the Debye temperature of a-Si from the computed values MSDs at low temperatures by comparing the MSDs with those obtained from the Debye theory. To achieve this, we start by writing the expression for the MSD at

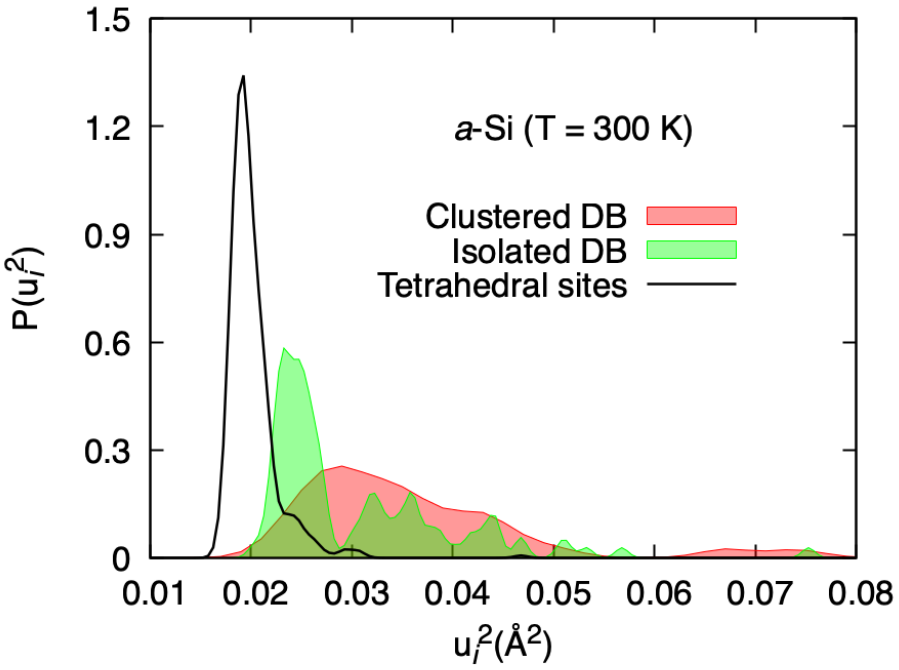

Figure 6.10: The distributions of u_i^2 for clustered (red) and isolated (green) DBs in *a*-Si networks at 300 K. The results correspond to the data obtained from 65 DBs from two sets of five independent models. The results for the tetrahedral sites (black) are from two 100% defect-free *a*-Si networks. The distributions are normalized to an integrated value of 0.01.

temperature T in the Debye approximation [202]

$$u_d^2(T) = \frac{9\hbar^2}{mk_BT}\left[\frac{1}{4x_d} + \frac{1}{x_d^3}\int_0^{x_d}\frac{x\,dx}{e^x - 1}\right], \tag{6.11}$$

where $x_d = h\nu_d/k_BT = \Theta_d/T$ and ν_d is the Debye frequency. In our approach, we proceed to calculate Θ_d from Eq. (6.11) by replacing $u_d^2(T)$ with $\langle u^2(T)\rangle$. To ensure that the Debye approximation remains valid, we limit ourselves to $\langle u^2(T)\rangle$ values obtained at low temperatures of up to 50 K. The Debye temperature is obtained numerically by calculating the value of x_d for which Eq. (6.11) [with $u_d^2(T) \to \langle u^2(T)\rangle$] is satisfied at temperatures of 10 K, 30 K and 50 K. The average value of x_d and Θ_d are computed from the results. Table 6.1 lists the results from our calculations. The estimated value of the average Debye temperature, for *a*-Si is found to be 541.5±4 K. We should mention that the absence of low-frequency vibrational modes in small 500-atom *a*-Si models underestimates the MSD values at low temperature due to the inverse-square dependence of the MSD on frequency. Thus, the Θ_d value obtained here provides a lower bound of the actual Debye temperature of *a*-Si.

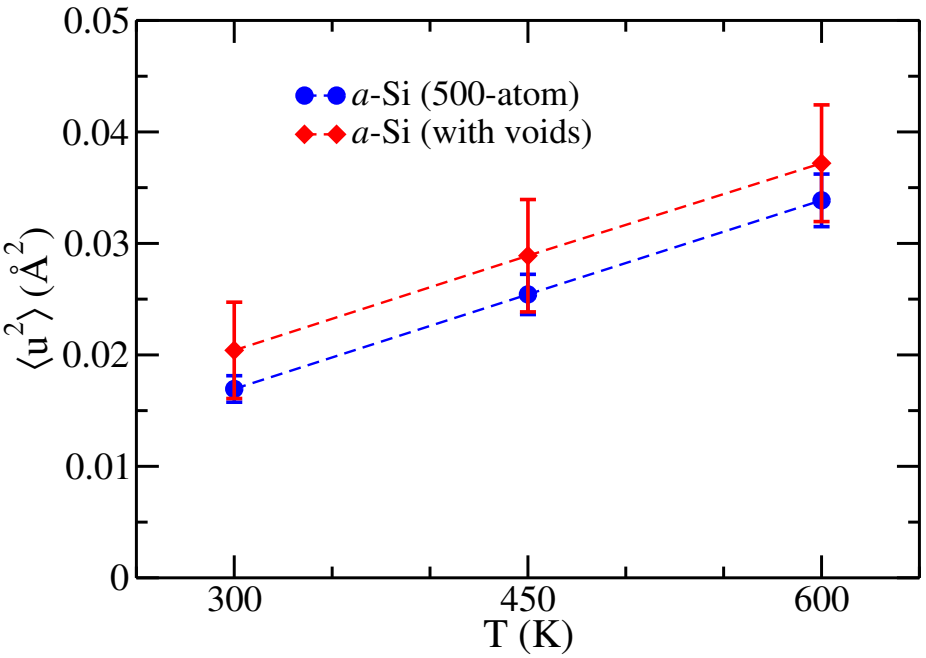

Figure 6.11: The MSDs of Si atoms obtained from 500-atom models of *a*-Si in the presence of two voids (red diamonds) at 300 K, 450 K, and 600 K. The corresponding values of the MSD without voids (blue circles) are also shown in the plot for comparison.

Table 6.1 lists the average values of Θ_d obtained from the MSDs in the temperature range of 10–50 K, along with the experimental values of Θ_d. The computed value of Θ_d in table 6.1 is considerably higher than the value of 430–470 K obtained by Feldman et al. [205]. These authors employed 216-atom models of *a*-Si and classical potentials to compute elastic constants and hence the Debye temperature. The large difference between these two values is not unexpected as the computation of Θ_d from different theoretical approaches may vary notably, depending upon the size and quality of structural models, the accuracy of total-energy and forces used in the calculations, and the sensitivity of calculations. Experimental values of Θ_d, obtained from specific-heat measurements of *a*-Si at low temperature in the Debye approximation, suggest that Θ_d values can vary from 478$\pm$5 K [203] to 528$\pm$20 K [204]. The Θ_d value obtained from the inversion of Eq. (6.11) in our work is close to that of Mertig et al. [204] but notably higher than that observed by Zink et al. [203]. In the next section, we shall further address this issue by calculating the specific heat of *a*-Si and comparing the results with those from the Debye approximation at low temperature.

Table 6.1: Debye temperatures (Θ_D) of *a*-Si obtained from the mean-square displacements and specifc-heat data at low temperature.

	T_s (300 K)			Expt.	T_s (350 K)		
T (K)	$\langle u^2 \rangle$ (Å^2)	x_D	$\theta_D(T)$ K	θ_D (K)	$\langle u^2 \rangle$ (Å^2)	x_D	$\theta_D(T)$ (K)
10	0.00725	53.632	536.31		0.00725	53.606	536.06
30	0.00730	18.092	542.76	487± 5 [203]	0.00731	18.079	542.37
50	0.00752	10.903	545.17	528± 20 [204]	0.00753	10.889	544.48

6.3.4 Debye temperature from the specific heat of *a*-Si

In this section, we compute the molar specific heat of *a*-Si from *ab initio* lattice-dynamical calculations in the harmonic approximation, and compare the results from experiments. We then attempt to obtain an estimate of Θ_d by invoking the Debye approximation at low temperature and compare Θ_d with the same from experiments and that from MSDs. The total vibrational energy of a solid at temperature T, consisting of N atoms, can be written as a sum of the energy of individual normal modes

$$\begin{aligned} E_{tot} &= \sum_{i=1}^{3N} \left[\frac{1}{2} + \frac{1}{\exp(\hbar\omega_i/k_BT) - 1} \right] \hbar\omega_i \\ &= E_0 + E_T \end{aligned} \tag{6.12}$$

and the molar specific heat, C_v, is given by

$$\frac{C_v}{3R} = \frac{1}{3N} \sum_{i=1}^{3N} \frac{k_B x_i^2 e^{x_i}}{(e^{x_i} - 1)^2}, \text{ where } x_i = \frac{\hbar\omega_i}{k_BT}. \tag{6.13}$$

In Eq. (6.12), the first term E_0 gives the total zero-point energy of the solid, which can be also written as

$$E_0 = \sum_{i=1}^{3N} \frac{1}{2}\hbar\omega_i = \int_0^\infty [C_v(\infty) - C_v(T)]\, dT. \tag{6.14}$$

In practical calculations, the upper limit of the integral in Eq. (6.14) is replaced by a sufficiently high but finite temperature, and $C_v(\infty)$ indicates the classical value of $3Nk_B$ at high temperatures. For a Debye model, the value of the zero-point energy integral is given by $\frac{9}{8}Nk_B\Theta_d$, which can be readily compared with the value obtained from the lattice-dynamical calculations. This is illustrated in Fig. 6.12, where the integral value from Eq. (6.14) is found to converge monotonically to the zero-point energy for temperatures in the vicinity of 3000 K. The corresponding value for the Debye model is also shown for Θ_d = 541.5 K. The Debye model underestimates the value of the zero-point energy by about 17% from the *ab initio* lattice-dynamical results.

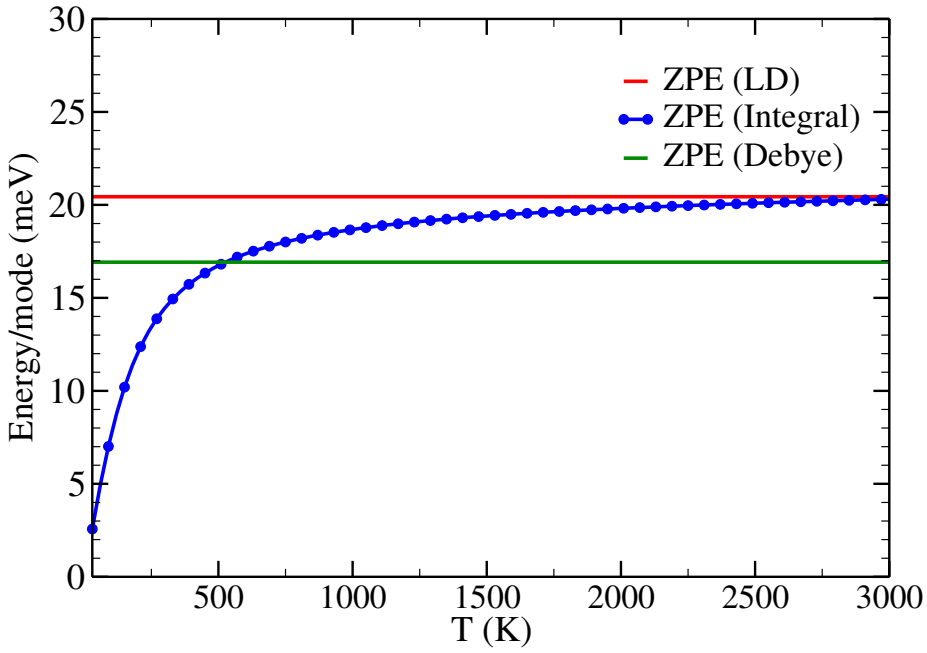

Figure 6.12: The convergence of the mean zero-point energy (ZPE) per vibrational mode for *a*-Si obtained from the integral representation in Eq. (6.14) with temperature (blue line). The horizontal lines correspond to the results obtained from the sum of vibrational frequencies (red line at 20.5 meV) and that from the Debye model (green line at 17 meV). A value of Θ_d = 541.5 K is used to calculate the ZPE from the Debye approximation.

The molar specific heat C_v of *a*-Si at different temperature can be calculated from Eq. (6.13) and the results can be compared with those obtained from the Debye approximation, using either the experimental value or the lattice-dynamical value of x_d (or Θ_d) from our work

$$\left[\frac{C_v}{3R}\right]_d = \frac{3}{x_d^3}\int_0^{x_d} \frac{x^4 e^x\, dx}{(e^x-1)^2} \quad \text{with } x_d = \Theta_d/T. \tag{6.15}$$

The results obtained from Eqs. (6.13) and (6.15) are plotted in Figs. 6.13–6.14 as a function of $1/x_d$. Here, we have used the experimental values of Θ_d = 487 K and 528 K from Refs. [203, 204] and the theoretical value of 541.5 K obtained from *ab initio* calculations presented in Sec 6.3.3. An analysis of the plots in Figs. 6.13 and 6.14 leads to the following observations:

1) A small change of Θ_d, and hence x_d, has very little to no effect on C_v. This is not unexpected in view of the integral nature of Eq. (6.15) and it is reflected in Fig. 6.13, where Θ_d = 487 K and 528 K were used to obtain C_v in the Debye approximation, leading to almost identical values of C_v. It is evident from Fig. 6.13 that the Debye approximation considerably overestimates the value of C_v in *a*-Si – compared to that from *ab initio* lattice-dynamical calculations – above a certain temperature T_c ($\sim$ 84 K) and underestimates it below T_c.

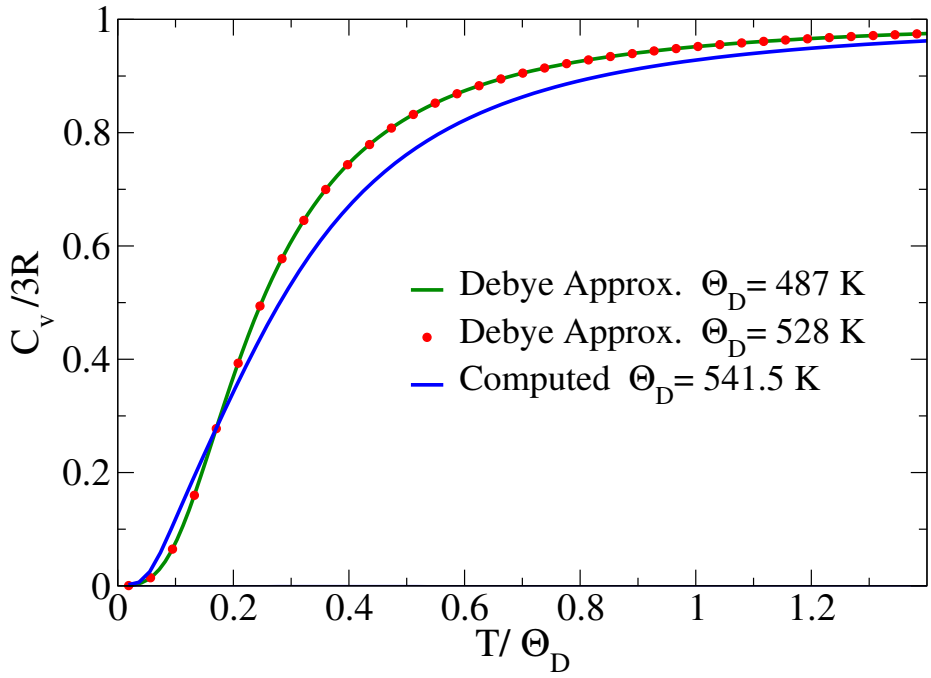

Figure 6.13: The temperature dependence of the molar specific heat, C_v, of *a*-Si from the Debye approximation (green line and red circles) and *ab initio* lattice-dynamical calculations (blue line). The results for the Debye approximation are obtained by using Θ_d = 528 K and 487 K (from Refs. [204] and [203], respectively).

Figure 6.14 shows the low-temperature behavior of C_v, which clearly indicates that the crossover temperature T_c is in the vicinity of $0.16\Theta_d$ or 84 K;

2) The linear variation of C_v with T in the low-temperature region of 30–60 K (i.e., $x_d^{-1} \approx$ 0.06 to 0.1) in Fig. 6.14 markedly deviates from the Debye-T^3 law at low temperatures. A linear behavior of C_v is well-known in the experimental literature of non-crystalline solids, including for *a*-SiO_2, *a*-Se [203, 206, 207] and dilute magnetic alloys [208], at temperature of up to 10 K. This behavior is often attributed to the presence of tunneling modes in two-level systems (TLS) [209] at low temperatures or due to the presence of vibrational modes in reduced dimensions, where the presence of ordered/disordered parallel atomic chains (e.g., in Se/*a*-Se) can lead to a linear behavior over a certain range of temperature. By contrast, the linear variation of C_v observed here in Fig. 6.14, which is evident in both experimental and theoretical results, appears at considerably higher temperatures of 30-60 K than 10 K.

3) The peak positions in the experimental and computed plots of C_v/T^3 vs. T in Fig. 6.15 are found to be at x K and y K, respectively. A small rightward shift of the computed peak with respect to its experimental counterpart possibly arises from the absence of some

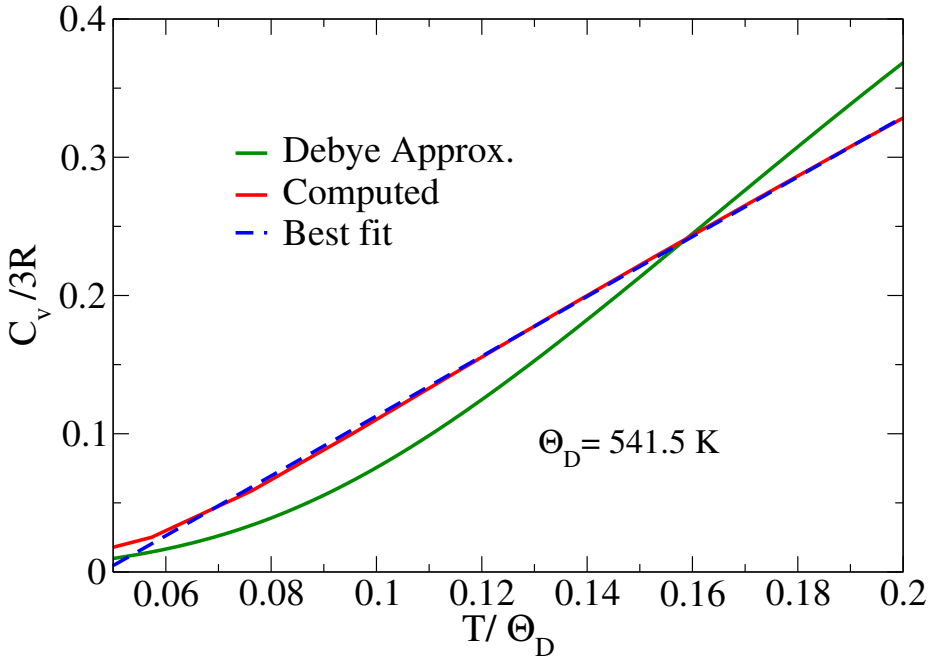

Figure 6.14: Low-temperature behavior of C_v in *a*-Si from the Debye approximation (red line), *ab initio* lattice-dynamical calculations (blue line), and experiments [204] (black line) in the region of 20–130 K. An approximate linear behavior of C_v can be seen to appear in the vicinity of 45 K in both experimental and theoretical results, which corresponds to a frequency value of about 0.9 THz.

low-frequency modes in small models that leads to a slight reduction of the specific heat (as no energy is needed to excite the missing modes) and causes the peak to move toward a higher temperature. However, a direct conformation of this surmise is outside scope of the presence work due to the small size of models employed in our study.

5) Finally, the argument presented above suggests that lattice-dynamical results obtained from small models may not reproduce the experimental C_v data of *a*-Si accurately below 80 K due to the absence of the low-frequency modes near the 1-THz region in the VDOS of our models. This is reflected in Fig. 6.15, where we have compared the results from the lattice-dynamical calculations in the harmonic approximation with the experimental data reported by Zink et al [203]. The difference between the experimental and theoretical values of C_v below 50 K is noticeable and it is likely to originate from the absence of a small number of excess low-frequency modes or the boson peak in the vibrational density of states in small models. To ensure that this difference is not simply related to conventional finite-size effects, we have verified our results using larger 1000-atom models. The results from two larger 1000-atom models do not exhibit any visible change in Fig. 6.15. This is understandable because in order to observe the possible contribution of the frequencies near the boson peak

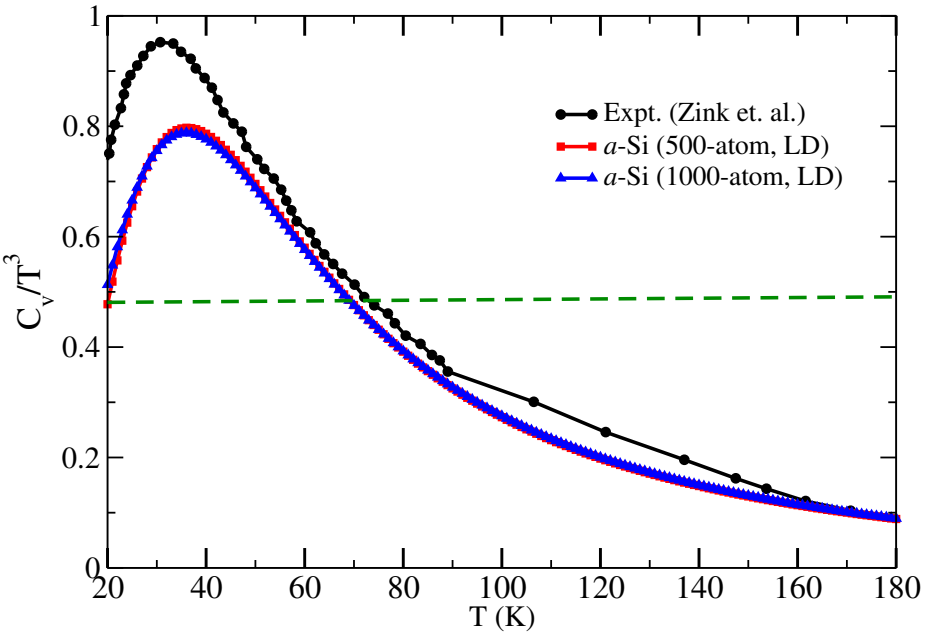

Figure 6.15: A comparison of the specific heat, C_v, of a-Si at low temperatures from experimental data (black) in Ref. [203] and the present study, using 500-atom (red) and 1000-atom (blue) models, in the lattice-dynamical (LD) calculations. The results from the Debye theory of specific heat are indicated as a horizontal dashed line (green), which corresponds to $C_v/T^3 = 0.481$ for $\Theta_d = 541.5$ K.

to the specific heat of disordered solids, the size of a model must be significantly large, of the order of at least 60,000 atoms or more [210], so that the frequencies in the vicinity of 1 THz can appear in the vibrational density of states. This explains the observed deviation of theoretical C_v values from experimental data in the vicinity of 50 K in Fig. 6.15.

6.3.5 Effects of anharmonicity on the MSD at high temperatures

We now briefly discuss the effects of anharmonicity on the MSD of atoms in a-Si at high temperatures. It goes without saying that the temperature-induced anharmonic effects at high temperatures can be truly taken into account by including thermal expansion of solids in simulations. Since the AIMD simulations presented in Sec 6.2.3 were conducted in canonical and microcanonical ensembles, where the volume expansion of a-Si was taken into account on an ad hoc basis, it is not possible to accurately address the role of anharmonicity on the MSD of atoms. Nonetheless, the results from direct AIMD simulations should provide a glimpse of the anharmonic effects on the MSD at high temperatures, as the volume-expansion factor, $\sim (1 + 3\gamma\Delta T)$, in Eq. (6.9) turns out to be very small and of the order of 1.0036 for $\Delta T = 300$ K and $\gamma = 4 \times 10^{-6}$ K^{-1} [200]. Thus, if we make allowances

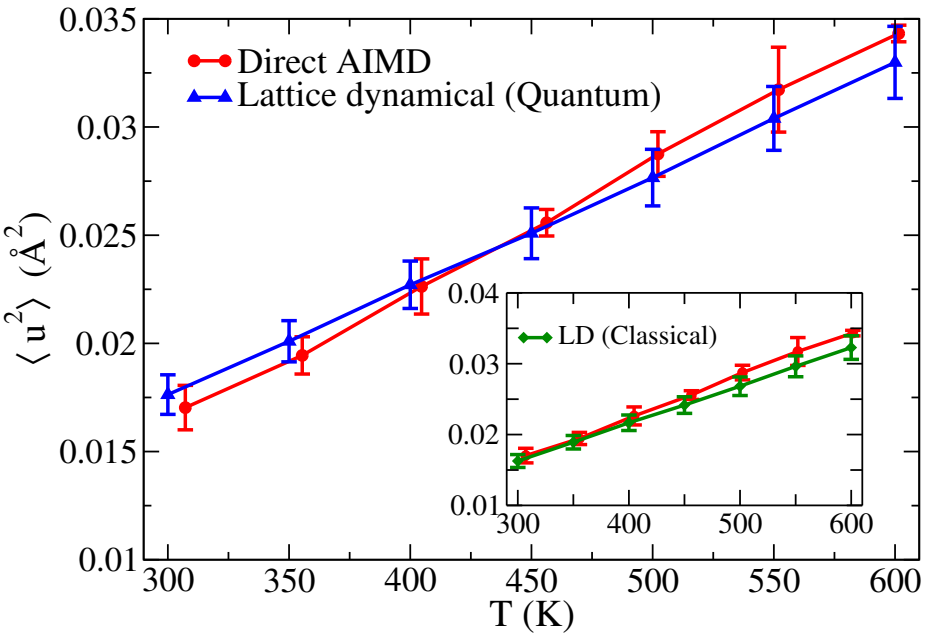

Figure 6.16: A comparison of $\langle u^2 \rangle$ obtained from 216-atom model of *a*-Si using lattice-dynamical calculations (blue) and direct AIMD simulations (red). The inset shows the results obtained by using the classical expression of energy, $\langle E_n \rangle = k_B T$ in Eq. (6.6). See section 6.3.5 for a discussion.

for not including such a small change of volume of the system, we should be able to observe the effects of temperature-induced anharmonicity on the MSD of atoms at high temperatures from direct AIMD results.

Figure 6.16 shows the results obtained from 216-atom models of *a*-Si using direct AIMD simulations in NVT and NVE ensembles, along with the results from lattice-dynamical calculations in the harmonic approximation. The results enable us to make the following remarks. First, a comparison of $\langle u^2 \rangle$ obtained from the lattice-dynamical calculations with those from direct AIMD simulations suggests that anharmonicity does not play a significant role at temperatures below 450 K. A small difference between two sets of data below 450 K can be attributed to the use of the phonon distribution function, $1/[\exp(x) - 1]$ with $x = \hbar\omega/k_B T$, in the lattice-dynamical calculations. This is apparent from the plot shown as an inset in Fig. 6.16, where the lattice-dynamical results are re-calculated in the classical limit using the value of $\langle E_n \rangle = k_B T$ in Eq. (6.6). Since the AIMD simulations are conducted by integrating the classical equations of motion, the results obtained from equilibrium atomic trajectories using Eq. (6.10) are reflective of the classical equipartition theorem. Consequently, the AIMD results are somewhat underestimated in the temperature range of 300–400 K. Second, the deviation at high temperatures, above 500 K, is likely to originate

from anharmonic effects in the dynamics. This is partly due to large thermal vibrations, which can affect the linear dependence of the forces on atomic displacements, and in part due to the defects and disorder in the amorphous network affecting force constants between neighboring atoms. Since the experimental value of the Debye temperature in *a*-Si is about 487–528 K, one may assume that the MSD of atoms can be calculated fairly accurately in the classical limit from the AIMD trajectories at temperatures above 450 K. Lastly, the use of the volume-expansion factor of $(1+3\gamma\Delta T)$ in our simulations does not yield any noticeable changes of the MSD of atoms, even at 600 K. This observation is consistent with the results observed in Fig. 6.1. It is therefore reasonable to conclude that the observed deviations of the direct AIMD results from its lattice-dynamical counterpart at high temperatures can only result from the anharmonic part of the potential in AIMD simulations.

We end this section with a brief discussion of the dependence of the MSD of atoms on the size of the basis functions and the nature of exchange-correlation (XC) approximations. Since vibrational excitations in solids typically involve energies of a few tens of meV, it is crucially important to calculate the elements of the dynamical matrix as accurately as possible by using an extended set of basis functions and a suitable XC functional appropriate for the system to be studied. To examine this issue, the MSDs of atoms in *a*-Si were calculated using both single-zeta (SZ) and double-zeta (DZ) basis functions (from SIESTA), and the local density approximation (LDA) of the XC functional and its generalized-gradient counterpart (GGA). The results of these calculations are shown in Fig. 6.17. It is evident from the plots that the use of SZ basis functions produces a somewhat larger value of $\langle u^2 \rangle$ at all temperatures compared to its DZ counterparts. By contrast, the XC approximation has little or no effect on $\langle u^2 \rangle$ values for a given basis set. A comparison of Θ_d values obtained from $\langle u^2 \rangle$ values using SZ and DZ basis functions suggests that the Θ_d value (of 541.5 K) derived from the latter matches more closely to the experimental value of 528 K. This observation is unsurprising and it is a reflection of the fact that the accuracy of the total force acting on an atom – and hence the elements of the dynamical matrix – crucially depends on the size of the basis functions used in the calculations. In view of these findings, one may conclude that the first-principles calculations of vibrational properties of amorphous solids should be studied using an extended set of basis functions, whenever possible.

6.4 Conclusions

In this paper, we have studied the Debye-Waller factor of *a*-Si using quantum-mechanical lattice-dynamical calculations in the harmonic approximation and from direct AIMD simulations that incorporate some aspects of anharmonic effects. The squared atomic displacement

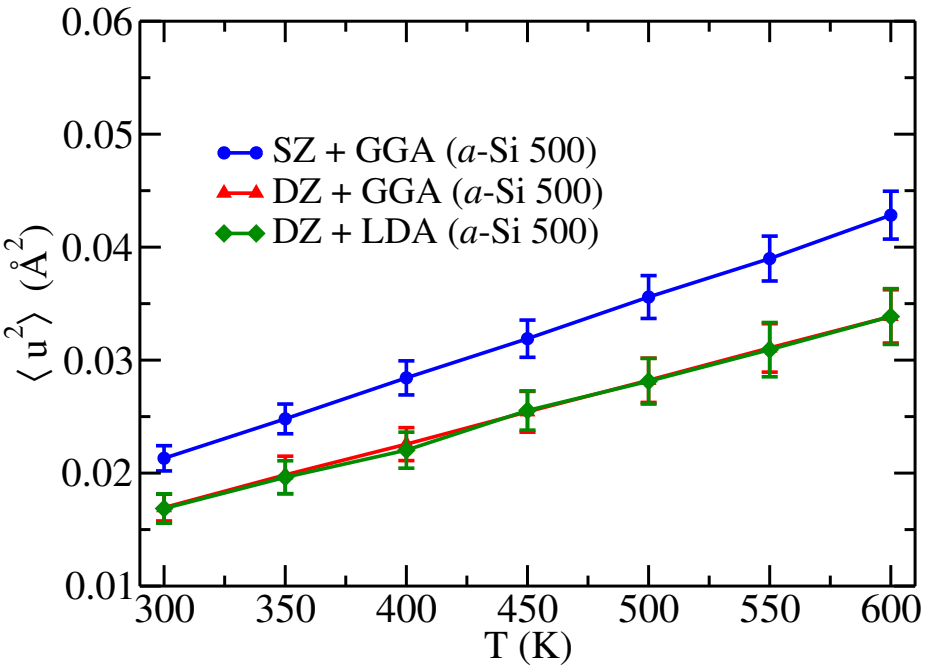

Figure 6.17: The dependence of the MSD, $\langle u^2 \rangle$, on the single- and double-zeta basis functions (SZ and DZ) and the exchange-correlation approximations (LDA and GGA) used in the DFT calculations in this study. The data correspond to the average values obtained at each temperature from two independent configurations.

(SD), u_i^2, is found to vary from site to site and that it considerably depends on the temperature and the degree of disorder in the local atomic environment of *a*-Si. In particular, it has been observed that while the distribution of the local SDs from tetrahedral sites exhibits a nearly gaussian behavior, the presence of dangling bonds and a few highly disordered sites (e.g., long Si–Si bonds) in the networks can lead to a stretched non-gaussian tail in the distribution. This non-gaussian behavior is distinctly different from that in crystals, where thermal vibrations of atoms in an ordered atomic environment give rise to a gaussian distribution in the harmonic approximation. The accuracy of the MSD values from lattice-dynamical calculations is verified by computing the Debye temperature of *a*-Si and comparing with that from experiments. The theoretical value of the Debye temperature of *a*-Si, averaged over 10–50 K, is found to be 541.5 K. This value agrees well with the experimental value of the Debye temperature, which is reported to be in the range of 487–528 K [203, 204].

A comparison of the specific heat, C_v, of *a*-Si from theory and experiments shows that the values obtained from the lattice-dynamical calculations match closely with those from experiments at temperatures from 50 K and above, but deviations occur below 50 K. A review of experimental and theoretical specific-heat data leads to the surmise that the absence of a small number of excess vibrational modes (relative to the Debye model) near 1

THz, which is often described as the boson peak in the reduced vibrational density of states of disordered solids, could be partly responsible for the deviation at low temperatures below 50 K. However, a definitive answer to this surmise is outside the scope of the present study as it requires accurate calculations of the vibrational spectra for large *a*-Si models in order to examine the vibrational modes near the 1 THz region. Such calculations are prohibitively difficult due to the requirement of using an extended set of basis functions to construct the *ab initio* force-constant matrix for *a*-Si models with several tens of thousands of atoms.

The effects of anharmonicity on atomic dynamics in *a*-Si have been studied by computing the MSD from the equilibrium trajectories of Si atoms obtained from direct AIMD simulations in microcanonical ensembles. Comparisons of results from AIMD and lattice-dynamical calculations show a small anharmonicity-induced increase of the MSD values at temperatures above 450 K. The fractional deviation of the anharmonic MSD at high temperatures from its harmonic counterpart appears to indicate that the results are qualitatively similar to those one obtains from using the quasi-harmonic approximation [202]. This suggests that the harmonic approximation works very well below 400 K, which is considerably noticeably lower than the Debye temperature of 487–528 K for *a*-Si. Finally, the Debye-Waller factor at 300 K suggests that the intensities of the first two diffraction maxima in *a*-Si, which are referred to as the FSDP and the principal peak, respectively, reduce by a factor of 0.94 and 0.8, respectively, for CuK_α X-radiation. This observation is quite important and useful in comparing the room-temperature experimental structure-factor data of *a*-Si with those from static model calculations, which do not account for thermal vibrations of atoms.

Chapter 7
SUMMARY

In this dissertation, we addressed the origin of extended-range oscillations (ERO) in amorphous silicon, using 21,952-400,000-atom models generated using WWW and MD methods from an atomistic point of view. Analysis of the partially ordered networks of Si atoms with radial ordering up to a distance of 6 Å reveals extended ordering on the network of amorphous solids as a propagation of short-range radial ordering, which can be manifest as weak oscillations in the total pair-correlation function (PCF). By comparing the extended-range oscillations of partially ordered Si networks, distorted *c*-Si systems, and large *a*-Si configurations, the radial ordering in reduced atomic pair-correlation of *a*-Si extends up to 20-30 Å. The ordering at extended-range oscillations of *a*-Si is further verified by using Shanon information and considering radial oscillations as the combination of gaussian peaks. Also, the structure factor of *a*-Si, expressed as a linear combination of Gaussian functions modulated by a sinc function indicates nearly no contribution of the ERO beyond 20 Å on the FSDP of *a*-Si. The FSDP of *a*-Si is found primarily contributed by the radial oscillations of up to 20 Å.

Considering the contribution of the radial oscillations up to 20 Å on the FSDP of *a*-Si, we then examine the origin and structure of the FSDP (First Sharp Diffraction Peak) in *a*-Si and *a*-SiO_2 with particular focus on the position, intensity, and width of the diffraction peak in the corresponding structure factor, of a monoatomic system, and reduced scattering intensity, of a binary system. For *a*-Si, the study based on the DFT relaxed models of size 216 to 6000 atoms reveals that a significant contribution to the FSDP comes from the atomic pair correlations in the second, fourth, and sixth radial shells, in addition to small residual contributions from the radial shells after that. Also, for a monoatomic covalent system, our observation suggests the minimum model size must be at least 1000 atoms or more to obtain accurate results free from any finite-size effects. Likewise, an approximate relation is obtained between the position of the FSDP and the average cubic radial distance of the atoms in the second radial shell of *a*-Si networks, suggesting a new explanation for the real-space and wavevector space structural interrelation. Direct numerical calculations confirm the results for a density of 2.15 to 2.3 $g.cm^{-3}$.

In addition, we analyzed the FSDP in the reduced scattering intensity of the *a*-SiO_2 system, consisting of 648 atoms- 216 Si and 432 O atoms. The emphasis is given to the

contribution of the radial shell correlations on the FSDP of a-SiO_2 at the vicinity of 1.5 $Å^{-1}$, the position of FSDP of binary glasses. A thorough analysis based on the impact of the radial correlations from specific regions, called radial shells, shows that the FSDP of a-SiO_2 is mostly contributed by the radial information coming from the fourth, third, sixth, and seventh shells in descending order, extended up to 6-8 Å. The contribution of real-space correlations of up to 4-8 Å are further verified using similar calculations for the partially reduced scattering intensity from Si-Si, Si-O, and O-O correlations. Rapid decreases in the intensity and nearly linearly shifted position of the FSDP are observed as indicated via diffraction experiments.

Finally, the study of atomic dynamics of Si atoms having tetrahedral bonds or incomplete (dangling) bonds is conducted in terms of the Debye-Waller factor and mean-square displacement of the Si atoms in a-Si models of size 216-500 atoms using quantum-mechanical lattice-dynamical calculations in the harmonic approximation and direct ab initio molecular dynamic simulations for anharmonic approach. Site-to-site varying atomic displacement is observed with a stretched non-gaussian tail in the distribution of atomic displacement, a behavior distinctly different from that in crystalline solids. The dynamics of atoms obtained from the lattice-dynamical calculations are validated by calculating and comparing specific heat with those from experiments at temperatures from 50 K and above. The atomic dynamics obtained from direct AIMD simulations in microcanonical ensembles indicate a minimum increase of the MSD values at temperatures above 450 K as an effect of anharmonicity. Anharmonicity-induced increase of the MSD of Si atoms is possible at temperatures above 450 K.

BIBLIOGRAPHY

[1] K. Morigaki. *Physics of Amorphous Semiconductors*. Imperial College Press, 1999.

[2] M.A. Kastner, S.R. Ovshinsky, and G.A. Thomas. *Disordered Semiconductors*. Institute for Amorphous Studies Series. Springer US, 2012.

[3] J. Singh and K. Shimakawa. *Advances in Amorphous Semiconductors*. Advances in Condensed Matter Science. CRC Press, 2003.

[4] K. Takahashi and M. Konagai. *Amorphous silicon solar cells*. New York, Wiley-Interscience, 1986.

[5] N. F. Mott and E. A. Davis. *Electronic Process in Non-Crysatalline Materials*. Clarendon Press, Oxford, 2nd edition, 1979.

[6] R. E. Hummel. *Electronic Properties of Materials*. Springer, 4th edition, 2011.

[7] A. H. Mahan, Y. Xu, B. P. Nelson, R. S. Crandall, J. D. Cohen, K. C. Palinginis, and A. C. Gallagher. Saturated defect densities of hydrogenated amorphous silicon grown by hot-wire chemical vapor deposition at rates up to 150 Å/s. *Applied Physics Letters*, 78(24):3788–3790, 2001.

[8] Rodney C. Ewing, Alkiviathes Meldrum, LuMin Wang, and ShiXin Wang. Radiation-Induced Amorphization. *Reviews in Mineralogy and Geochemistry*, 39(1):319–361, 01 2000.

[9] D. A. Drabold, P. A. Fedders, Otto F. Sankey, and John D. Dow. Molecular-dynamics simulations of amorphous si. *Phys. Rev. B*, 42:5135–5141, Sep 1990.

[10] R. Biswas, Gary S. Grest, and C. M. Soukoulis. Generation of amorphous-silicon structures with use of molecular-dynamics simulations. *Phys. Rev. B*, 36:7437–7441, Nov 1987.

[11] M.D. Rechtin, A.L. Renninger, and B.L. Averbach. Monte-carlo models of amorphous materials. *Journal of Non-Crystalline Solids*, 15(1):74–82, 1974.

[12] Roy L. Johnston. Evolving better nanoparticles: Genetic algorithms for optimising cluster geometries. *Dalton Trans.*, pages 4193–4207, 2003.

[13] Jackelyn A. Martinez, Dundar E. Yilmaz, Tao Liang, Susan B. Sinnott, and Simon R. Phillpot. Fitting empirical potentials: Challenges and methodologies. *Current Opinion in Solid State and Materials Science*, 17(6):263–270, 2013. Frontiers in Methods for Materials Simulations.

[14] John E. Fischer. Photoelectric properties of amorphous silicon and germanium films. *Thin Solid Films*, 17(2):223–229, 1973.

[15] Violetta Sessi, Maik Simon, Halid Mulaosmanovic, Darius Pohl, Markus Loeffler, Tom Mauersberger, Franz P. G. Fengler, Terence Mittmann, Claudia Richter, Stefan Slesazeck, Thomas Mikolajick, and Walter M. Weber. A silicon nanowire ferroelectric field-effect transistor. *Advanced Electronic Materials*, 6(4):1901244, 2020.

[16] W.E. Spear and P.G. Le Comber. Substitutional doping of amorphous silicon. *Solid State Communications*, 17(9):1193 – 1196, 1975.

[17] J. Abelson. Photoconductivity of hydrogenated amorphous silicon. *Journal of Non-Crystalline Solids*, 114:450 – 452, 1989. Proceedings of the Thirteenth International Conference on Amorphous and Liquid Semiconductors.

[18] R.J. Loveland, W.E. Spear, and A. Al-Sharbaty. Photoconductivity and absorption in amorphous Si. *Journal of Non-Crystalline Solids*, 13(1):55 – 68, 1973.

[19] M. J. Powell. The physics of amorphous-silicon thin-film transistors. *IEEE Transactions on Electron Devices*, 36(12):2753–2763, Dec 1989.

[20] A. V. Emelyanov, M. V. Khenkin, A. G. Kazanskii, P. A. Forsh, P. K. Kashkarov, M. Gecevicius, M. Beresna, and P. G. Kazansky. Femtosecond laser induced crystallization of hydrogenated amorphous silicon for photovoltaic applications. *Thin Solid Films*, 556:410 – 413, 2014.

[21] H. O. Jacobs, A. R. Tao, A. Schwartz, D. H. Gracias, and G. M. Whitesides. Fabrication of a cylindrical display by patterned assembly. *Science*, 296:323–325, 12 2002. 785.

[22] N. Asada, M. Takeuchi, V. Vaganov, N. Belov, S. in't Hout, and I. Sluchak. Silicon micro-optical scanner. *Sensors and Actuators A: Physical*, 83(1):284 – 290, 2000.

[23] W.E. Spear. The study of transport and related properties of amorphous silicon by transient experiments. *Journal of Non-Crystalline Solids*, 59-60:1 – 13, 1983. Proceedings of the Tenth International Conference on Amorphous and Liquid Semiconductors.

[24] Annett Thøgersen, Spyros Diplas, Jeyanthinath Mayandi, Terje Finstad, Arne Olsen, John F. Watts, Masanori Mitome, and Yoshio Bando. An experimental study of charge distribution in crystalline and amorphous si nanoclusters in thin silica films. *Journal of Applied Physics*, 103(2):024308, 2008.

[25] R. Car and M. Parrinello. Structural, dymanical, and electronic properties of amorphous silicon: An ab initio molecular-dynamics study. *Phys. Rev. Lett.*, 60:204–207, Jan 1988.

[26] F. Wooten, K. Winer, and D. Weaire. Computer generation of structural models of amorphous Si and Ge. *Phys. Rev. Lett.*, 54:1392, 1985.

[27] Khalid Laaziri, S. Kycia, S. Roorda, M. Chicoine, J. L. Robertson, J. Wang, and S. C. Moss. High resolution radial distribution function of pure amorphous silicon. *Phys. Rev. Lett.*, 82:3460–3463, Apr 1999.

[28] K. Laaziri, S. Kycia, S. Roorda, M. Chicoine, J. L. Robertson, J. Wang, and S. C. Moss. High-energy x-ray diffraction study of pure amorphous silicon. *Phys. Rev. B*, 60:13520, 1999.

[29] J. Fortner and J. S. Lannin. Radial distribution functions of amorphous silicon. *Phys. Rev. B*, 39:5527, 1989.

[30] D.E. Polk. Structural model for amorphous silicon and germanium. *Journal of Non-Crystalline Solids*, 5(5):365–376, 1971.

[31] G. A. N. Connell and R. J. Temkin. Modeling the structure of amorphous tetrahedrally coordinated semiconductors. i. *Phys. Rev. B*, 9:5323–5326, Jun 1974.

[32] D. E. Polk and D. S. Boudreaux. Tetrahedrally coordinated random-network structure. *Phys. Rev. Lett.*, 31:92–95, Jul 1973.

[33] Paul Steinhardt, Richard Alben, M. G. Duffy, and D. E. Polk. Relaxed continuous-random-network models. *Phys. Rev. B*, 8:6021–6023, Dec 1973.

[34] P. N. Keating. Effect of invariance requirements on the elastic strain energy of crystals with application to the diamond structure. *Phys. Rev.*, 145:637, 1966.

[35] Douglas Henderson and Frank Herman. Simulation of the atomic arrangements in amorphous silicon and germanium. *Journal of Non-Crystalline Solids*, 8-10:359–363, 1972. Amorphous and Liquid Semiconductors.

[36] Kléman, M. and Sadoc, J.F. A tentative description of the crystallography of amorphous solids. *J. Physique Lett.*, 40(21):569–574, 1979.

[37] F. Wooten and D. Weaire. Modeling tetrahedrally bonded random networks by computer. In Henry Ehrenreich and David Turnbull, editors, *Solid State Physics*, volume 40, pages 1–42. Academic Press, 1987.

[38] G. T. Barkema and N. Mousseau. High-quality continuous random networks. *Phys. Rev. B*, 62:4985, 2000.

[39] R. L. C. Vink, G. T. Barkema, M. A. Stijnman, and R. H. Bisseling. Device-size atomistic models of amorphous silicon. *Phys. Rev. B*, 64:245214, Dec 2001.

[40] Raymond Atta-Fynn and Parthapratim Biswas. Nearly defect-free dynamical models of disordered solids: The case of amorphous silicon. *The Journal of Chemical Physics*, 148(20):204503, 2018.

[41] Devilal Dahal, Raymond Atta-Fynn, S. R. Elliott, and Parthapratim Biswas. Hyperuniformity and static structure factor of amorphous silicon in the infinite-wavelength limit. *Journal of Physics: Conference Series*, 1252(1):012003, jun 2019.

[42] N.C. Cooper, C.M. Goringe, and D.R. McKenzie. Density functional theory modelling of amorphous silicon. *Computational Materials Science*, 17(1):1–6, 2000.

[43] Eunja Kim and Young Hee Lee. Structural, electronic, and vibrational properties of liquid and amorphous silicon: Tight-binding molecular-dynamics approach. *Phys. Rev. B*, 49:1743–1749, Jan 1994.

[44] R. L. McGreevy and L. Pusztai. Reverse monte carlo simulation: A new technique for the determination of disordered structures. *Molecular Simulation*, 1(6):359–367, 1988.

[45] Parthapratim Biswas, Raymond Atta-Fynn, and D. A. Drabold. Reverse monte carlo modeling of amorphous silicon. *Phys. Rev. B*, 69:195207, May 2004.

[46] A. K. Soper. Partial structure factors from disordered materials diffraction data: An approach using empirical potential structure refinement. *Phys. Rev. B*, 72:104204, Sep 2005.

[47] A. Pandey, Parthapratim Biswas, and D. A. Drabold. Force-enhanced atomic refinement: Structural modeling with interatomic forces in a reverse monte carlo approach applied to amorphous si and sio_2. *Phys. Rev. B*, 92:155205, Oct 2015.

[48] Dil K. Limbu, Stephen R. Elliott, Raymond Atta-Fynn, and Parthapratim Biswas. Disorder by design: A data-driven approach to amorphous semiconductors without total-energy functionals. *Sci. Rep.*, 10:7742, 2020.

[49] D. K. Limbu, R. Atta-Fynn, D. A. Drabold, Stephen R. Elliott, and Parthapratim Biswas. Information-driven inverse approach to disordered solids: Applications to amorphous silicon. *Phys. Rev. Materials*, 2:115602, 2018.

[50] B. E. Warren and J. Biscce. The structure of silica glass by x-ray diffraction studies *. *Journal of the American Ceramic Society*, 21(2):49–54, 1938.

[51] Adrian C. Wright. Neutron scattering from vitreous silica. v. the structure of vitreous silica: What have we learned from 60 years of diffraction studies? *Journal of Non-Crystalline Solids*, 179:84–115, 1994. Proceedings of the First PAC RIM Meeting on Glass and Optical Materials.

[52] K. Andreev, V. Tadaion, Q. Zhu, W. Wang, Y. Yin, and T. Tonnesen. Thermal and mechanical cyclic tests and fracture mechanics parameters as indicators of thermal shock resistance – case study on silica refractories. *Journal of the European Ceramic Society*, 39(4):1650–1659, 2019.

[53] Preeti S. Shinde, Pradnya S. Suryawanshi, Kanchan K. Patil, Vedika M. Belekar, Sandeep A. Sankpal, Sagar D. Delekar, and Sushilkumar A. Jadhav. A brief overview of recent progress in porous silica as catalyst supports. *Journal of Composites Science*, 5(3), 2021.

[54] T. Aiyama, T. Fukunaga, K. Niihara, T. Hirai, and K. Suzuki. An x-ray diffraction study of the amorphous structure of chemically vapor-deposited silicon nitride. *Journal of Non-Crystalline Solids*, 33(2):131–139, 1979.

[55] H.F. Poulsen, J. Neuefeind, H.-B. Neumann, J.R. Schneider, and M.D. Zeidler. Amorphous silica studied by high energy x-ray diffraction. *Journal of Non-Crystalline Solids*, 188(1):63–74, 1995.

[56] A. Howie. High resolution electron microscopy of amorphous thin films. *Journal of Non-Crystalline Solids*, 31(1):41–55, 1978. Proceedings of the Topical Conference on Atomic Scale Structure of Amorphous Solids.

[57] Peter A.V. Johnson, Adrian C. Wright, and Roger N. Sinclair. Neutron scattering from vitreous silica ii. twin-axis diffraction experiments. *Journal of Non-Crystalline Solids*, 58(1):109–130, 1983.

[58] P. H. Gaskell and D. J. Wallis. Medium-range order in silica, the canonical network glass. *Phys. Rev. Lett.*, 76:66, 1996.

[59] J. K. Christie, S. N. Taraskin, and S. R. Elliott. Structural characteristics of positionally disordered lattices: Relation to the first sharp diffraction peak in glasses. *Phys. Rev. B*, 70:134207, Oct 2004.

[60] S. Susman, D.L. Price, K.J. Volin, R.J. Dejus, and D.G. Montague. Intermediate-range order in binary chalcogenide glasses: The first sharp diffraction peak. *J. Non-Cryst. Solids*, 106:26, 1988.

[61] S. R. Elliott. Medium range structural order in covalent amorphous solids. *Nature*, 354:445, 1991.

[62] S. Susman, D.L. Price, K.J. Volin, R.J. Dejus, and D.G. Montague. Intermediate-range order in binary chalcogenide glasses: The first sharp diffraction peak. *Journal of Non-Crystalline Solids*, 106(1):26–29, 1988.

[63] Philip S. Salmon. Real space manifestation of the first sharp diffraction peak in the structure factor of liquid and glassy materials. *Proceedings of the Royal Society of London. Series A: Mathematical and Physical Sciences*, 445(1924):351–365, 1994.

[64] J. Du and L. R. Corrales. Compositional dependence of the first sharp diffraction peaks in alkali silicate glasses: A molecular dynamics study. *J. Non-Cryst. Solids*, 352:3255, 2006.

[65] J. H. Lee and S. R. Elliott. Simulations of void-filled vitreous silica to interpret the origin of the first sharp diffraction peak. *Phys. Rev. B*, 50:5981–5987, Sep 1994.

[66] Mark Wilson and Paul A. Madden. Voids, layers, and the first sharp diffraction peak in $zncl_2$. *Phys. Rev. Lett.*, 80:532–535, Jan 1998.

[67] Y Inamura, Y Katayama, and W Utsumi. Transformation in intermediate-range structure of vitreous silica under high pressure and temperature. *J. Phys.: Condens. Matter*, 19:415104, 2007.

[68] Y. Inamura, M. Arai, N. Kitamura, S.M. Bennington, and A.C. Hannon. Intermediate-range structure and low-energy dynamics of densified sio2 glass. *Phys. B*, 241-243:903, 1997.

[69] Devilal Dahal, Hiroka Warren, and Parthapratim Biswas. On the origin and structure of the first sharp diffraction peak of amorphous silicon. *physica status solidi (b)*, 258(9):2000447, 2021.

[70] A. Uhlherr and S. R. Elliott. Generation of the first sharp diffraction peak by extended-range ordering of atoms and voids in amorphous silicon. *Philos. Mag. B*, 71:611, 1995.

[71] Rui Shi and Hajime Tanaka. Distinct signature of local tetrahedral ordering in the scattering function of covalent liquids and glasses. *Science Advances*, 5(3):eaav3194, 2019.

[72] Devilal Dahal, Stephen R. Elliott, and Parthapratim Biswas. Extended-range order in tetrahedral amorphous semiconductors: The case of amorphous silicon. *Phys. Rev. B*, 105:115203, Mar 2022.

[73] W. H. Zachariasen. The atomic arrangement in glass. *Journal of the American Chemical Society*, 54(10):3841–3851, 1932.

[74] Loup Verlet. Computer "experiments" on classical fluids. i. thermodynamical properties of lennard-jones molecules. *Phys. Rev.*, 159:98–103, Jul 1967.

[75] D. Frenkel and B. Smit. *Understanding Molecular Simulation: From Algorithms to Applications*. Computational science. Elsevier Science, 2001.

[76] F. H. Stillinger and T. A. Weber. Computer simulation of local order in condensed phases of silicon. *Phys. Rev. B*, 31:5262, 1985.

[77] Jahlani I. Odujole and Salil Desai. Molecular dynamics investigation of material deformation behavior of pmma in nanoimprint lithography. *AIP Advances*, 10(9):095102, 2020.

[78] W.L. Dunn and J.K. Shultis. *Exploring Monte Carlo Methods*. Elsevier Science, 2011.

[79] I.M. Sobol. *A Primer for the Monte Carlo Method*. Taylor & Francis, 1994.

[80] S. Brooks, A. Gelman, G. Jones, and X.L. Meng. *Handbook of Markov Chain Monte Carlo*. Chapman & Hall/CRC Handbooks of Modern Statistical Methods. CRC Press, 2011.

[81] P. Hohenberg and W. Kohn. Inhomogeneous electron gas. *Phys. Rev.*, 136:B864–B871, Nov 1964.

[82] W. Kohn and L. J. Sham. Self-consistent equations including exchange and correlation effects. *Phys. Rev.*, 140:A1133–A1138, Nov 1965.

[83] Eric J. Bylaska. Plane-wave dft methods for chemistry. In David A. Dixon, editor, *Annual Reports in Computational Chemistry*, volume 13, pages 185–228. Elsevier, 2017.

[84] D R Bowler and T Miyazaki. methods in electronic structure calculations. *Reports on Progress in Physics*, 75(3):036503, feb 2012.

[85] J. P. Perdew and Alex Zunger. Self-interaction correction to density-functional approximations for many-electron systems. *Phys. Rev. B*, 23:5048, 1981.

[86] John P. Perdew, Kieron Burke, and Matthias Ernzerhof. Generalized gradient approximation made simple. *Phys. Rev. Lett.*, 77:3865, 1996.

[87] S. R. Elliott. *Physics of Amorphous Materials*. Longman, London, 2nd edition, 1990.

[88] S. V. King. Ring configurations in a random network model of vitreous silica. *Nature*, 213:1112–1113, 1967.

[89] Lester Guttman. Ring structure of the crystalline and amorphous forms of silicon dioxide. *Journal of Non-Crystalline Solids*, 116(2):145–147, 1990.

[90] Sébastien Le Roux and Philippe Jund. Ring statistics analysis of topological networks: New approach and application to amorphous ges2 and sio2 systems. *Computational Materials Science*, 49(1):70–83, 2010.

[91] Gilles Horowitz. Validity of the concept of band edge in organic semiconductors. *Journal of Applied Physics*, 118(11):115502, 2015.

[92] F. Bloch. Uber die quantenmechanik der elektronen in kristallgittern. *Zeitschrift fur Physik*, 52:555, 1929.

[93] M. Born and R. Oppenheimer. Zur quantentheorie der molekeln. *Annalen der Physik*, 389(20):457–484, 1927.

[94] Max Born and Kun Huang. Dynamical theory of crystal lattices. *American Journal of Physics*, 23(7):474–474, 1955.

[95] Ricardo A. Broglia, Gianluca Colò, Giovanni Onida, and H. Eduardo Roman. *Phonons: Harmonic Approximation*, pages 105–130. Springer Berlin Heidelberg, 2004.

[96] W. H. Zachariasen. The atomic arrangement in glass. *J. Am. Chem. Soc.*, 54:3841, 1932.

[97] Parthapratim Biswas, Durga Paudel, Raymond Atta-Fynn, and Stephen R. Elliott. Temperature-induced nanostructural evolution of hydrogen-rich voids in amorphous silicon: a first-principles study. *Nanoscale*, 12:1464–1477, 2020.

[98] P Biswas and S R Elliott. Nanoscale structure of microvoids in a-si:h: a first-principles study. *J. Phys.: Condens. Matter*, 27:435201, oct 2015.

[99] J. M. Gibson and M. M. J. Treacy. Diminished medium-range order observed in annealed amorphous germanium. *Phys. Rev. Lett.*, 78:1074–1077, Feb 1997.

[100] A. Uhlherr and S. R. Elliott. Extended-range propagated order in amorphous solids. *J. Phys.: Condens. Matter*, 6:L99, 1994.

[101] R. Xie, G. G. Long, S. J. Weigand, S. C. Moss, T. Carvalho, S. Roorda, M. Hejna, S. Torquato, and P. J. Steinhardt. Hyperuniformity in amorphous silicon based on the measurement of the infinite-wavelength limit of the structure factor. *Proc. Natl. Acad. Sci.*, 110:13250, 2013.

[102] M Aniya and F Shimojo. Medium range order in oxide and chalcogenide superionic glasses: A comparative study by using the average electronegativity. *Journal of Non-Crystalline Solids*, 341(1):110–114, 2004.

[103] Badri Shyam, Kevin H. Stone, Riccardo Bassiri, Martin M. Fejer, Michael F. Toney, and Apurva Mehta. Measurement and modeling of short and medium range order in amorphous ta_2o_5 thin films. *Scientific Reports*, 6:32170, 2016.

[104] Q. Mei, C. J. Benmore, S. Sen, R. Sharma, and J. L. Yarger. Intermediate range order in vitreous silica from a partial structure factor analysis. *Phys. Rev. B*, 78:144204, Oct 2008.

[105] Philip S. Salmon, Adrian C. Barnes, Richard A. Martin, and Gabriel J. Cuello. Glass fragility and atomic ordering on the intermediate and extended range. *Phys. Rev. Lett.*, 96:235502, Jun 2006.

[106] S. Sampath, C. J. Benmore, K. M. Lantzky, J. Neuefeind, K. Leinenweber, D. L. Price, and J. L. Yarger. Intermediate-range order in permanently densified geo_2 glass. *Phys. Rev. Lett.*, 90:115502, 2003.

[107] P. Vashishta, Rajiv K. Kalia, Giomal A. Antonio, and I. Ebbsjö. Atomic correlations and intermediate-range order in molten and amorphous $gese_2$. *Phys. Rev. Lett.*, 62:1651, 1989.

[108] J.C. Phillips. Topology of covalent non-crystalline solids ii: Medium-range order in chalcogenide alloys and *a*-si(ge). *J. Non-Cryst. Solids*, 43:37, 1981.

[109] G. Lucovsky. Specification of medium range order in amorphous materials. *Journal of Non-Crystalline Solids*, 97-98:155–158, 1987. Amorphous and liquid semiconductors.

[110] H. Iyetomi, P. Vashishta, and R. K. Kalia. Integral-equation approach to medium-range order in molten and glassy chalcogenides. *Phys. Rev. B*, 43:1726–1734, Jan 1991.

[111] P. Armand, A. Ibanez, E. Philippot, Q. Ma, and D. Raoux. Local and medium range order in germanium chalcogenide glasses. *Journal of Non-Crystalline Solids*, 150(1):371–375, 1992. Proceedings of the Fifth International Conference on the structure of Non-Crystalline Materials (NCM 5).

[112] H. W. Sheng, W. K. Luo, F. M. Alamgir, J. M. Bai, and E. Ma. Atomic packing and short-to-medium-range order in metallic glasses. *Nature*, pages 419–425, 2006.

[113] Yao Yang, Jihan Zhou, Fan Zhu, Yakun Yuan, Dillan J. Chang, Dennis S. Kim, Minh Pham, Arjun Rana, Xuezeng Tian, Yonggang Yao, Stanley J. Osher, Andreas K. Schmid, Liangbing Hu, Peter Ercius, and Jianwei Miao. Determining the three-dimensional atomic structure of an amorphous solid. *Nature*, 592:60–64, 2021.

[114] D. Ma, A. Stoica, and XL. Wang. Power-law scaling and fractal nature of medium-range order in metallic glasses. *Nature Materials*, 8:30–34, 2009.

[115] L. Cormier, P. H. Gaskell, G. Calas, and A. K. Soper. Medium-range order around titanium in a silicate glass studied by neutron diffraction with isotopic substitution. *Phys. Rev. B*, 58:11322–11330, Nov 1998.

[116] Philip S Salmon. The structure of tetrahedral network glass forming systems at intermediate and extended length scales. *Journal of Physics: Condensed Matter*, 19(45):455208, oct 2007.

[117] Sukti Hazra, Isao Sakata, Mitsuyuki Yamanaka, and Eiichi Suzuki. Evolution of an amorphous silicon network from silicon paracrystallites studied by spectroscopic ellipsometry. *Phys. Rev. B*, 69:235204, Jun 2004.

[118] A. Hirata, P. Guan, T. Fujita, Y. Hirotsu, A. Inoue, A. R. Yavari, T. Sakurai, and M. Chen. Direct observation of local atomic order in a metallic glass. *Nature Materials*, 10:28–33, 2011.

[119] Bevan K. Sharma and Mark Wilson. Intermediate-range order in molten network-forming systems. *Phys. Rev. B*, 73:060201, Feb 2006.

[120] Keiji Tanaka. Medium-range structure in chalcogenide glasses. *Japanese Journal of Applied Physics*, 37(4R):1747, apr 1998.

[121] Kengo Nishio, Takehide Miyazaki, and Hisao Nakamura. Universal medium-range order of amorphous metal oxides. *Phys. Rev. Lett.*, 111:155502, Oct 2013.

[122] V. L. Deringer, N. Bernstein, G. Csányi, C. Ben M., M. Ceriotti, M. Wilson, D. A. Drabold, and S. R. Elliott. Origins of structural and electronic transitions in disordered silicon. *Nature*, 589:59–64, 2021.

[123] J M Holender and G J Morgan. Generation of a large structure (105atoms) of amorphous si using molecular dynamics. *J. Phys.: Condens. Matter*, 3:7241, 1991.

[124] S. Roorda, C. Martin, M. Droui, M. Chicoine, A. Kazimirov, and S. Kycia. Disentangling neighbors and extended range density oscillations in monatomic amorphous semiconductors. *Phys. Rev. Lett.*, 108:255501, Jun 2012.

[125] J. S. Custer, Michael O. Thompson, D. C. Jacobson, J. M. Poate, S. Roorda, W. C. Sinke, and F. Spaepen. Density of amorphous si. *Appl. Phys. Lett.*, 64:437, 1994.

[126] R. L. C. Vink, G. T. Barkema, and W. F. van der Weg. Raman spectra and structure of amorphous si. *Phys. Rev. B*, 63:115210, 2001.

[127] S. Nosé. A unified formulation of the constant temperature molecular dynamics methods. *J. Chem. Phys.*, 81:511, 1984.

[128] W. G. Hoover. Canonical dynamics: Equilibrium phase-space distributions. *Phys. Rev. A*, 31:1695, 1985.

[129] R. Atta-Fynn and P. Biswas. Nearly defect-free dynamical models of disordered solids: The case of amorphous silicon. *J. Chem. Phys.*, 148:204503, 2018.

[130] Werner Weber. Adiabatic bond charge model for the phonons in diamond, si, ge, and $\alpha - \mathrm{Sn}$. *Phys. Rev. B*, 15:4789, May 1977.

[131] R Haydock, V Heine, and M J Kelly. Electronic structure based on the local atomic environment for tight-binding bands. *Journal of Physics C: Solid State Physics*, 5(20):2845, oct 1972.

[132] R. Haydock. Solid state physics. In H. Ehrenreich, D. Turnbull, and F. Seitz, editors, *Characterization of Materials*, volume 35 of *Solid State Physics*, pages 216–287. Academic Press, 1980.

[133] In the recursion method, the diagonal element of $\hat{G}(z)$ is computed by transforming the tight-binding H matrix into a tridiagonal form using the Lanczos algorithm and expressing the element as a continued fraction. The coefficients of the continued fraction are determined by the diagonal and off-diagonal elements of the tridiagonal matrix, and a suitable terminator scheme, which preserves the analytic properties of $\hat{G}(z)$, is used to evaluate the continued fraction.

[134] Parthapratim Biswas. Vibrational properties of amorphous silicon from tight-binding $o(n)$ calculations. *Phys. Rev. B*, 65:125208, Mar 2002.

[135] The Fisher-Pearson coefficient of skewness of a distribution, p(x), is expressed as the standardized third central moment, $E\left[((x-\mu_1)/\nu)^3\right]$, where μ_n is the conventional n^{th} moment and $\nu^2 = \mu_2 - {\mu_1}^2$ of p(x). For samples of finite size, n, one often multiplies by a scale factor of $\sqrt{n(n-1)}/(n-2)$ to obtain the adjusted Fisher-Pearson coefficient. The value of the adjusted coefficient is reported in this study.

[136] C. E. Shannon. A mathematical theory of communication. *The Bell System Technical Journal*, 27(3):379–423, 1948.

[137] R. A. Fisher. *Statistical Methods, Experimental Design, and Scientific Inference*. Oxford University Press, Oxford, 1959.

[138] The covariance is expressed as the average cross product between two variables. One often uses M-k instead of M in the denominator of Eq.(5). However, this does not affect the results for $n \ll M$.

[139] Owing to the stochastic nature of the minimization problem in fitting Eq. (6) with simulated G(r) of *a*-Si, we have used here 20 independent sets of Gaussian parameters, (ai, bi, ci), to obtain a robust estimate of the average value of ε.

[140] Philip S. Salmon, Richard A. Martin, Philip E. Mason, and Gabriel J. Cuello. Topological versus chemical ordering in network glasses at intermediate and extended length scales. *Nature*, 435(7038), 2005.

[141] G. D' Angelo, C. Crupi, M. Á. González, E. Basile, V. C. Nibali, and C. Mondelli. Prepeak and first sharp diffraction peak in the structure factor of $(Cs_2O)_{0.14}(B_2O_3)_{0.86}$ glass: Influence of temperature. *J. Phys. Chem. B*, 114:12565, 2010.

[142] S.R. Elliott. Extended-range order, interstitial voids and the first sharp diffraction peak of network glasses. *J. Non-Cryst. Solids*, 182:40, 1995.

[143] C. Crupi, G. Carini, G. Ruello, and G. D'Angelo. Intermediate range order in alkaline borate glasses. *Philos. Mag.*, 96:788, 2016.

[144] E. Bychkov, C. J. Benmore, and D. L. Price. Compositional changes of the first sharp diffraction peak in binary selenide glasses. *Phys. Rev. B*, 72:172107, 2005.

[145] O. Uemura, Y. Sagara, and T. Satow. The neutron diffraction study of amorphous gese2. *Phys. Status Solidi A*, 32:K91, 1975.

[146] D.L. Price, S. Susman, K.J. Volin, and R.J. Dejus. Intermediate-range order in binary and ternary glasses. *Phys. B*, 156-157:189, 1989.

[147] L. E. Busse and S. R. Nagel. Temperature dependence of the structure factor of as_2se_3 glass up to the glass transition. *Phys. Rev. Lett.*, 47:1848, 1981.

[148] P. Armand, A. Ibanez, Q. Ma, D. Raoux, and E. Philippot. Structural characterization of germanium selenide glasses by differential anomalous x-ray scattering. *J. Non-Cryst. Solids*, 167:37, 1994.

[149] S. Susman, K. J. Volin, D. G. Montague, and D. L. Price. Temperature dependence of the first sharp diffraction peak in vitreous silica. *Phys. Rev. B*, 43:11076, 1991.

[150] J.H. Lee and S.R. Elliott. Simulation evidence for the origin of the first sharp diffraction peak. *J. Non-Cryst. Solids*, 192-193:133 – 136, 1995. Structure of Non-Crystalline Materials 6.

[151] P. Debye. Interferenz von röntgenstrahlen und wärmebewegung. *Ann. Phys.*, 348:49, 1913.

[152] The effect of temperature on the structure factor of polycrystalline and disordered aggregates can be rather complicated due to the presence of attendant thermal diffuse scattering, which originates from the self-scattering of an atom with respect to itself. Here, we refer to the effect of the Debye-Waller factor, which simply dampens the Bragg peaks of crystalline samples at high temperature.

[153] S. Susman, K. J. Volin, D. L. Price, M. Grimsditch, J. P. Rino, R. K. Kalia, P. Vashishta, G. Gwanmesia, Y. Wang, and R. C. Liebermann. Intermediate-range order in permanently densified vitreous sio_2: A neutron-diffraction and molecular-dynamics study. *Phys. Rev. B*, 43:1194, 1991.

[154] O Pilla, L Angelani, A Fontana, J R Gonçalves, and G Ruocco. Structural and dynamical consequences of density variation in vitreous silica. *J. Phys.: Condens. Matter*, 15:S995, 2003.

[155] G. Lucovsky and J. C. Phillips. Nano-regime length scales extracted from the first sharp diffraction peak in non-crystalline sio2 and related materials: Device applications. *Nanoscale Res. Lett.*, 5:550, 2010.

[156] J. Du and L. R. Corrales. First sharp diffraction peak in silicate glasses: Structure and scattering length dependence. *Phys. Rev. B*, 72:092201, 2005.

[157] An alternative approach to generate a 4-fold-coordinated disordered network is to employ the reverse Monte Carlo (RMC) approach using a suitable cost function. The resulting tetravalent network can be used as a starting configuration for the WWW bond switches between atoms.

[158] Nicholas Metropolis, Arianna W. Rosenbluth, Marshall N. Rosenbluth, Augusta H. Teller, and Edward Teller. Equation of state calculations by fast computing machines. *The Journal of Chemical Physics*, 21(6):1087–1092, 1953.

[159] José M Soler, Emilio Artacho, Julian D Gale, Alberto García, Javier Junquera, Pablo Ordejón, and Daniel Sánchez-Portal. The SIESTA method for ab initio order-n materials simulation. *J. Phys.: Condens. Matter*, 14:2745, 2002.

[160] J. Harris. Simplified method for calculating the energy of weakly interacting fragments. *Phys. Rev. B*, 31:1770, 1985.

[161] D. Beeman, R. Tsu, and M. F. Thorpe. Structural information from the raman spectrum of amorphous silicon. *Phys. Rev. B*, 32:874, 1985.

[162] R. Atta-Fynn and P. Biswas. Nearly defect-free dynamical models of disordered solids: The case of amorphous silicon. *J. Chem. Phys.*, 148:204503, 2018.

[163] Volker L. Deringer, Noam Bernstein, Albert P. Bartók, Matthew J. Cliffe, Rachel N. Kerber, Lauren E. Marbella, Clare P. Grey, Stephen R. Elliott, and Gábor Csányi. Realistic atomistic structure of amorphous silicon from machine-learning-driven molecular dynamics. *J. Phys. Chem. Lett.*, 9:2879, 2018.

[164] The positions of the maxima of $\sin(x)/x$ asymptotically converge to $(4m+1)\pi/2$, where m is a positive integer. The first four positions of the maxima of $\sin(x)/x$, for $x \geq 0$, are given by x=0, 7.725, 14.065, and 20.37. The corresponding values for $\sin(x)$ are at x=1.570 ($\pi/2$), 7.853 ($5\pi/2$), 14.137 ($9\pi/2$), and 20.420 ($13\pi/2$). This also explains why m=0 does not provide a physical solution (as it corresponds to $Qr = 0$).

[165] A. Fischer-Colbrie, A. Bienenstock, P. H. Fuoss, and Matthew A. Marcus. Structure and bonding in photodiffused amorphous ag-gese$_2$ thin films. *Phys. Rev. B*, 38:12388–12403, Dec 1988.

[166] C.Z Tan and J Arndt. X-ray diffraction of densified silica glass. *Journal of Non-Crystalline Solids*, 249(1):47–50, 1999.

[167] Sherman Susman, Kenneth J. Volin, Daniel G. Montague, and David L. Price. Temperature dependence of the first sharp diffraction peak in vitreous silica. *Phys. Rev. B*, 43:11076–11081, May 1991.

[168] P. Vashishta, Rajiv K. Kalia, José P. Rino, and Ingvar Ebbsjö. Interaction potential for sio$_2$: A molecular-dynamics study of structural correlations. *Phys. Rev. B*, 41:12197–12209, Jun 1990.

[169] Johannes Sarnthein, Alfredo Pasquarello, and Roberto Car. Structural and electronic properties of liquid and amorphous sio$_2$: An ab initio molecular dynamics study. *Phys. Rev. Lett.*, 74:4682–4685, Jun 1995.

[170] S R Elliott. The origin of the first sharp diffraction peak in the structure factor of covalent glasses and liquids. *J. Phys.: Condens. Matter*, 4:7661, 1992.

[171] T. Uchino, J. D. Harrop, S. N. Taraskin, and S. R. Elliott. Real and reciprocal space structural correlations contributing to the first sharp diffraction peak in silica glass. *Phys. Rev. B*, 71:014202, 2005.

[172] De Nyago Tafen and D. A. Drabold. Realistic models of binary glasses from models of tetrahedral amorphous semiconductors. *Phys. Rev. B*, 68:165208, Oct 2003.

[173] O. V. Mazurin, M. V. Streltsina, and T. P Shvaiko-Shvaikovskaya. *Handbook of Glass Data Part A: Silica Glass and Binary Silicate Glasses;*. Elsevier, Amsterdam, 1983.

[174] T. E. Faber and J. M. Ziman. A theory of the electrical properties of liquid metals. *The Philosophical Magazine: A Journal of Theoretical Experimental and Applied Physics*, 11(109):153–173, 1965.

[175] J. R. G. Da Silva, D. G. Pinatti, C. E. Anderson, and M. L. Rudee. A refinement of the structure of vitreous silica. *The Philosophical Magazine: A Journal of Theoretical Experimental and Applied Physics*, 31(3):713–717, 1975.

[176] R. L. Mozzi and B. E. Warren. The structure of vitreous silica. *Journal of Applied Crystallography*, 2(4):164–172, Oct 1969.

[177] Aiichiro Nakano, Rajiv K. Kalia, and Priya Vashishta. First sharp diffraction peak and intermediate-range order in amorphous silica: finite-size effects in molecular dynamics simulations. *J. Non-Cryst. Solids*, 171:157, 1994.

[178] J Horbach. Molecular dynamics computer simulation of amorphous silica under high pressure. *Journal of Physics: Condensed Matter*, 20(24):244118, may 2008.

[179] Hilding Faxén. Die bei interferenz von röntgenstrahlen infolge der wärmebewegung entstehende streustrahlung. *Zeitschrift für Physik*, 17(1):266–278, 1923.

[180] Ivar Waller. Zur frage der einwirkung der wärmebewegung auf die interferenz von röntgenstrahlen. *Zeitschrift für Physik*, 17(1):398–408, 1923.

[181] H. Ott. Der einfluß der temperatur auf die röntgenstreuung fester körper nach der quantenmechanik. *Annalen der Physik*, 415(2):169–196, 1935.

[182] Max Born. Theoretical investigations on the relation between crystal dynamics and x-ray scattering. *Reports on Progress in Physics*, 9(1):294–333, jan 1942.

[183] The Debye-Waller factor depends on the elemental species (k) of an atom and it is often written as the square of the temperature factor $T_k(\mathbf{Q}) = \exp(-M_k) = \langle \exp[i\mathbf{Q}\cdot\mathbf{u}(k)]\rangle$, with $\langle\ldots\rangle$ indicating a time average. Assuming that the displacements are small (i.e., harmonic) and random, $2M$ is given by $\langle(\mathbf{Q}\cdot\mathbf{u})^2\rangle$, where the vector $\mathbf{u}$ is parallel to $\mathbf{Q}$.

[184] R. C. Shukla and C. A. Plint. Anharmonic contributions to the debye-waller factor: Calculation and application to aluminum. *Phys. Rev. B*, 40:10337–10344, Nov 1989.

[185] R. C. Shukla and D. W. Taylor. Debye-waller factor of sodium: A comparison of theory and experiment. *Phys. Rev. B*, 45:10765–10768, May 1992.

[186] J. S. Reid and J. D. Pirie. Dynamic deformation and the Debye–Waller factors for silicon-like crystals. *Acta Crystallographica Section A*, 36(6):957–965, Nov 1980.

[187] Claus Flensburg and Robert F. Stewart. Lattice dynamical debye-waller factor for silicon. *Phys. Rev. B*, 60:284–291, Jul 1999.

[188] G.-M. Rignanese, J.-P. Michenaud, and X. Gonze. Ab initio study of the volume dependence of dynamical and thermodynamical properties of silicon. *Phys. Rev. B*, 53:4488–4497, Feb 1996.

[189] Nguyen Van Hung, Cu Sy Thang, Nguyen Cong Toan, and Ho Khac Hieu. Temperature dependence of debye–waller factors of semiconductors. *Vacuum*, 101:63–66, 2014.

[190] Fernando D. Vila, J. J. Rehr, H. H. Rossner, and H. J. Krappe. Theoretical x-ray absorption debye-waller factors. *Phys. Rev. B*, 76:014301, Jul 2007.

[191] P. P. Lottici. Extended x-ray-absorption fine-structure debye-waller factors and vibrational density of states in amorphous arsenic. *Phys. Rev. B*, 35:1236–1241, Jan 1987.

[192] S. N. Taraskin and S. R. Elliott. Anharmonicity and localization of atomic vibrations in vitreous silica. *Phys. Rev. B*, 59:8572–8585, Apr 1999.

[193] C. S. Schnohr, P. Kluth, L. L. Araujo, D. J. Sprouster, A. P. Byrne, G. J. Foran, and M. C. Ridgway. Anisotropic vibrations in crystalline and amorphous inp. *Phys. Rev. B*, 79:195203, May 2009.

[194] Although it is not necessary to use DZ basis functions for constructing *a*-Si models, the MSD of atoms from lattice-dynamical calculations is found to be dependent on the basis functions used to obtain the dynamical matrix in Eq. (6.2). For numerical consistency, we therefore used double-zeta basis functions throughout this work (see Fig. 6.17).

[195] R.L.C. Vink, G.T. Barkema, W.F. van der Weg, and N. Mousseau. Fitting the stillinger–weber potential to amorphous silicon. *J. Non-Cryst. Solids*, 282:248, 2001.

[196] José M Soler, Emilio Artacho, Julian D Gale, Alberto García, Javier Junquera, Pablo Ordejón, and Daniel Sánchez-Portal. The SIESTA method for ab initio order-n materials simulation. *J. Phys.: Condens. Matter*, 14:2745, 2002.

[197] R. Fletcher. *Practical Methods of Optimization*. John Wiley and Sons, 1987.

[198] Parthapratim Biswas, Raymond Atta-Fynn, and Stephen R. Elliott. Metadynamical approach to the generation of amorphous structures: The case of *a*-si:h. *Phys. Rev. B*, 93:184202, May 2016.

[199] C. Kittel. *Introduction to Solid State Physics, 5th Edition*. John Wiley & Sons,, 1976.

[200] K. Takimoto, A. Fukuta, Y. Yamamoto, N. Yoshida, T. Itoh, and S. Nonomura. Linear thermal expansion coefficients of amorphous and microcrystalline silicon films. *Journal of Non-Crystalline Solids*, 299-302:314–317, 2002.

[201] The argument can be readily presented for a one-dimensional ordered chain of lattice constant a and spring constant k, where $\omega^2(q \to 0) = kq^2a^2/M$ in the nearest-neighbor interaction between atoms. A scale transformation $x' = sx$ leads to $k' = k/s^2$ in thermal equilibrium at temperature T and we have $u_i'^2 \approx \sum_n (k_B T)/M\omega_n'^2 e_i(n)^2 \approx u_i^2$.

[202] B. T. M. Willis and A. W. Pryor. *Thermal Vibrations in Crystallography*. Cambridge Univ. Press, 1975.

[203] B. L. Zink, R. Pietri, and F. Hellman. Thermal conductivity and specific heat of thin-film amorphous silicon. *Phys. Rev. Lett.*, 96:055902, Feb 2006.

[204] M. Mertig, G. Pompe, and E. Hegenbarth. Specific heat of amorphous silicon at low temperatures. *Solid State Communications*, 49(4):369–372, 1984.

[205] J. L. Feldman, J. Q. Broughton, and F. Wooten. Elastic properties of amorphous Si and derived debye temperatures and grüneisen parameters: Model calculation. *Phys. Rev. B*, 43:2152–2158, Jan 1991.

[206] R. C. Zeller and R. O. Pohl. Thermal conductivity and specific heat of noncrystalline solids. *Phys. Rev. B*, 4:2029–2041, Sep 1971.

[207] E. W. Hornung, R. A. Fisher, G. E. Brodale, and W. F. Giauque. Isotope sieve for 4he vs 3he. the low temperature heat capacity of sio2 glass before and after contact with 4he and 3he. *The Journal of Chemical Physics*, 50(11):4878–4886, 1969.

[208] W. Marshall. Specific heat of dilute alloys. *Phys. Rev.*, 118:1519–1523, Jun 1960.

[209] P. W. Anderson, B. I. Halperin, and C. M. Varma. Anomalous low-temperature thermal properties of glasses and spin glasses. *The Philosophical Magazine: A Journal of Theoretical Experimental and Applied Physics*, 25(1):1–9, 1972.

[210] Frank Finkemeier and Wolfgang von Niessen. Boson peak in amorphous silicon: A numerical study. *Phys. Rev. B*, 63:235204, May 2001.